Building Structural Complexity in Semiconductor Nanocrystals through Chemical Transformations

Bryce Frederick Sadtler

Department of Chemistry
University of California, Berkeley
Berkeley, CA 94720

and

Materials Science Division
Lawrence Berkeley National Laboratory
Berkeley, CA 94720

May, 2009

This work was supported by the Director, Office of Science, Office of Basic Energy Sciences, of the U.S. Department of Energy under Contract No. DE-AC02-05CH11231.

Building Structural Complexity in Semiconductor Nanocrystals through Chemical Transformations

by

Bryce Frederick Sadtler

B.S. in Chemistry (Purdue University) 2002
B.S. (Purdue University) 2002

A dissertation submitted in partial satisfaction of the
requirements for the degree of

Doctor of Philosophy

in

Chemistry

in the

GRADUATE DIVISION

of the

UNIVERSITY OF CALIFORNIA, BERKELEY

Committee in charge:

Professor A. Paul Alivisatos, Chair
Professor Peidong Yang
Professor Michael Crommie

Spring 2009

The dissertation of Bryce Frederick Sadtler is approved:

_____

Chair Date

_____

Date

_____

Date

University of California, Berkeley

Building Structural Complexity in Semiconductor Nanocrystals through Chemical Transformations

by

Bryce Frederick Sadtler

Abstract

Building Structural Complexity in Semiconductor Nanocrystals through Chemical Transformations

by

Bryce Frederick Sadtler

Doctor of Philosophy in Chemistry

University of California, Berkeley

Professor A. Paul Alivisatos, Chair

Methods are presented for synthesizing nanocrystal heterostructures comprised of two semiconductor materials epitaxially attached within individual nanostructures. The chemical transformation of cation exchange, where the cations within the lattice of an ionic nanocrystal are replaced with a different metal ion species, is used to alter the chemical composition at specific regions of a nanocrystal. Partial cation exchange was performed in cadmium sulfide (CdS) nanorods of well-defined size and shape to examine the spatial organization of materials within the resulting nanocrystal heterostructures.

The selectivity for cation exchange to take place at different facets of the nanocrystal plays an important role in determining the resulting morphology of the binary heterostructure. The exchange of copper (I) (Cu^{+}) cations in CdS nanorods occurs preferentially at the ends of the nanorods. Theoretical modeling of epitaxial attachments between different facets of CdS and Cu_2S indicate that the selectivity for cation

exchange at the ends of the nanorods is a result of the low formation energy of the interfaces produced.

During silver (I) (Ag^+) cation exchange in CdS nanorods, non-selective nucleation of silver sulfide (Ag_2S), followed by partial phase segregation leads to significant changes in the spatial arrangement of CdS and Ag_2S regions at the exchange reaction proceeds through the nanocrystal. A well-ordered striped pattern of alternating CdS and Ag_2S segments is found at intermediate fractions of exchange. The forces mediating this spontaneous process are a combination of Ostwald ripening to reduce the interfacial area along with a strain-induced repulsive interaction between Ag_2S segments.

To elucidate why Cu^+ and Ag^+ cation exchange with CdS nanorods produce different morphologies, models for epitaxial attachments between various facets of CdS with Cu_2S or Ag_2S lattices were used to calculate interface formation energies. The formation energies indicate the favorability for interface nucleation at different facets of the nanorod and the stability of the interfaces during growth of the secondary material (Cu_2S or Ag_2S) within the CdS nanocrystal. The physical properties of the CdS-Ag_2S and CdS-Cu_2S binary nanorods are discussed in terms of the electronic structure of their components and the heterostructure morphology.

Professor A. Paul Alivisatos
Dissertation Committee Chair

To Ben and Guilia

Table of Contents

List of Figures

List of Tables

Acknowledgments

Before I began graduate school at Berkeley, I told myself that I could be my own island among the sea of other scientists at a top research university. This turned out to be as far as possible from the truth. There are many people to thank for a great deal of help during my path through graduate school.

First of all, I have received a great deal of support from my research advisor, Paul Alivisatos. Thank you for upholding a strong set of academic ideals and for giving me freedom and encouragement to pursue my own research goals.

The members of the Alivisatos group when I arrived made my first years of graduate school a very positive experience. Alex Mastroianni and Josh Wittenberg took me aside during the open house on my first day in Berkeley to give me advice about joining the group. Always a step ahead, they have continued to do so all the way through the writing of my dissertation. I am very grateful to have overlapped with the senior graduate students of the laboratory, Ben Boussert, Deborah Aruguete, Delia Milliron, and Christine Micheel who provided a tremendous amount of support during the years we spent together. They helped me to pick a research project and provided a lot of useful insight into surviving graduate school. Delia taught me the secrets of nanocrystal synthesis, and continues to share expertise on the subject. I spent the majority of my first two years of graduate school working with Ben Boussert, who was both a great mentor and a close friend. I continually reminisce about the times that Ben, Giulia Adesso, and I shared together in D86 Hildebrand.

My graduate research involved a strong collaboration between many other talented scientists in the Alivisatos group, at the University of California, Berkeley and the Lawrence Berkeley National Laboratory. Richard Robinson and I worked together for several years to understand one very interesting observation. Rich also helped push me through the activation barrier of taking a research project from start to finish. Denis Demchenko and Lin-Wang Wang did the theoretical modeling of nanoscale interfaces

that are included in this dissertation. Haimei Zheng performed a substantial amount of electron microscopy, which was essential to this project. Steven Hughes also helped with the electron microscopy and the understanding of heterostructure growth in nanocrystals. Paul Peng and Professor Richard Saykally performed the transient absorption spectroscopy.

Thank you to Matt Sheldon for many enjoyable scientific discussions while walking between the lab and the gym. Thanks to Gordana Dukovic for being a good friend, scientific collaborator, and also proving that a commitment to scientific creativity and integrity was the essential combination for becoming a professor at a top research university. I greatly appreciate the many exchanges of advice and experience concerning research, career goals, and other essential topics with members of the Alivisatos group, including Jon Owen, Shelley Claridge, Steven Hughes, Rachel Smith, Emory Chan, Sassan Sheikholeslami, Yi Cui, and Young-wook Jun. Thank you to Heather Whitley for teaching me Latex and a lot about quantum mechanics during our time together as teaching assistants. Thank you to Rita Tidwell, James Wang, and Helen Cameron making sure there was a source of ample funding, chemicals, and supplies to conduct this research.

My undergraduate advisor, Professor Alex Wei, at Purdue University and members of his group, Stephen Pusztay, Jihane Achkar, Fabien Boulineau, Beomseok Kim, and Steven Tripp taught me how to conduct scientific research. My experience working with them is the primary reason that I decided to graduate school. I also thank Professors Jean-Pierre Sauvage and Jinwoo Cheon, who graciously hosted me in their laboratories during my visits abroad.

My last year of graduate school has been equally enjoyable as the first, primarily due to the arrival of several new members of the Alivisatos group who have re-sparked my excitement for research. Thanks especially to Jessy Baker, Charina Choi, Joey Luther, and Jen Dionne. I almost wish that I could be a grad student for another year so that we could continue to work together.

Thank you to Loo Lin for her encouragement, understanding, and patience.

Lastly, I thank my parents who rarely questioned what I was doing during most of my education, and trusted me to make the right choices.

Chapter 1.
Introduction

Nanocrystals are crystalline materials composed of ~ 100 to ~100,000 atoms and represent an intermediate size regime between molecules and macroscopic matter. While they possess a periodic atomic structure similar to that of extended crystalline lattices, they can exhibit vastly different chemical and physical properties as a result of their small size.[1] The physical origins of size dependence of both structural and electronic transitions in semiconductor nanocrystals are discussed below. Cadmium selenide (CdSe) nanocrystals are the most well studied colloidal semiconductor material and serve as a starting point for understanding how nanocrystal size, shape, and composition can be used to govern their physical properties. Such control has led to the design of nanocrystal architectures for a range of applications including medical diagnostics, catalysis, information processing, and energy storage and conversion.[2-8] Building further complexity through the spatial positioning of different components in higher order nanostructures will enhance their functionality in these applications.[9]

1.1 Structural Properties of Nanocrystals

The surfaces of semiconductor nanocrystals are normally composed of well-defined crystalline facets. The exact restructuring of these surfaces may be different from that of bulk crystals, as a result of the various organic or inorganic species that are

used both to control the growth of the nanocrystals and to passivate unsaturated surface atoms.[1,10-12] As discussed below in section 1.3, the specific facets exposed at the surface define the nanocrystal shape and can be varied with the conditions used to nucleate and grow the crystals. The relative stability of these facets governs the reactivity of the nanocrystal towards structural transformations.

Both the kinetics and thermodynamics of solid-state transformations in nanocrystals deviate significantly from those of macroscopic crystals due to their small size resulting in a high surface-to-volume ratio.[1] For nanometer-size crystals, surface atoms comprise a significant fraction of the total number of atoms within the lattice. The increase in surface-to-volume ratio with decreasing size alters the thermodynamic stability of various structural phases leading to a strong size-dependency of phase transitions. For example, the melting point of CdSe nanocrystals is depressed with decreasing size, due to the increasing number of unsaturated surface bonds.[13] On the other hand, the pressure-induced phase transition, CdSe nanocrystals from the 4-cooridinate wurtzite phase to the 6-coordinate rock-salt phase, exhibits the opposite trend. Here the transition at occurs at a higher pressure for smaller nanocrystals as a result of the increased energetic barrier for structural reorganization at the surface.[14,15]

The interface created during the nucleation of a new composition or structural phase within a crystal imposes an activation barrier to the transformation. As each nanocrystal is normally composed of a single domain, the kinetics of their conversion can be more closely akin to molecular reactions in solution rather than transformations in bulk multicrystalline materials.[16,17] In macroscopic crystals multiple nucleation events

occur throughout the solid, which are strongly affected by the presence of grain boundaries, vacancies and other defects throughout the extended lattice. The interior of a nanocrystal lattice tends to be nearly perfect as the presence of a defect significantly raises the total energy of the crystal.[18] Furthermore, defects can be easily expelled as only small diffusion lengths are required for them to reach the surface. Thus, phase transitions in nanocrystals can occur through a single nucleation event, where rapid transformation occurs once the activation barrier against nucleation of the new phase is overcome.[16] The activation barrier defines the transition state between the initial and final structures, analogous to a reaction pathway in a molecular transformation. A unique consequence of such single crystal to single crystal transformations is that they can be fully reversible over multiple cycles.

1.2 Optical Properties of Semiconductor Nanocrystals

While changes in the reactivity of nanocrystals are primarily a result of the large fraction of surface atoms comprising each crystal, the wide tunability in the optical and electronic properties of semiconductor nanocrystals arise from the quantum confinement of charge carriers (electrons and holes). As the electronic structure of nanocrystals fall between that of molecules and bulk crystals, both the languages of molecular orbital theory and solid-state physics are useful in describing the development in electronic structure with nanocrystal size. A brief introduction to the basic electronic structure of

semiconductors is first provided to put into context the utility of tuning the electronic structure in nanocrystals.

The bonding of atomic orbitals leads to the splitting of their energy levels into filled and unfilled states (i.e. two electrons occupy the lower energy level, while the higher level is unoccupied). When the number of atoms in a material approaches infinity (such as in an extended crystal), then the energy spacing between levels becomes much smaller than the thermal energy needed to excited an electron from one state to another, such that the levels form continuous bands. However, in semiconductors, there is an energy gap between the filled and unfilled electronic bands, which are called the valence and conduction bands, respectively. Given sufficient energy, electrons in the valence band can be promoted into the conduction band. The function of most semiconductor devices relies on the utilization of such optically or electrically excited charge carriers. For many semiconductors of interest in optoelectronic applications, the difference in between top edge of the valence band and the bottom edge of the conduction band, referred to as the band gap, falls within the energy regime of visible radiation. Thus, the absorption of light can promote electrons from the valence band into the conduction band. The absence of the electron in the valence band effectively creates a positively charged carrier, known as a hole. Coulomb attraction between the negatively-charged electron and positively-charged hole creates a bound electron-hole pair, called an exciton. Relaxation of the electron back to the valence band leads to recombination of the electron and hole. This process can either occur non-radiatively, through vibrational relaxation, or radiatively leading to the emission of a photon of the band gap energy.

In a nanometer-size crystal, the density of electronic levels becomes discrete due the fewer number of atomic orbitals contributing to the electronic bands (see Figure 1.1). In semiconductor nanocrystals, the density of states become most sparse near the band edges, concentrating the oscillator strength of optical excitations into a small number of electronic transitions. The band gap also widens in energy as the size of the nanocrystal decreases, as can be understood from the Heisenberg uncertainty principle. When electrons become confined to a smaller volume than their Bohr exciton radius, the uncertainty in their momentum will become greater. This raises the energy of all the electronic levels and widens the energy difference between filled and unfilled states. Thus, the band gap energy, which determines the onset of optical absorption and fluorescence emission can be systematically controlled for crystals with nanometer length-scales, based on their size. For instance, fluorescence emission in cadmium chalcogenide nanocrystals (CdS, CdSe, CdTe) can be tuned through the visible spectrum based the size and composition of the nanocrystal.[19,20] The physical parameters of bulk semiconductors such as the band gap, the effective masses of electrons and holes, Bohr exciton radius, exciton binding energy, and dielectric constant serve as a starting point for understanding how quantum-size effects emerge in nanocrystals made of different compositions. For example, lead sulfide (PbS) has a much larger Bohr exciton radius and a much smaller bulk band gap than CdS. Consequently there is a much larger variability in the band gap with size for PbS compared to CdS nanocrystals.[21]

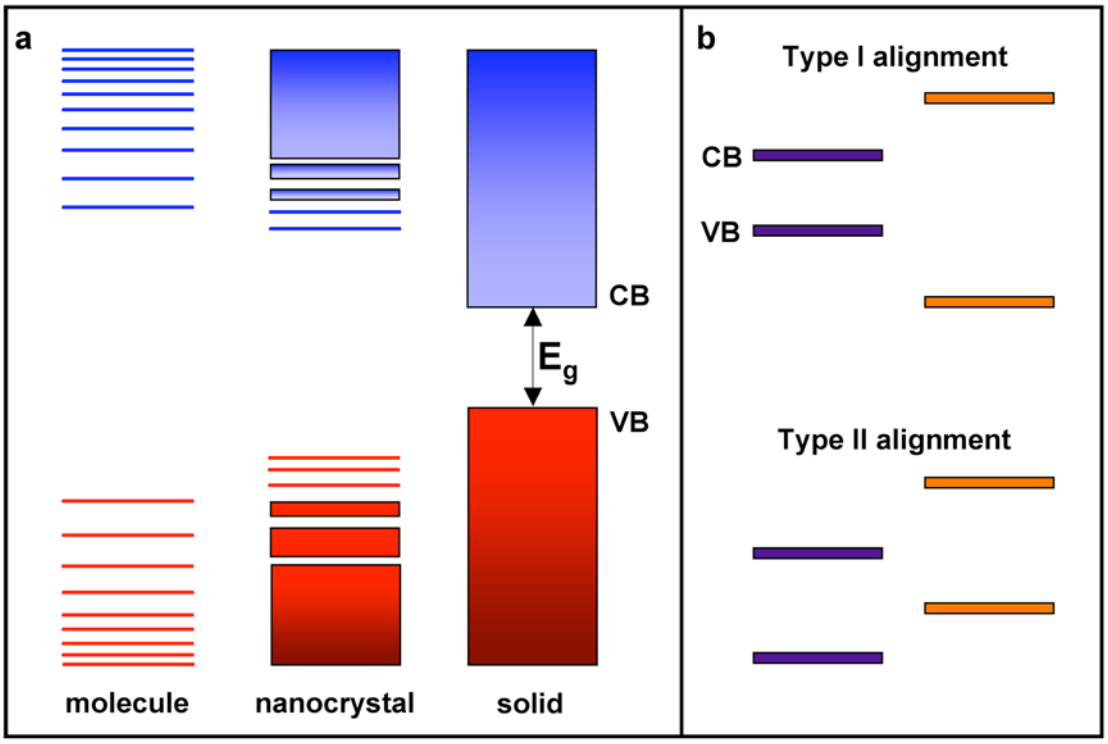

Figure 1.1. Electronic structure of semiconductor nanocrystals (a) Nanocrystals have an electronic structure that is intermediate between molecules and bulk solids. The levels become discrete near the band edges. E_g is band gap energy or the difference between the valence band (VB) and conduction band (CB) edges. (b) The alignment of band edges in a semiconductor heterostructure can be either sandwiched (Type I) or staggered (Type II).

Anisotropy in the nanocrystal shape will break the symmetry of the electronic levels along different directions of the crystal. For instance, in semiconductor nanorods the band gap emission depends primarily on the diameter, as it is the most confined dimension.[22] Furthermore, fluorescence emission from CdSe nanorods is linearly polarized as the lowest lying level in the conduction band is a superposition of electron orbitals parallel to the length of the nanorod.[23] Thus, shape control in low-dimensional materials can produce unique optical properties that are not found in extended crystals.

1.3 Synthesis and Shape Control of Colloidal Nanocrystals

The synthesis of colloidal inorganic nanocrystals using wet chemical techniques has been extensively studied for over the past 25 years to produce a variety of nanocrystalline materials of well-defined sizes, shapes and compositions.[1,19-47] Nanocrystals are normally synthesized via the thermal decomposition of organometallic precursors at high temperatures in the presence of coordinating species, which reversibly bind to the nanocrystals during their growth. Reaction parameters such as the growth time, temperature, and the choice of the inorganic precursors and stabilizing agents can be used to adjust the rate of monomer addition to different facets of the nanocrystals in order to control size and shape. Organic surfactant molecules, generally consisting of a polar head group and a hydrophobic chain (classes include alkylamines, alkylcarboxylic acids, alkylphosphonic acids, alkylthiols, trialkyphosphines, etc), both provide extensive influence over the nanocrystal growth kinetics and serve to stabilize the nanocrystals in aqueous or organic solutions. The temporal separation of nucleation and growth stages is often used to achieve monodisperse colloidal nanostructures.[39,48,49] If the nucleation of all the nanocrystals to be formed in the reaction occurs simultaneously, then their growth rates as the amount of available monomer is depleted will be similar. However, if new nucleation events occur during the growth of the initially formed nanocrystals, then there will be a wide size distribution. Additional injections to increase the monomer concentration can be used to focus the nanocrystal size distribution as smaller crystals will grow faster than larger ones.[48]

Nanocrystals with shapes including rods, disks, cubes, sheets, plates, and tetrapods can be produced through judicious choice of the growth conditions.[28-39] These shapes often reflect the symmetry of the underlying crystal lattice. For example, as PbS crystallizes in the cubic rock-salt phase, the nanocrystals form cubes or cuboctahedra.[21,31] CdS and CdSe, which possess a hexagonal wurtzite crystal structure, form elongated hexagonal nanorods.[28,29] For crystallization near thermodynamic equilibrium, facets that minimize the surface energy will dominate the crystal surface.[50] However, anisotropic nanocrystal growth is often achieved under highly non-equilibrium conditions, where more complicated shapes develop based on the relative rates of monomer addition to different facets of the crystal.[30,39,50] Surfactants that bind more strongly to particular facets will inhibit their growth by preventing monomer addition to these surfaces. In some cases, the particular habit of preferred facets or even the crystalline phase can change during crystal growth. For instance, CdSe and CdTe can nucleate as tetrahedral crystals in the zinc-blende phase. As the precursor concentration drops, the wurtzite phase become more stable, leading the formation of four wurtzite branches which extend from the tetrahedral core to produce tetrapod-shaped nanocrystals.[30,37] Systematic control of the crystal phase and branching can be used to grow a rich variety of nano-scale architectures.[50,51]

1.4 Methods for Making Nanocrystal Heterostructures

The synthesis of nanocrystal heterostructures is important both for creating multi-functional materials and for controlling electronic coupling between nanoscale units.[3,6,46,47] Similar to band-gap engineering in thin-film semiconductor growth, multilayer heterostructures can be grown to direct the energetic and spatial flow of excited charge carriers.[20,24-26] In one of the earliest examples, zinc sulfide (ZnS) was grown epitaxially as a shell around spherical CdSe nanocrystals.[20,24] These two semiconductors have a Type I band alignment, where the conduction band of ZnS is higher in energy and the valence band is lower in energy than that of CdSe (see schematic in Figure 1.1b). Passivation of surface states by the wider band gap material greatly increases the quantum yield of fluorescence emission from the CdSe nanocrystals. More recently, core-shell heterostructures have been synthesized with a Type II band alignment, where both the valence and conduction band edge of the core material are lower in energy than those of the shell (see schematic in Figure 1.1b).[25,26] Here, charge separation occurs as the electron relaxes into the lower lying conduction band of the core, while the hole is promoted to the higher energy valence band of the shell. Radiative recombination of these charges across the interface produces fluorescence that is lower in energy than the band gap of either material, enabling the emission to be tuned to the near-infrared wavelengths.

As the complexity of colloidal nanocrystal heterostructures increases beyond simple core-shell morphologies, their electronic structure and physical properties will strongly depend on the spatial organization of the two materials within each nanocrystal.

For example, dendritic nanocrystals with a Type II band alignment between the first and second generation of branching can lead to charge separation on a length scale of tens of nanometers.[40] Whereas, in tetrapod nanocrystals with a Type I band alignment between the arms and core, the wider band gap arms can be used to collect blue light and funnel carriers into the core leading to highly efficient fluorescence emission at red wavelengths.[41]

In organic chemistry, the ability to perform selective reactions on specific functional groups of a molecule is essential for obtaining complex molecular structures over multi-step syntheses. Such precision over the composition and spatial organization of nano-scale components would provide enormous flexibility for designing a new generation of nanostructures for advanced applications, such as the early detection of cancer, magnetic-data storage, and solar cell devices.[3,6-9] Colloidal nanocrystals possessing anisotropic shapes provide a platform for selective chemical modification based on the relative reactivities of the different crystalline facets exposed at the surface. This enables the synthesis of multi-component nanostructures through the nucleation and growth of a secondary material on specific facets of the preformed nanocrystals (see Figure 1.2a).[40-47]

While the methodology of sequential growth has been applied to a wide range of material combinations, its drawback is that the desired heterogeneous nucleation on the existing nanocrystal surface often competes with homogenous nucleation of separate nanocrystals of the secondary material. An alternative method for synthesizing nanocrystal heterostructures, which circumvents separate nucleation, is the

transformation of a portion of the nanocrystal into a new composition or structural phase. Chemical transformations greatly expand the library of compositions and morphologies that can be synthesized through solution-phase reactions on nanocrystals precursors. Examples of chemical transformations include galvanic displacement and alloying in metal nanocrystals, oxidation and sulfidation, and cation and anion exchange in ionic nanocrystals.[52-61]

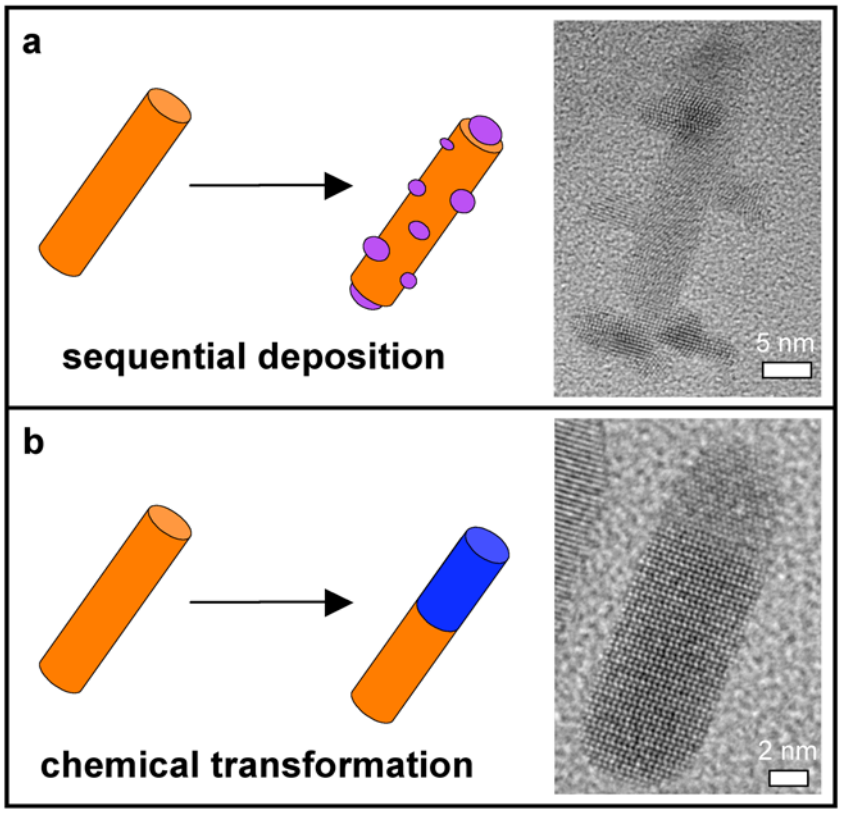

Figure 1.2. Methods for synthesizing nanocrystal heterostructures. (a) Sequential nucleation and growth on an existing nanocrystal. The heterostructure on the right is composed of zinc telluride (ZnTe) grown on cadmium sulfide (CdS) (b) Partial chemical transformation of an existing nanocrystal. The heterostructure on the right is composed of CdS and copper sulfide (Cu_2S).

Its high surface-to-volume ratio makes the entire nanocrystal accessible to solid-state reactions, which require the diffusion of atoms or ions through the crystal lattice. Thus, nanocrystals often displace enhanced reactivity to chemical transformations such as oxidation and cation exchange.[17,56,57,61] Similar to structural transformations, single crystal to single crystal chemical transformations can occur when there is a topotaxial relationship between the lattices of the initial and final compositons, such that the reaction interface grows epitaxially through the nanocrystal.[61-63] If the underlying connectivity of the crystal lattice is not maintained during the solid-state reaction, then the final morphology of the nanostructure will depend on the relative diffusion rates of the reacting species through the crystal lattice. For instance, in the sulfidation of metal cobalt (Co) and cadmium (CdS) anoparticles, the final structure (i.e. Co_3S_4 or CdS) is hollow due to the greater diffusion flux of material towards the outside of the particle.[56,57]

1.5 Cation Exchange in Ionic Nanocrystals

In ionic nanocrystals, cation exchange can be used to alter the composition of the material by replacing the cations within the nanocrystal lattice with a different metal ion.[59-66] For example, the addition of a small molar excess of Ag^+ cations to cadmium chalcogenide nanocrystals (CdS, CdSe, CdTe) leads to their complete conversion to the corresponding silver chalcogenide (i.e. Ag_2S, Ag_2Se, Ag_2Te). The thermodynamic driving force for the reaction will depend on the relative free energies of the initial and

final crystals and the solvation energies of the two cation species. The exchange reaction can be made thermodynamically favorable through the presence of coordinating molecules that preferentially solvate the cations within the nanocrystal lattice over the substitutional cations.[61,65] The cation exchange reaction is reversible; the structure and properties of the initial nanocrystals can be regained by altering the reaction conditions to favor the reverse reaction (e.g. Ag_2Se can be converted back to CdSe by using coordinating molecules that bind strongly to Ag^+ cations). When the mobilities of cations within the crystal lattices are high, complete cation exchange can occur rapidly (<1 second) and spontaneously at room temperature.[17,61-63] In these cases, partial transformation of the nanocrystal is achieved by limiting the ratio of substitutional cations in solution to those within the nanocrystals.

Remarkably, the shape of anisotropic nanocrystals such as rods and tetrapods is preserved after cation exchange when their dimensions are greater than the reaction zone for exchange (~ 4 nm), indicating that the connectivity of the anion sublattice is maintained during the diffusion and exchange of cations.[61-63] Thus, partial transformation of a nanocrystal creates a heterostructure where the two compounds share a common anion network and are epitaxially connected within a single nanostructure. Adjusting the ratio of substitutional cations to those within the nanocrystals can be used to control the relative volume fraction of the two crystals within the binary heterostructures. The spatial arrangement of materials within the nanocrystal will depend on a number of kinetic and thermodynamic factors such as the relative activation

barriers for cation exchange to initiate at different facets of the nanocrystal and the energetic stability of interfaces as reaction fronts proceed through the nanocrystal.

In this work, cadmium sulfide (CdS) nanorods with high shape and size monodispersity were used as a model system to study cation exchange reactions with different metal ions. Copper (I) (Cu^+) and silver (I) (Ag^+) cation exchange produce significantly different heterostructure morphologies of copper sulfide (Cu_2S) or silver sulfide (Ag_2S) within the host CdS nanorods. This dissertation examines the two cation exchange reactions in detail and identifies key parameters that mediate the morphological development during the solid-state transformation. Through control of the cation exchange process, novel nanocrystal architectures have been produced, which display tunable optical properties, making them promising materials for nanocrystal-based optoelectronic devices.

1.6 Dissertation Outline

Following the introduction in Chapter 1, a general description of the methods used for nanorod synthesis, cation exchange, structural and optical characterization of the nanocrystals, and the theoretical modeling of nano-scale interfaces is provided in Chapter 2. Each subsequent chapter details a set of experimental results and their analysis. The chapters are arranged for continuity of the concepts discussed and are not in chronological order of when the experiments or analysis were performed. Parts of this work have been previously published in peer-reviewed journals and have been

reproduced with permission from the publishers. At the beginning of each chapter, the publications that comprise portions of the chapter are listed. Each chapter has its own bibliography, although particular references may be appear in multiple chapters.

Chapter 3 examines the selectivity for Cu^+ cation exchange to occur at the ends of CdS nanorods. The epitaxial attachments of Cu_2S to the end facets of CdS nanorods have low formation energies, favoring their nucleation and growth during the exchange reaction. Additionally, as the two end facets of wurtzite CdS nanorods are crystallographically nonequivalent, asymmetric heterostructures can be produced by preferential nucleation at one end. The effect of different reaction conditions, including the size and shape of the initial CdS nanocrystals and the amount and rate of addition of Cu^+ cations on the resulting heterostructure morphology is examined. Such facet-selective reactions can provide orthogonality during multi-step chemical transformations.

Chapter 4 describes the spontaneous formation of 1D periodic patterns during Ag^+ cation exchange in CdS nanorods. This single-step chemical transformation provides a simple method to form striped nanorods composed of several alternating segments of CdS and Ag_2S. The phase segregation of Ag_2S and CdS materials via cation diffusion leads to significant changes in the morphology of the heterostructures as the fraction of Ag_2S increases within the nanorods. The forces mediating the spontaneous organization process are a combination of Ostwald ripening to reduce the interfacial area along with an elastic repulsive interaction between Ag_2S segments within the nanorod.

Chapter 5 compares the heterostructure morphologies produced by Cu^+ and Ag^+ cation exchange in CdS nanocrystals. Models for epitaxial attachments between various facets of CdS with Cu_2S or Ag_2S are used to calculate interface formation energies. The formation energies indicate the favorability for interface nucleation at different facets of the nanorod and the stability of the interfaces during growth of the secondary material (Cu_2S or Ag_2S) within the CdS nanocrystal. The relative stabilities of the epitaxial models correspond well with the frequency with which the corresponding morphologies are observed.

In Chapter 6 the optical properties of the CdS-Ag_2S and CdS-Cu_2S nanorod heterostructures produced by cation exchange are discussed. The absorption cross-section of the binary nanorods can be adjusted throughout the visible and near-infrared spectrum by varying the relative fraction of the high (CdS) and low (Ag_2S or Cu_2S) band-gap materials. The CdS-Ag_2S heterostructures exhibit near-infrared emission, which can be tuned with the size of the Ag_2S regions. Asymmetric CdS-Cu_2S nanorods may enable the separation of optically excited charge carriers at the interface followed by their transport to opposite ends of the elongated nanostructure.

1.7 Chapter 1 Bibliography

(1) Alivisatos, A. P. *Journal Of Physical Chemistry* **1996**, *100*, 13226-13239.

(2) Alivisatos, P. *Nature Biotechnology* **2004**, *22*, 47-52.

(3) Cheon, J.; Lee, J.-H. *Accounts of Chemical Research* **2008**, *41*, 1630-1640.

(4) Jun, Y.-W.; Seo, J.-W.; Cheon, J. *Accounts of Chemical Research* **2008**, *41*, 179-189.

(5) Narayanan, R.; Taber, C.; El-Sayed, M. A. *Topics in Catalysis* **2008**, *48*, 60-74.

(6) Jun, Y.-W.; Choi, J.-S.; Cheon, J. *Chemical Communications* **2007**, 1203-1214.

(7) Gratzel, M. *Nature* **2001**, *414*, 338-344.

(8) Milliron, D. J.; Gur, I.; Alivisatos, A. P. *MRS Bulletin* **2005**, *30*, 41-44.

(9) Murphy, C. *ACS Nano* **2009**, *3*, 770-774.

(10) Manna, L.; Wang, L. W.; Cingolani, R.; Alivisatos, A. P. *Journal of Physical Chemisty B* **2005**, *109*, 6183-6192.

(11) Puzder, A.; A. J. Williamson; Gygi, F.; Galli, G. *Physical Review Letters* **2004**, *92*, 217401-1-4.

(12) Puzder, A.; Williamson, A. J.; Zaitseva, N.; Galli, G.; Manna, L.; Alivisatos, A. P. *Nano Letters* **2004**, *4*, 2361-2365.

(13) Goldstein, A. N.; Echer, C. M.; Alivisatos, A. P. *Science* **1992**, *256*, 1425-1427.

(14) Tolbert, S. H.; Alivisatos, A. P. *Science* **1994**, *265*, 373-376.

(15) Tolbert, S. H.; Alivisatos, A. P. *The Journal of Chemical Physics* **1995**, *102*, 4642-4656.

(16) Jacobs, K.; Zaziski, D.; Scher, E. C.; Herhold, A. B.; Alivisatos, A. P. *Science* **2001**, *293*, 1803-1806.

(17) Chan, E. M.; Marcus, M. A.; Fakra, S.; ElNaggar, M.; Mathies, R. A.; Alivisatos, A. P. *Journal of Physical Chemisty A* **2007**, *111*, 12210-12215.

(18) Dalpian, G. M.; Chelikowsky, J. R. *Physical Review Letters* **2006**, *96*, 226802-1-4.

(19) Murray, C. B.; Norris, D. J.; Bawendi, M. G. *Journal of the American Chemical Society* **1993**, *115*, 8706-8715.

(20) Dabbousi, B. O.; Rodriguez-Viejo, J.; Mikulec, F. V.; Heine, J. R.; Mattoussi, H.; Ober, R.; Jensen, K. F.; Bawendi, M. G. *Journal of Physical Chemisty B* **1997**, *101*, 9463-9475.

(21) Hines, M. A.; Scholes, G. D. *Advanced Materials* **2003**, *15*, 1844-1849.

(22) Li, L.-S.; Hu, J.; Yang, W.; Alivisatos, A. P. *Nano Letters* **2001**, *1*, 349-351.

(23) Hu, J.; Li, L.-S.; Yang, W.; Manna, L.; Wang, L.-W.; Alivisatos, A. P. *Science* **2001**, *292*, 2060-2063.

(24) Hines, M. A.; Guyot-Sionnest, P. *Journal of Physical Chemisty* **1996**, *100*, 468-471.

(25) Kim, S.; Fisher, B.; Eisler, H.-J.; Bawendi, M. *Journal of the American Chemical Society* **2003**, *125*, 11466-11467.

(26) Smith, A. M.; Mohs, A. M.; Nie, S. *Nature Nanotechnology* **2009**, *4*, 56-63.

(27) Wang, X.; Zhuang, J.; Peng, Q.; Li, Y. *Nature* **2005**, *437*, 121-124.

(28) Peng, X.; Manna, L.; Yang, W.; Wickham, J.; Scher, E.; Andreas, K.; Alivisatos, A. P. *Nature* **2000**, *404*, 59-61.

(29) Jun, Y.-W.; Lee, S.-M.; Kang, N.-J.; Cheon, J. *Journal of the American Chemical Society* **2001**, *123*, 5150-5151.

(30) Manna, L.; Scher, E. C.; Alivisatos, A. P. *Journal of the American Chemical Society* **2000**, *122*, 12700-12706.

(31) Lee, S.-M.; Jun, Y.-W.; Cho, S.-N.; Cheon, J. *Journal of the American Chemical Society* **2002**, *124*, 11244-11245.

(32) Puntes, V. F.; Krishnan, K. M.; Alivisatos, A. P. *Science* **2001**, *291*, 2115-2117.

(33) Puntes, V. F.; Zanchet, D.; Erdonmez, C. K.; Alivisatos, A. P. *Journal of the American Chemical Society* **2002**, *124*, 12874-12880.

(34) Sigman, M. B. Jr.; Ghezelbash, A.; Hanrath, T.; Saunders, A. E.; Lee, F.; Korgel, B. A. *Journal of the American Chemical Society* **2003**, *125*, 16050-16057.

(35) Seo, J.-W.; Jun, Y.-W.; Park, S.-W.; Nah, H.; Moon, T.; Park, B.; Kim, J.-G.; Kim, Y. J.; Cheon, J. *Angewandte Chemie-International Edition* **2007**, *46*, 8828-8831.

(36) Seo, J.-W.; Jang, J.-T.; Park, S.-W.; Kim, C.; Park, B.; Cheon, J. *Advanced Materials* **2008**, *20*, 4269-4273.

(37) Manna, L.; Milliron, D. J.; Meisel, A.; Scher, E. C.; Alivisatos, A. P. *Nature Materials* **2003**, *2*, 382-385.

(38) Jun, Y.-W.; Choi, J.-S.; Cheon, J. *Angewandte Chemie-International Edition* **2006**, *45*, 3414-3439.

(39) Yin, Y.; Alivisatos, A. P. *Nature* **2005**, *437*, 664-670.

(40) Milliron, D. J.; Hughes, S. M.; Cui, Y.; Manna, L.; Li, J.; Wang, L.-W.; Alivisatos, A. P. *Nature* **2004**, *430*, 190-195.

(41) Talapin, D. V.; Nelson, J. H.; Shevchenko, E. V.; Aloni, S.; Sadtler, B.; Alivisatos, A. P. *Nano Letters* **2007**, *7*, 2951-2959.

(42) Shieh, F.; Saunders, A. E.; Korgel, B. A. *Journal of Physical Chemistry B* **2005**, *109*, 8538-8542.

(43) Shi, W.; Zeng, H.; Sahoo, Y.; Ohulchanskyy, T. Y.; Ding, Y.; Wang, Z. L.; Swihart, M.; Prasad, P. N. *Nano Letters* **2006**, *6*, 875-881.

(44) Mokari, T.; Rothenberg, E.; Popov, I.; Costi, R.; Banin, U. *Science* **2004**, *304*, 1787-1790.

(45) Kudera, S.; Carbone, L.; Casula, M. F.; Cingolani, R.; Falqui, A.; Snoeck, E.; Parak, W. J.; Manna, L. *Nano Letters* **2005**, *5*, 445-449.

(46) Cozzoli, P. D.; Pellegrino, T.; Manna, L. *Chemical Society Reviews* **2006**, *35*, 1195-1208.

(47) Casavola, M.; Buonsanti, R.; Caputo, G.; Cozzoli, P. D. *European Journal of Inorganic Chemistry* **2008**, 837-854.

(48) Peng, X.; Wickham, J.; Alivisatos, A. P. *Journal of the American Chemical Society* **1998**, *120*, 5343-5344.

(49) Peng, Z. A.; Peng, X. *Journal of the American Chemical Society* **2002**, *124*, 3343-3353.

(50) Choi, K.-S. *Dalton Transactions* **2008**, 5432-5438.

(51) Kanaras, A. G.; Sonnichsen, C.; Liu, H.; Alivisatos, A. P. *Nano Letters* **2005**, *5*, 2164-2167.

(52) Sun, Y.; Xia, Y. *Science* **2002**, *298*, 2176-2179.

(53) Yin, Y. D.; Erdonmez, C.; Aloni, S.; Alivisatos, A. P. *Journal of the American Chemical Society* **2006**, *128*, 12671-12673.

(54) Wang, D.-Y.; Chen, C.-H.; Yen, H.-C.; Lin, Y.-L.; Huang, P.-Y.; Hwang, B.-J.; Chen, C.-C. *Journal of the American Chemical Society* **2007**, *129*, 1538-1540.

(55) Cable, R. E.; Schaak, R. E. *Journal of the American Chemical Society* **2006**, *128*, 9588-9589.

(56) Yin, Y.; Rioux, R. M.; Erdonmez, C. K.; Hughes, S.; Somorjai, G. A.; Alivisatos, A. P. *Science* **2004**, *304*, 711-714.

(57) Cabot, A.; Smith, R. K.; Yin, Y.; Zheng, H.; Reinhard, B. M.; Liu, H.; Alivisatos, A. P. *ACS Nano* **2008**, *2*, 1452-1458.

(58) Leonard, B. M.; Anderson, M. E.; Oyler, K. D.; Phan, T.-H.; Schaak, R. E. *ACS Nano* **2009**, *3*, 940-948.

(59) Mews, A.; Eychmuller, A.; Giersig, M.; Schooss, D.; Weller, H. *Journal of Physical Chemisty* **1994**, *98*, 934-941.

(60) Dloczik, L.; Koenenkamp, R. *Journal of Solid State Electrochemistry* **2004**, *8*, 142-146.

(61) Son, D. H.; Hughes, S. M.; Yin, Y.; Alivisatos, A. P. *Science* **2004**, *306*, 1009-1012.

(62) Robinson, R. D.; Sadtler, B.; Demchenko, D. O.; Erdonmez, C. K.; Wang, L.-W.; Alivisatos, A. P. *Science* **2007**, *317*, 355-358.

(63) Sadtler, B.; Demchenko, D. O.; Zheng, H.; Hughes, S. M.; Merkle, M. G.; Dahmen, U.; Wang, L.-W.; Alivisatos, A. P. *Journal of the American Chemical Society* **2009**, *131*, 5285-5293.

(64) Camargo, P. H. C.; Lee, Y. H.; Jeong, U.; Zou, Z.; Xia, Y. *Langmuir* **2007**, *23*, 2985-2992.

(65) Wark, S. E.; Hsia, C.-H.; Son, D. H. *Journal of the American Chemical Society* **2008**, *130*, 9550-9555.

(66) Pietryga, J. M.; Werder, D. J.; Williams, D. J.; Casson, J. L.; Schaller, R. D.; Klimov, V. I.; Hollingsworth, J. A. *Journal of the American Chemical Society* **2008**, *130*, 4879-4885.

Chapter 2.
Experimental and Theoretical Methods

2.1 Synthesis of Cadmium Sulfide Nanorods

Colloidal cadmium sulfide (CdS) nanorods were synthesized under air-free conditions at high temperature using standard Schlenk-line techniques. The approximate amounts of each of the reagents in a typical reaction are listed in parentheses. First, cadmium oxide (CdO, ~ 210 mg) along with varying amounts of octadecylphosphonic acid (ODPA, 0.5 – 1 g), tetradecylphosphonic acid (TDPA, 0 – 0.5 g), propylphosphonic acid (PPA, 0 – 25 mg), and the coordinating solvents trioctylphosphine oxide (TOPO, 2.5 – 3 g) or hexadecylamine (HDA, ~ 3 g) were added to a 3-neck, round-bottom flask. The contents of each flask were evacuated at 120ºC for at least 20 minutes to remove water during the melting of the mixture to form a solution. The flasks were then heated to 320ºC under argon for 20 to 30 minutes to enable complexation of cadmium ions with the alkylphosphonic acid ligands. The reaction flasks were cooled back to 120ºC and again evacuated for approximately 1 hour to remove water produced by the cadmium complexation. After the second evacuation step, the flasks were again heated under argon to 320ºC, and trioctylphosphine (TOP, 2 g) was injected into each flask. Separately the sulfur precursor, trioctylphosphine sulfide (TOPS) or tributylphosphine sulfide (TBPS), was prepared by mixing either TOP or tributylphosphine (TBP) and sulfur together in a 1:1 molar ratio inside an argon-filled glove box followed by stirring of the mixture at room temperature until the sulfur was fully dissolved (typically ~ 24

hours for TOPS and ~ 1 hour for TBPS). The trialkyphosphine sulfide, TOPS (0.65 – 1.3 g) or TBPS (~ 0.75 g), was injected into the flask, inducing nucleation of the nanocrystals, which were subsequently grown ~315ºC for 45 minutes to 90 minutes. Secondary aliquots of TOPS or TBPS (1 to 1.5 g) mixed with TOP (1 – 2.5 g) can be subsequently added either by rapid injection or slow injection via a syringe pump (typically at a rate of 0.1 – 0.2 mL/min).

After arresting nanocrystal growth by cooling the reaction to ~ 100°C, a non-polar solvent (hexane or toluene, 5 – 10 mL) and a surfactant (nonanoic acid or octylamine, 1 – 3 mL) were added to the reaction flasks, and the solutions were transferred to air-free vials. Centrifugation was used to separate the nanocrystals from the remaining cadmium-phosphonate complex and the excess surfactants used in the reaction. The nanorods were then washed several times with a combination of a nonpolar solvent (hexane or toluene, 5 – 15 mL), a surfactant (octylamine or nonanoic acid, 1 – 5 mL), and a polar solvent (chloroform, acetone, isopropanol, or methanol, 3 – 8 mL). The additional surfactants help to break up the excess cadmium-phosphonate complex, which can form a gel when the reaction is cooled to room temperature. Following each centrifugation step, the supernatant was removed, and the precipitated nanocrystals were redispersed in fresh solvents. The final washing step was performed without the presence of additional surfactants. Excess octylamine was found to inhibit cation exchange of the CdS nanorods, as it binds to copper (I) (Cu^+) and silver (I) (Ag^+) cations in solution. After the washing steps, the nanorods were dispersed in toluene and stored in an argon-filled glovebox. This procedure produces some branched structures

(i.e., bipods, tripods, and tetrapods) along with the nanorods. However, the majority of branched structures are removed during the washing steps, as they do not flocculate as easily as the nanorods and thus tend to stay in the supernatant. While the nanorods my flocculate over time, they can easily be redispersed through mild agitation. The CdS nanorods are generally stable for several years when stored in a glovebox.

The average diameter of the nanorods was typically between 4 – 5 nm, while the lengths could be varied between 20 – 100 nm. Longer reactions times and additional injections of TOPS or TBS during the reaction can be used to increase the anisotropy of the nanorods (i.e. increase the average length but not diameter). However, nanorod samples with longer average lengths typically also possess a larger variation in the length distribution. Short-chain alkylphosphonic ligands (i.e. hexyl- or propylphosphonic acid) increase the anisotropy of nanorod growth, but also increase the fraction of branched nanostructures. The addition of alkylamines or small volumes of water can be used to increase the average diameter of the nanorods, but also lead to both an increase in the diameter distribution and the fraction of branched nanostructures.

2.2 Cation Exchange of Cadmium Sulfide Nanorods

M^+ (M = Cu or Ag) cation exchange was used to convert CdS nanorods into CdS-M_2S binary nanorods and M_2S nanorods. The Cu^+ exchange reactions were performed inside an argon-filled glovebox at room temperature. The Ag^+ cation exchange reactions were either done at -66°C in air or at room temperature in an argon-filled glovebox. The

extent of conversion in the nanocrystals depends on the M^+/Cd^{2+} ratio, where an excess of M^+ ions (i.e. $M^+/Cd^{2+} > 2$ as two M^+ ions replace one Cd^{2+} ion for charge balance) leads to full conversion of the nanorod to M_2S. The molar concentration of Cd^{2+} ions for the CdS nanorod solutions was determined by inductively coupled plasma atomic emission spectroscopy (ICP-AES) of acid-digested samples. Typical molar extinction coefficients for Cd^{2+} within the CdS nanorod solutions were ~ 3×10^6 mol/cm^2 at 300 nm measured by visible absorption spectroscopy. The amount of Cd^{2+} in the CdS nanorod solution in each reaction was between 1×10^{-6} to 1×10^{-5} moles.

The salt, tetrakis(acetonitrile)copper(I) hexafluorophosphate ($[MeCN]_4Cu(I)PF_6$), was used in the Cu^+ exchange reactions as the weak binding affinity of the anion makes the salt readily soluble in methanol (MeOH). The Cu^+ solution in MeOH is completely miscible with the colloidal solution of nanorods dispersed in toluene. In a typical reaction, 12 mg of $[MeCN]_4Cu(I)PF_6$ was dissolved in 2.5 mL of MeOH. This solution was used for full conversion or was further diluted 5 or 10-fold for partial conversion. For full conversion, the $[MeCN]_4Cu(I)PF_6$ solution (~ 0.6 – 1 mL) was added to a stirring solution of CdS nanorods in toluene (~ 2 mL). For partial conversion a concentrated solution of CdS nanorods in toluene (~ 50 – 500 μL) was added to a stirring $[MeCN]_4Cu(I)PF_6$ solution (~ 0.1 – 1 mL) diluted in toluene (~ 2 mL). The color of the nanocrystals changes rapidly (< 1 second) from yellow to golden brown after mixing of the Cu^+ and CdS solutions. To examine the effect of slow addition of Cu^+ ions, the $[MeCN]_4Cu(I)PF_6$ solution was loaded into a syringe pump and added at a rate of 0.15 mL/min via a capillary needle to a stirring solution of CdS nanorods in toluene. The

nanorods were washed by the addition of MeOH followed by centrifugation and removal of the supernatant to remove excess cations in solution. No additional surfactants were added to the CdS-Cu_2S or Cu_2S nanocrystals, which remained stable over several months when suspended in toluene. While flocculation may occur, the nanorods can be redispersed by agitation.

Silver nitrate ($AgNO_3$) was used for the Ag^+ cation exchange reactions with CdS nanorods. The amounts used for a typical reaction were 2.0 ml of toluene, 0.6 mL of a 1.2×10^{-3} M $AgNO_3$ solution in MeOH, 0.3 mL of MeOH, and 0.2 mL of CdS nanorods in toluene. The optical density of 0.2 mL of the CdS nanorod solution diluted with 2 mL of toluene was ~ 0.8 at 350 nm. The color of the nanocrystals rapidly changes from yellow to dark brown after mixing the Ag^+ and CdS solutions for the room temperature reactions. For the low temperature reactions, the color would change as the reaction vial warmed to room temperature. Excess cations in solution were removed from the CdS-Ag_2S and Ag_2S nanorods by the addition of MeOH, followed by precipitation through centrifugation and removal of the supernatant. Fully converted Ag_2S nanorods were generally not soluble in pure toluene, but could be made more soluble by the addition of a small amount of isopropanol or TBP. The CdS-Ag_2S nanorods were stable against permanent aggregation over a period of several weeks. To convert Ag_2S nanorods back to CdS, a solution of the Ag_2S nanorods in tetrahydrofuran (0.5 – 1 mL) was mixed with a large excess of cadmium nitrate ($Cd(NO_3)_2$, 100 – 300 mg) dissolved in acetonitrile (MeCN, 1 mL). A drop of TBP was then added and the reaction was heated to approximately 75°C for 15 minutes while stirring.

2.3 Characterization Methods

Transmission electron microscopy (TEM) provides direct observation of the size, shape, and morphology of the nanorods. TEM samples were prepared by placing a drop of the nanocrystal solution onto a carbon-coated copper grid in an ambient atmosphere. Bright-field TEM images were obtained using a Tecnai G2 S-Twin electron microscope operating at 200 kV. The magnification of the images was between 71000× and 195000×. The length and diameter distributions of the initial CdS nanorods and fully converted Cu_2S and Ag_2S nanorods were gathered from bright-field TEM images. At least 150 measurements were made for each sample. All statistical measurements were collected from the images using Image-pro Plus software.

Under bright-field TEM conditions, the Cu_2S and CdS regions of the binary nanorods normally have similar contrast. In some cases the CdS segment appeared darker by Bragg diffraction of the electron beam. CdS has a more symmetric lattice than Cu_2S, making it is more likely to be oriented at the necessary angle for Bragg diffraction to occur. The CdS-Cu_2S interface could also be observed by high-resolution TEM, although the structure changes slowly over time. First, the Cu_2S material undergoes a phase transition from the low-temperature to the high-temperature chalcocite phase.[1] This structural change is followed by diffusion of Cu across the CdS-Cu_2S interface and the formation of Cu metal around the edges of the nanocrystals.

Maps of the elemental distribution of Cd and Cu in the CdS-Cu_2S nanocrystals were obtained by energy-filtered TEM (EFTEM). The EFTEM experiments were

performed using a Philips CM200 microscope or a monochromated F20 UT Technai microscope. Both microscopes were equipped with a field emission gun, an electron energy loss spectrometer and a Gatan Image Filter (GIF) and were operated at 200 kV. The Cd M-edge (404 eV) and Cu L-edge (931 eV) were used to make the color composite images. The Cu M-edge (120 eV, minor) was used for the Cu-EFTEM images.

Statistics for the segment lengths of the CdS and Cu_2S regions in the binary nanorods were determined from EFTEM images by making at least 150 measurements. The degree of asymmetry for each CdS-Cu_2S binary nanorod was taken to be one minus the ratio of the length of the short Cu_2S segment over the length of the long Cu_2S segment. Using this definition, a nanorod possessing two Cu_2S segments of equal lengths has an asymmetry value of 0, and a nanorod with Cu_2S on only one side of the nanorod has an asymmetry value of 1. The length fraction of the nanorod converted to Cu_2S was measured as the ratio of the combined length of Cu_2S segments over the total length of the nanorod. Thus, a nanorod that is entirely composed of CdS will have a length conversion of 0, and a nanorod fully converted to Cu_2S will have a value of 1. CdS-Cu_2S interfaces were grouped into three categories: flat and parallel to the nanorod cross-section, flat and at an angle to the cross-section, and multifaceted (which appear curved in low-magnification TEM images). As TEM imaging provides a two-dimensional projection of the nanorod heterostructures, the apparent angle and curvature of an interface depends on its relative orientation on the TEM substrate. Therefore, the

fraction of each of these types of interfaces, measured from a population of over 200 nanorods, is approximate.

The elemental distributions of the CdS-Ag_2S nanorods were observable from the atomic contrast difference in bright-field TEM, where the Ag_2S regions appear darker, do the higher density of metal atoms per unit volume. Energy-dispersive X-ray spectroscopy (EDS) was used to confirm the elemental distribution of Cd, Ag, and S within the nanorods. EDS spectra were collected with a Philips CM200/FEG scanning TEM equipped with an ultra-thin silicon window detector operated at 200 kV. Spherical aberration (Cs) and chromatic aberration (Cc) were both 1.2 mm. The energy resolution of the detector was 136 eV at 5.895 keV for Mn-Kα radiation. Electron-beam damage occurred more quickly in the Ag_2S containing nanorods, preventing HRTEM characterization.

For the CdS-Ag_2S nanorod heterostructures, the number of Ag_2S regions per nanorod, the Ag_2S segment lengths, and their center-to-center spacing were gathered from bright-field TEM images. Some CdS-Ag_2S superlattices contained small Ag_2S islands on the surface of the nanorod whose diameter was less than 25% of the CdS rod diameter; these islands were disregarded in the spacing measurements. Gaussian functions were used to fit the histograms. To estimate the volume fraction of Ag_2S within the superlattices, the total length fraction of Ag_2S segments along each nanorod was measured for 40 nanorod superlattices. Assuming the diameters of all the segments are equal, the volume fraction is proportional to the length fraction.

For the pair distribution histograms, coordinate markers were placed on the Ag_2S regions of the CdS-Ag_2S nanorod heterostructures. For partially formed Ag_2S segments, that do not span the nanorod diameter (which are the majority for low Ag^+/Cd^{2+} ratios and are found as a small fraction at intermediate Ag^+/Cd^{2+} ratios), the marker was placed at the center of the nanorod rather than the center of the Ag_2S region so that only the length component parallel to the nanorod axis between Ag_2S regions is measured. The coordinates were then used to compute the distance between each Ag_2S region within a given CdS nanorod with all other Ag_2S regions on that nanorod. These pair-wise Ag_2S distances were measured for over 200 nanorods in each sample. The spacings were normalized by multiplying by (n-1)/L, where n = the number of Ag_2S regions and L = sum of nearest neighbor spacings for the nanorod. As Ag_2S regions almost always occurred at each end of the nanorod, L is approximately the nanorod length.

The crystal structures of the CdS, CdS-Cu_2S, and Cu_2S nanorod samples were determined from powder X-ray diffraction (XRD) obtained on a Bruker AXS diffractometer using Co Kα radiation (1.790 Å) and a general area detector operating at 40 kV and 35 mA. The instrument resolution was 0.05° in 2θ, and the acquisition time for each sample was one hour. For the CdS, CdS-Ag_2S, and Ag_2S nanorod samples, XRD patterns were measured on a PANalytical X'Pert PRO MPD with an X'Celerator detector and a copper (Cu-Ka) radiation source (1.542 Å) operating at 40 kV and 40 mA. The accumulation time for each sample was at least 4 hours with a step size of 0.0334 degrees. The XRD samples were prepared by dissolving the precipitated nanocrystals in

a minimal amount of toluene or chloroform and either depositing the concentrated solution on a silicon plate or centrifuging it down into a 0.3 mm Borosilicate capillary.

For optical absorption and fluorescence measurements the nanocrystals were precipitated and redispersed in tetrachloroethylene and a 1 cm path-length FUV quartz cuvette was used with a flat absorption profile from ~ 170 – 2200 nm. Absorption spectra were recorded on an Agilent 8453 spectrometer, and were corrected for the solvent background. Fluorescence spectra were recorded on a Fluorolog 3 equipped with a Triax 320 spectrometer. For spectra in the visible range (425 – 750 nm), the excitation wavelength was 400 nm, and a photomultiplier tube (PMT) was used for detection. For visible to near-infrared (NIR) region (500 – 1100 nm), a charge-coupled device (CCD) detector was used. The excitation wavelength was 400 nm and a long-pass filter with a cut-off of ~ 500 nm was placed in front of the detector to block scattering of the excitation light. A liquid nitrogen cooled, InGaAs photodiode detector was also used for the NIR region (900 – 1400 nm). The excitation wavelength was varied between 400-600 nm, and a long-pass filter with a cutoff of 650 nm was placed in front of the detector. The emission spectra recorded using the PMT and InGaAs detector were corrected for the wavelength-dependent response of the emission grating and detector. The spectra recorded on the CCD were not corrected. Photoluminescence excitation (PLE) spectra at NIR emission wavelengths were also measured using the InGaAs detector. The emission was recorded at a fixed wavelength, while the excitation was varied between 400 to 600 nm in 5 nm increments. The emission slit was 10 nm. The PLE spectra were corrected for the wavelength dependence of the excitation intensity.

Femtosecond transient absorption spectra were measured using a 1 kilohertz (kHz) regeneratively-amplified titanium:sapphire laser system seeded by a home-built oscillator provided 1.2 millijoules (mJ) pulses at 800 nm for the time-resolved experiments. The majority of this output (90%) pumped a home-built noncollinear optical parametric amplifier (NOPA), which can be tuned to visible wavelengths (450 – 750 nm). The remainder of the 800 nm light was frequency doubled to 400 nm in a β-barium borate (BBO) crystal and either the fundamental or second-harmonic served as the optical pump in the experiments. A normalized transient bleach spectrum obtained with a white light continuum probe determined the lowest excitonic transition to be at a visible probe wavelength of 470 nm. Optical chopping the pump beam's path at 500 Hz allowed gated boxcar integrator detection of the differential probe transmission, $\Delta T/T$. A neutral density filter controlled the pump fluence to prevent no more than an average of one electron-hole pair excited per nanorod. The nanocrystals were dissolved in toluene and a 1 mm path-length NIR cuvette was used with a flat profile from ~ 250 – 3500 nm. The optical densities for the nanocrystal samples ranged from 0.5 – 1.5 at 400 nm. Pump and probe polarizations were at the magic angle, and all experiments were conducted at room temperature. Pulse durations of the pump and probe are ca. 200 and 400 femtoseconds (fs), as determined by autocorrelation measurements. Between 3 – 5 averaged transients represent each of the dynamics traces plotted, and the decay times were fit in Origin and re-plotted in Matlab.

2.4 Theoretical Modeling

Ab initio calculations were performed using Vienna Ab-initio Simulation Package (VASP) and Parallel total Energy (PEtot) programs, utilizing the local density approximation (LDA) and the generalized gradient approximation (GGA) to density functional theory (DFT).[2,3] Norm-conserving pseudopotentials were used in order to model the electron-ion interaction in PEtot. Projector augmented wave (PAW) pseudopotentials with planewave energy cutoffs of 280 eV were used in VASP. We used Γ-point only eigenenergies in the Brillouin zone as the supercells are sufficiently large to ensure weak dispersion of energy bands.

These techniques were used to estimate the stability of various phases of Cu_2S and Ag_2S and find optimal geometries for the epitaxial attachment between CdS with Cu_2S or Ag_2S. Interface formation energies for the CdS-Cu_2S and CdS-Ag_2S epitaxial attachments were calculated using the VASP program. All geometries were relaxed to have the forces on atoms reduced to 0.01 eV/Å or less. The interface formation energy is defined as the ab initio total energy difference of the supercell containing the interface and its bulk constituents. Total formation energies containing both chemical and elastic contributions were obtained by using the difference in energy between the supercell and natural bulk structures. To calculate the chemical energy alone, the bulk lattices were strained similar to the lattice in the supercell. The elastic contributions were computed assuming the distortions occurred in the Cu_2S or Ag_2S cell only to match to the lattice of the CdS cell. The cell thicknesses for Cu_2S were 13.5 Å for the end-on and angled

attachments to CdS and 27.3 Å for the side attachment. The cell thicknesses for Ag_2S were ~ 15.8 Å in all cases.

The supercell geometry used to calculate the interface formation energies implies infinite repetition of alternating CdS and Cu_2S (or Ag_2S) slabs, such that two interfaces are always present. If the case of the attachment of Cu_2S to the (0001) and $(000\bar{1})$ facets of CdS, the formation energies for the individual interfaces were calculated. CdS-Cu_2S supercells were constructed, which include a single CdS-Cu_2S interface and the opposite CdS and Cu_2S surfaces separated by vacuum. Thus, one supercell contains the attachment of the (001) facet of Cu_2S to the $(000\bar{1})$ facet of CdS, along with a Cd-terminated (0001) CdS surface passivated with pseudo-hydrogen atoms,[4] and an unpassivated $(00\bar{1})$ Cu_2S surface. The second supercell contains the attachment of the (001) facet of Cu_2S to the (0001) facet of CdS, along with a S-terminated $(000\bar{1})$ CdS surface passivated with pseudo-hydrogen atoms, and the same unpassivated $(00\bar{1})$ Cu_2S surface as in the first supercell. To determine the individual energies for the interfaces contained in these supercells, it is necessary to take into account the CdS and Cu_2S surface energies in each supercell as well as the difference in the number of Cu and Cd atoms between the two supercells. The non-equivalent CdS surface energies are subtracted out from each of the two supercells using auxiliary CdS constructions.[5] The difference in the number of atoms in the two supercells is accounted for by incorporating the chemical potentials of individual Cu and Cd atoms into the bulk chemical potential of the lattices. In order to cancel out the Cu_2S surface energies, both the supercells connect the (001) facet of Cu_2S to CdS such that the same $(00\bar{1})$ Cu_2S surface is exposed

for both supercells. In the original supercell containing both interfaces, the (001) Cu_2S facet connects to the $(000\bar{1})$ facet of CdS, while the $(00\bar{1})$ Cu_2S facet connect to the (0001) CdS facet. However, due to the similar bonding arrangement of interfacial Cu atoms for either Cu_2S facet, (001) or $(00\bar{1})$, connected to the (0001) CdS facet, their formation energies should be similar. Subtracting the Cu_2S surface energies leaves only the difference between the two CdS-Cu_2S interfaces. Combining the energy difference between the two interfaces with their sum determined from the original supercell leads to the desired individual formation energies for Cu_2S attached to the wurtzite CdS (0001) or $(000\bar{1})$ facets.

The electronic structures of the CdS-Ag_2S (Cu_2S) interfaces were estimated by comparing the site-projected densities of states (DOS) of the most bulk-like S atoms in the supercell with the site-projected DOS of bulk CdS and Ag_2S (Cu_2S). The valence band alignment at the CdS-Ag_2S interfaces was obtained by computing the macroscopic average of the electrostatic potential obtained within LDA/GGA. The alignment of the average electrostatic potential combined with the bulk values for the valence band maxima, computed relative to the bulk electrostatic potential, yields the band alignment. The conduction band alignment was obtained by adding the bulk experimental band gap value to the valence band energy, as the LDA GGA approximations tend to underestimate the value of the band gap energy.

The elastic energies and strain for the CdS-Ag_2S attachments were calculated using the Valence Force Field (VFF) method, which is an atomistic model for bond stretching and bending. The VFF model parameters for CdS are available in the

literature. Ab initio elastic constants for bulk Ag_2S were computed by distorting the crystal in the corresponding directions and fitting the total energy into second order elastic expansions. These elastic constants were then fit to the VFF model. A CdS nanorod was constructed to have two inclusion segments with the lattice mismatch and elastic constants of the Ag_2S structure determined from the ab initio calculations. All of the atomic positions were relaxed according to the VFF model, and the elastic energy after relaxation was calculated. This was done for several segment-segment separation distances for nanorod diameters of 4.8 and 6 nm. The surfaces of the nanorods were passivated with pseudo-hydrogen atoms.[4] The nanorod lengths varied with the segment separation from 30 to 42 nm, while the distance between the Ag_2S segments and the ends of the nanorods was kept constant in order to fix any possible contribution from the ends of the nanorods to the elastic energy. The number of atoms in the models varied from 25228 to 57201.

2.5 Chapter 2 Bibliography

(1) Putnis, A. *American Mineralogist* **1977**, *62*, 107-114.

(2) Kresse, G.; Furthmuller, J. *Computational Materials Science* **1996**, *6*, 15-50.

(3) Kresse, G.; Furthmuller, J. *Physical Review B* **1996**, *54*, 11169-11186.

(4) Wang, L.-W.; Li, J. *Physical Review B* **2004**, *69*, 153302-1-4.

(5) Zhang, S. B.; Wei, S.-H. *Physical Review Letters* **2004**, *92*, 086102-1-4.

Chapter 3.

Selective Facet Reactivity during Cation Exchange of Cadmium Sulfide Nanorods

3.1 Partial Cation Exchange Reactions in Ionic Nanocrystals

The partial transformation of ionic nanocrystals through cation exchange can be used to synthesize nanocrystal heterostructures. We demonstrate that the selectivity for cation exchange to take place at different facets of the nanocrystal plays a critical role in determining the resulting morphology of the binary heterostructure. In the case of Cu^+ cation exchange in CdS nanorods, the reaction front nucleates preferentially at the ends of the nanorods such that Cu_2S grows inward from either end. From interface formation energies calculated for epitaxial connections between different facets of CdS and Cu_2S, we infer the relative stability of each interface during the nucleation and growth of Cu_2S within the CdS nanorods. The epitaxial attachments of Cu_2S to the end facets of CdS nanorods minimize the formation energy, making these interfaces stable throughout the exchange reaction. Additionally, as the two end facets of wurtzite CdS nanorods are crystallographically nonequivalent, asymmetric heterostructures can be produced.

Cation exchange provides a facile method to systematically vary the proportion of two chemical compositions within individual nanostructures. In anisotropic

nanocrystals, various heterostructure morphologies can be envisioned depending on how the solid-state reaction proceeds through the crystal lattice. For example, if exchange occurs uniformly at all surfaces of the nanocrystal, then a core-shell morphology would develop. On the other hand, an asymmetric structure can result if the reaction is more facile at a particular facet. While the rapid kinetics of cation exchange in nanocrystals make *in situ* structural characterization challenging,[1] heterostructures produced at different degrees of conversion can provide insight into the temporal evolution of the morphology at a fixed concentration. As the size and shape can vary among a population of nanocrystals, it is essential to characterize the distribution of heterostructure morphologies obtained for a given exchange reaction.

3.2 Structural Characterization of CdS-Cu_2S and Cu_2S Nanorods

Cu^+ cation exchange was used to convert CdS nanorods into CdS-Cu_2S binary nanorods and Cu_2S nanorods. XRD patterns of the CdS nanorods before and after the addition of increasing amounts of Cu^+ cations are shown in Figure 3.1. The addition of excess Cu^+ cations relative to the amount of Cd^{2+} within the wurtzite CdS nanocrystals leads to their complete transformation to the low-temperature form of chalcocite Cu_2S as measured from XRD patterns of the reactant and product nanorods.[2] Partially converted samples made by substoichiometric addition of Cu^+ cations show a combination of diffraction peaks from both CdS and Cu_2S. Peaks belonging to the CdS phase disappear and peaks belonging to Cu_2S grow stronger in intensity with increasing amounts of Cu^+

added to the solution of CdS nanorods. While the diffraction peaks apparent in the partially converted nanorods could potentially arise from Cu_2S as chalcocite in its low or high temperature forms or from the non-stoichiometric djurleite phase ($Cu_{1.96}S$), we assume that the Cu_2S material is in the low temperature chalcocite phase during all stages of the exchange reaction. The epitaxial mismatch between CdS and Cu_2S is relatively low and the interfacial area does not change significantly as the CdS-Cu_2S interface move along the nanorod. Therefore, it is unlikely that a strain-induced phase change of the Cu_2S material occurs.

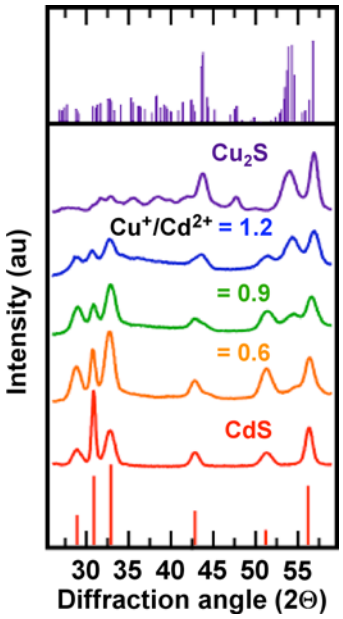

Figure 3.1. XRD patterns of initial CdS nanorods (bottom, red) and CdS-Cu_2S binary nanorods formed with increasing amounts of Cu^+. The addition of excess Cu^+ cations leads to full conversion of the wurtzite nanorods into the low temperature phase of chalcocite Cu_2S (top, purple). The Cu^+/Cd^{2+} cation ratio used for the partial exchange reactions is provided above each plot. Patterns from the Joint Committee on Powder Diffraction Standards (JCPDS) for wurtzite CdS (bottom, JCPDS #00-041-1049, space group P63mc (186)) and low temperature chalcocite Cu_2S (top, JCPDS # 00-033-0490, space group P21/c (14)) are included for reference.

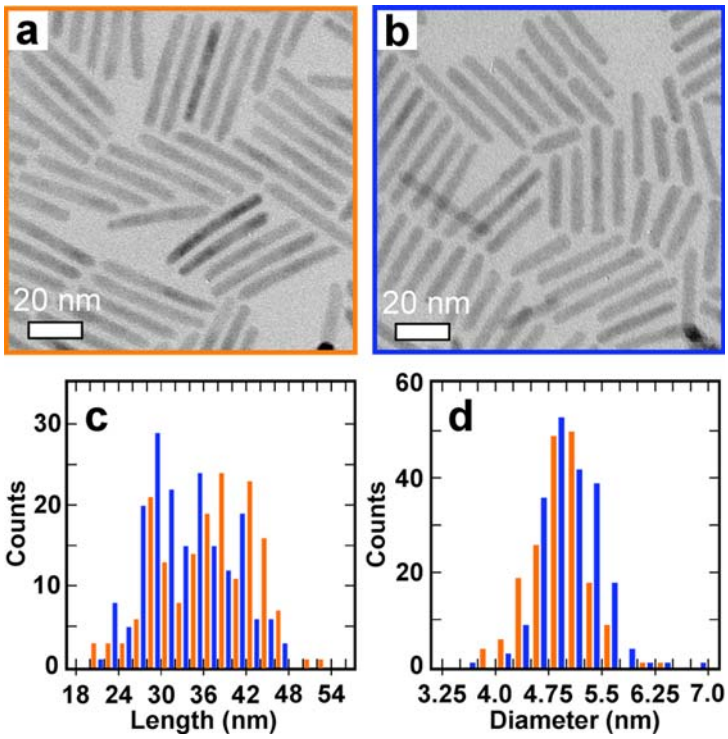

Figure 3.2. TEM images and size distributions of the nanorods before and after cation exchange. (a) TEM image of initial CdS nanorods. (b) Cu_2S nanorods after complete Cu^+ exchange, showing shape preservation of the nanorods. (c) Length distributions of the nanorods before (orange) and after (blue) cation exchange. (d) Diameter distributions of the nanorods.

The bright-field TEM images in Figure 3.2 show that after complete Cu^+ cation exchange, the shape and size of the nanorods is preserved within the 8% contraction in lattice volume upon conversion from CdS to Cu_2S. For partial Cu^+ exchange, energy-filtered TEM (EFTEM) was used to obtain elemental mappings of the Cu- and Cd-containing regions of binary nanorods. The composite energy-filtered image in Figure 3.3b clearly shows the CdS and Cu_2S portions of the binary nanorods, where the ends of the nanorods have been converted to Cu_2S. The preferential conversion of the ends occurs for nanorods of varying lengths, diameters, and aspect ratios. By observing

nanorods with different conversion fractions to Cu_2S, the EFTEM images indicate that cation exchange starts at the ends, and the Cu_2S regions grow into the nanorods upon further exchange. The only cases where Cu_2S segments existed in between regions of CdS were at sites of irregularities such as kinks along the nanorod diameter or at the zinc-blende branch-point of bipod and tripod nanocrystals.[3]

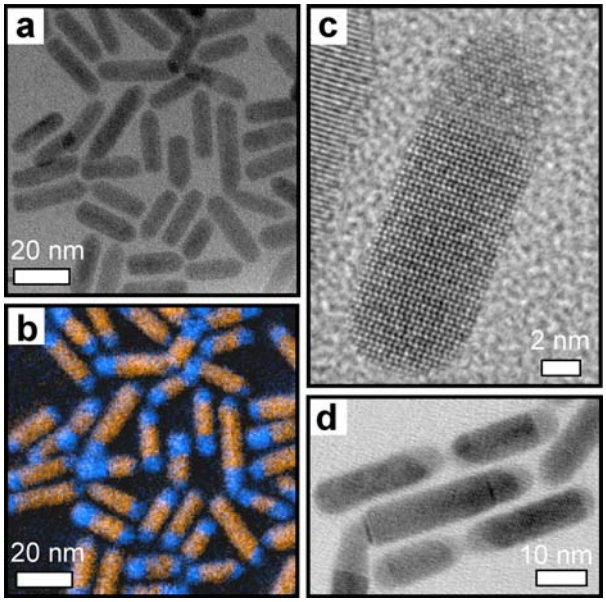

Figure 3.3. TEM images of CdS-Cu_2S binary nanorods. (a) Bright-field (zero-loss) image. (b) Color-composite EFTEM image, where the orange regions correspond to the Cd energy-filtered mapping and blue regions correspond to the Cu mapping. (c) High-resolution TEM image of a CdS-Cu_2S nanorod. (d) Bright-field TEM image, where CdS-Cu_2S interfaces can be seen at various angles relative to the nanorod cross-section.

The high-resolution TEM (HRTEM) image of a Cu_2S-CdS heterostructure in Figure 3.3c shows the epitaxial interface between the two materials within the nanorod. We observe electron beam induced changes to the Cu_2S crystal phase similar to previous

reports in Cu_2S thin films,[4] which prevent analysis of the CdS-Cu_2S interfacial atomic structure by HRTEM. However, the general shape, orientation and location of the interfaces within the nanorod can be observed by EFTEM. The majority of interfaces are flat and parallel to the cross-section of the nanorod (i.e. parallel to the (0001) plane of CdS). However, a significant population of interfaces (up to 30% in various samples) are at an angle of up to ~ 40° relative to the nanorod cross-section (see Figure 3.3d). As the apparent angle of the interface depends on the relative orientation of the nanorod on the TEM substrate, it is likely that these interfaces occur along specific crystallographic facets of the two lattices, rather than at a continuous range of angles. Some interfaces observed by HRTEM consist of multiple facets, which are flat in the middle and taper towards the outer edges of the interface, making them appear curved at lower-magnifications. Step-edges were also observed in some interfaces, which naturally arise if only a fraction of cations within an atomic layer is exchanged.

While Cu^+ cation exchange occurs at both ends of the CdS nanorods, the relative lengths of the two Cu_2S end segments within a given nanorod can vary significantly. As the CdS wurtzite lattice lacks inversion symmetry about the c-axis, the (0001) and $(000\bar{1})$ end facets of the nanorods are crystallographically nonequivalent.[3] Cd atoms at a $(000\bar{1})$ surface facet expose three dangling bonds whereas Cd atoms at a (0001) surface expose only one dangling bond. Thus, the bonding arrangement of Cd atoms to the interfacial sulfur layer at the CdS-Cu_2S attachment will be different at opposite ends of the nanorod. Two important factors found to affect the asymmetry of the Cu_2S end

segments are the shape (curvature and diameter) of the ends of the CdS nanorods and the rate of addition of the Cu^+ ions to the CdS solutions.

Figure 3.4 shows Cu-EFTEM images for three CdS-Cu_2S binary nanorod samples along with histograms of the asymmetry of the length of the Cu_2S segments within individual nanorods for each of the samples shown. To examine the effect of the nanocrystal dimensions on the asymmetry of Cu_2S segments, partial Cu^+ exchange was performed on nanorods of different lengths and diameters. Sample 1 shown in Figure 3.4a used CdS nanorods with an average length of 48±7 nm (average ± first standard deviation) and a diameter of 6±0.8 nm. The molar ratio of Cu^+ cations relative to Cd^{2+} was 0.51. In this case, the Cu_2S segment lengths are symmetric, evident by the continual decrease in counts in the asymmetry histogram in Figure 3.4d from 0 to 1. The mean asymmetry for this sample was 0.25, where the asymmetry of the two Cu_2S segments in a given binary nanorod is defined as one minus the ratio of the length of the short segment length over the length of the long segment. In sample 2 shown in Figure 3.4b, a Cu^+/Cd^{2+} ratio of 0.56 was used to make CdS-Cu_2S heterostructures from CdS nanorods with a smaller average length but larger diameter (length = 29±4 nm and diameter = 9±0.8 nm). The reaction produced asymmetric heterostructures, as the counts in the asymmetry histogram tend to increase from 0 to 1 (mean asymmetry = 0.6). As seen in the EFTEM images in Figure 3.4, a significant difference between the two nanorod samples is that the ends of smaller diameter nanorods used to make sample 1 possess higher curvature, indicating they are composed of multiple surface facets. This appears to lead to a higher fraction of curved (multifaceted) interfaces in sample 1 (~18%)

compared to sample 2 (~2 %). On the other hand, there appears to be no correlation between the asymmetry of the Cu_2S segments and the length of the nanorods (see Figure 3.5a).

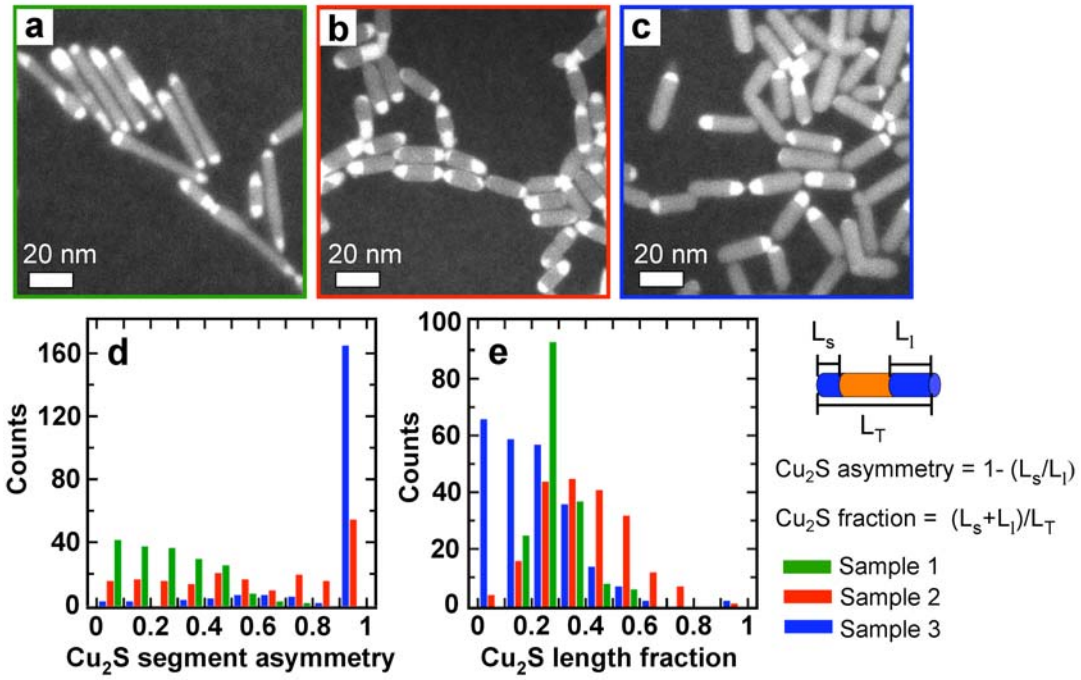

Figure 3.4. Cu-EFTEM images of CdS-Cu_2S binary nanorods and corresponding size statistics of the Cu_2S and CdS regions. The bright regions in the images correspond to Cu_2S and the grey regions to the CdS portions of the nanorods. The green, red, and blue bars in the histograms correspond to samples 1, 2, and 3 shown in (a), (b), and (c), respectively. The three samples were made under the following conditions: (a) Sample 1: initial CdS nanorods with dimensions of 48×6 nm and fast addition to the Cu^+ solution, (b) Sample 2: CdS nanorods with dimensions of 29×9 nm and fast addition to the Cu^+ solution, and (c) Sample 3: The same initial nanorods as 2, but with slow addition of Cu^+ ions. (d) Histograms of the asymmetry of the Cu_2S segment lengths on the ends of the nanorods for the three samples. (e) Histograms of the Cu_2S length fraction within the binary nanorods. The asymmetry and length fraction of the Cu_2S segments are defined to the right.

Sample 3 used the same initial nanorods as sample 2, but the Cu^+ solution was added drop-wise via a syringe pump to the CdS solution. Slowing the rate of addition of Cu^+ cations to the CdS nanorods has several significant effects on the morphology of the CdS-Cu_2S heterostructures. First, it greatly enhances the asymmetry of the heterostructures leading to a majority of nanorods with Cu_2S only on one end as shown in Figure 3.4c (sample 3, mean asymmetry = 0.91). It also widens the distribution of the fraction exchanged among the individual nanorods within sample 3 (see Figure 3.4e). Thus, the disparity of Cu_2S segment sizes both within individual nanorods and among the different nanorods in a sample increases from sample 1 to 2 to 3. Finally, sample 3 has fewer nanorods with interfaces that are at an angle to the cross-section of the nanorod (~15% for sample 3 versus ~30% for sample 2). Thus, the slow addition of Cu^+ cations appears to increase the selectivity for nucleation of one CdS-Cu_2S interface per nanorod that is parallel to the nanorod cross-section.

The basic morphology of the CdS-Cu_2S binary nanorods is similar for different degrees of conversion. In Figure 3.5b the asymmetry of Cu_2S segment lengths for individual nanorods are plotted versus the length fraction of Cu_2S they contain. A weak correlation can be seen where the asymmetry between the Cu_2S ends segments tends to decrease as the fraction of Cu_2S increases in a particular nanorod. Thus, while the three samples shown in Figure 3.4 possess different distributions of Cu_2S within the nanorods (see Figures 3.4e and 3.5c), the conversion fraction does not appear to play a significant role in determining the overall asymmetry of the binary nanorods. Figure 3.6 shows EFTEM images and corresponding size statistics for CdS-Cu_2S heterostructures made

with different Cu^{+}/Cd^{2+} ratios. As the Cu^{+}/Cd^{2+} cation ratio increases, there is a small decrease in the average asymmetry of the resulting heterostructures (see Figure 3.6c). However, the main effect of increasing the Cu^{+}/Cd^{2+} ratio was to increase the percentage of fully converted Cu_2S nanorods (see Figure 3.6d).

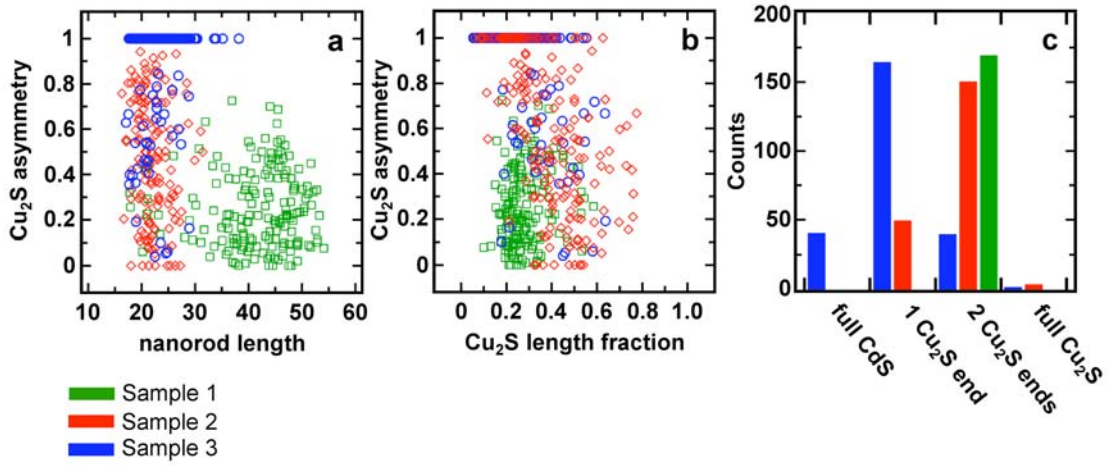

Figure 3.5. The dependence of Cu_2S segment asymmetry on nanorod length and conversion fraction and the populations of the different nanorod morphologies produced. The color coating in Figure 3.6 is the same as 3.4 where green corresponds to Sample 1, red to Sample 2, and blue to Sample 3. (a) Plot of the asymmetry of the Cu_2S end segments of individual CdS-Cu_2S nanorods versus the length of the nanorod for the three samples shown in Figure 3.4. (b) Plot of the asymmetry of the Cu_2S ends segments of individual CdS-Cu_2S nanorods versus the Cu_2S length fraction of the nanorod for the three samples shown in Figure 3.4. A weak correlation can be seen where the asymmetry decreases for higher Cu_2S conversion within the nanorod. (c) Population of binary nanorods for the three samples shown in Figure 3.4. After Cu^{+} exchange the samples can contain a mixture of unreacted CdS nanorods, nanorods with Cu_2S on one end, nanorods with Cu_2S on both ends, and fully converted nanorods.

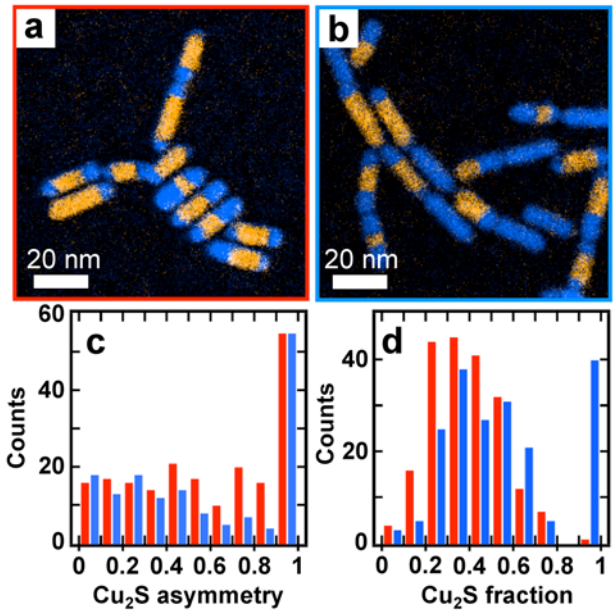

Figure 3.6. EFTEM composite images of CdS-Cu_2S binary nanorods made with different Cu^+/Cd^{2+} ratios and the corresponding statistics of the Cu_2S and CdS regions. (a) EFTEM composite image for CdS-Cu_2S heterostructures made with a Cu^+/Cd^{2+} ratio of ~ 0.55. (b) EFTEM composite for CdS-Cu_2S heterostructures made with a Cu^+/Cd^{2+} ratio of ~ 0.76. Orange regions correspond to the Cd mapping and blue to the Cu mapping. (c) Histograms of the asymmetry of the Cu_2S segment lengths on the ends of the nanorods for the two cases. (d) Histograms of the Cu_2S length fraction within the binary nanorods. For each histogram the red bars correspond to the sample shown in (a) and the blue bars to the sample shown in (b).

3.3 Modeling the CdS-Cu_2S Epitaxial Attachments

The nucleation and growth of Cu_2S within a CdS nanocrystal involves complex atomic motions making the microscopic mechanism for the solid-state reaction relatively difficult to model. However, the formation energies for CdS-Cu_2S interfaces created at different facets of the CdS crystal give a measure of their relative stability, where interfaces with low formation energies should be observed more frequently. We have constructed models of epitaxial connections between different facets of wurtzite CdS and

chalcocite Cu_2S shown in Figure 3.7. These models were used to calculate interface formation energies, defined as the total energy difference of the supercell containing the interface and its bulk constituents. The values are presented in Table 3.1 and include both chemical formation energies, reflecting the strength of interfacial Cd-S-Cu bonds, as well as the elastic contribution due to lattice distortions from the epitaxial mismatch. The elastic contribution depends on the degree of lattice mismatch between the two facets, the elastic constants of the interfacial atoms, as well the thickness of the cells used in the calculation. Thus, while the values of the elastic energies are geometry dependent, in the CdS-Cu_2S system they are a minor contribution to the total formation energy. Elastic strain becomes a more important contribution in the CdS-Ag_2S system presented in Chapter 4, where the lattice mismatch between crystals is large and differs substantially for different epitaxial attachments.

Table 3.1. Interface formation energies (in eV/per interface unit containing one S atom) for attachments of CdS to Cu_2S.[a]

	End-on CdS ±(0001) to orthorhombic Cu_2S ±(001) $(I_1 + I_2)/2$	End-on CdS $(000\bar{1})$ to orthorhombic Cu_2S (001) (I_1 only)	End-on CdS (0001) to orthorhombic Cu_2S (001) (I_2 only)	Angled CdS ±$(10\bar{1}2)$ to monoclinic Cu_2S ±(001)	Side CdS ±$(10\bar{1}0)$ to orthorhombic Cu_2S ±(001)
Chemical	0.204	0.116	0.292	0.348	0.83
Chemical + Elastic	0.255	0.161	0.349	0.416	0.85

[a] The lattices and facets comprising each interface are listed. The chemical contribution to the formation energy along with the sum of the chemical and elastic contributions are provided for each interface. The elastic contributions were computed assuming the distortions occurred in the Cu_2S lattice only to match the lattice of the CdS. The thicknesses of the Cu_2S cells were 13.5 Å for the end-on and angled attachments and 27.3 Å for the side attachment. The ± symbol indicates that facets with opposite (hkl) or (hkil) indexes comprise the two interfaces in the supercell.

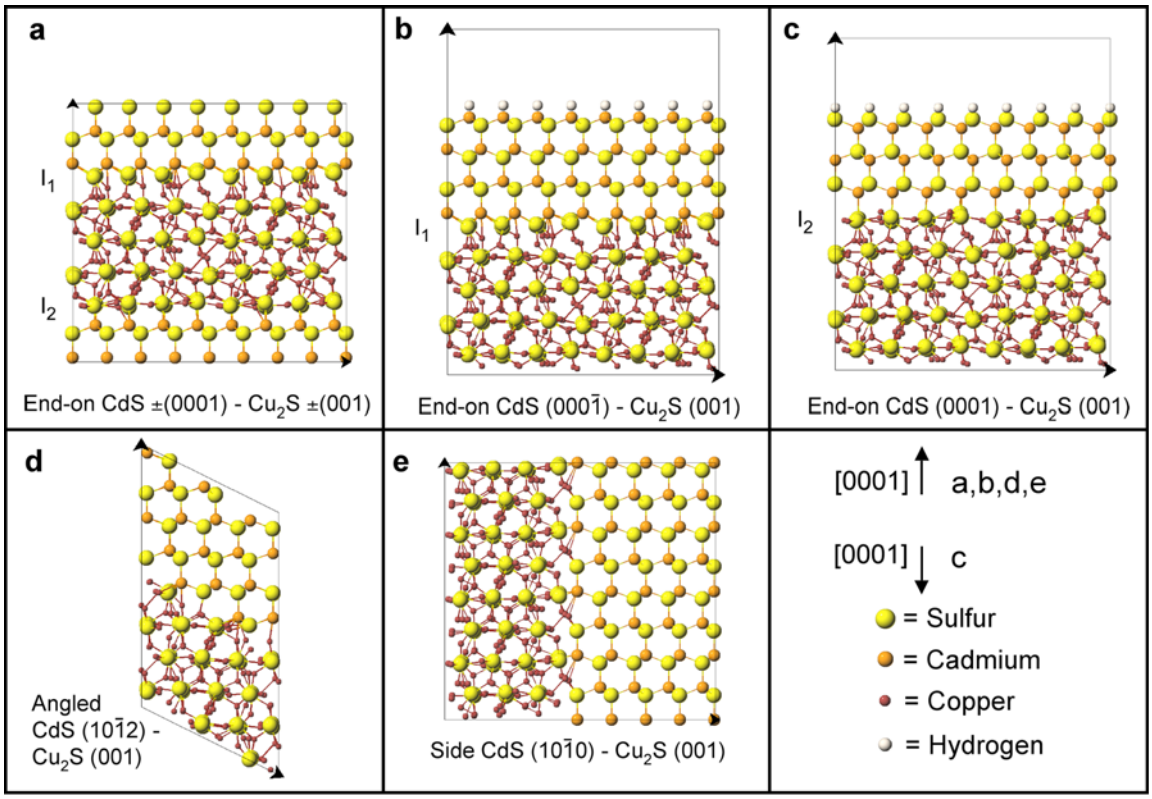

Figure 3.7. Models of the CdS-Cu_2S epitaxial attachments corresponding to the interface formation energies listed in Table 3.1. Two-dimensional projections of the lattices are shown for clarity. (a) End-on, CdS-Cu_2S attachment using the Cu_2S orthorhombic cell. This supercell contains two non-equivalent interfaces labeled as I_1 and I_2. (b) Supercell containing the interface, I_1, connecting Cu_2S to the (000$\bar{1}$) CdS facet. (c) Supercell containing the interface, I_2, connecting Cu_2S to the (0001) facet of CdS. These two supercells also possess CdS and Cu_2S surfaces, which are subtracted out to separate the formation energies for I_1 and I_2. (d) Angled, CdS-Cu_2S interface formed with the original monoclinic Cu_2S lattice connecting to hexagonal CdS. (e) Side, CdS-Cu_2S interface connecting orthorhombic Cu_2S to the (10$\bar{1}$0) facet of CdS.

As the hexagonal close-packed (hcp) sulfur sublattices in CdS and Cu_2S are crystallographically nearly identical,[5] epitaxial attachments can be made by aligning the S atoms in the two crystals. While the unit cell of low chalcocite is monoclinic, it is common to model it as pseudo-orthorhombic, making the symmetry of the lattice easier to visualize.[2,6] To align the c-axes of the hcp sulfur lattices, the [001] axis of the

orthorhombic Cu_2S cell is made parallel with the [0001] axis of the hexagonal CdS lattice. The attachment of orthorhombic Cu_2S to the $(000\bar{1})$ and (0001) end facets of CdS naturally creates interfaces parallel to the cross-section of the nanorod as shown in Figure 3.7a. However, because the CdS lattice lacks inversion symmetry about the c-axis, these two interfaces, labeled as I_1 and I_2, have different epitaxy. In the interface, I_1, connecting Cu_2S to the $(000\bar{1})$ CdS facet, each Cd atom bonds to three S atoms in the interfacial layer. While in the interface, I_2, connecting Cu_2S to the (0001) CdS facet, each Cd atom has one bond to an interfacial S atom.

The supercell geometry used to calculate the interface formation energies implies infinite repetition of alternating CdS and Cu_2S slabs, such that two interfaces are always present. In the case of the supercell in Figure 3.7a, where the bonding arrangement of Cd atoms at the interfacial layer significantly differ for the two attachments, it is necessary to separate their formation energies. To determine the individual energies of these two interfaces we construct the supercells shown in Figures 3.7b and 3.7c, which include a single CdS-Cu_2S interface (I_1 or I_2) and the opposite CdS and Cu_2S surfaces separated by vacuum. The supercell in Figure 3.7b contains the interface I_1, along with a Cd-terminated (0001) CdS passivated surface,[7] and an unpassivated $(00\bar{1})$ Cu_2S surface. The supercell in Figure 3.7c contains the interface I_2, along with a S-terminated $(000\bar{1})$ CdS passivated surface, and the same unpassivated $(00\bar{1})$ Cu_2S surface as in Figure 3.7b. To determine the individual energies for I_1 and I_2 it is necessary to take into account the CdS and Cu_2S surface energies in each supercell as well as the difference in the number of Cu and Cd atoms between the two supercells. The non-equivalent CdS surface

energies are subtracted out from each of the two supercells using auxiliary CdS constructions.[8] The difference in the number of atoms in the two supercells are accounted for by incorporating the chemical potentials of individual Cu and Cd atoms into the bulk chemical potential of the lattices. As the Cu_2S surfaces in the two supercells are the same, their contribution can be removed by taking the difference between the two supercells, leaving on the energy difference between I_1 and I_2. Combining the energy difference between the two interfaces with their average determined from the supercell in Figure 3.7a leads to the desired individual formation energies for Cu_2S attached to the wurtzite CdS (0001) or $(000\bar{1})$ facets. As seen in Table 3.1, the interface I_1 has a chemical formation energy that is about 2.5 times lower than I_2.

Due to the small lattice mismatch between the sulfur lattices of CdS and Cu_2S, the formation energies are determined primarily by the distributions of Cu and Cd atoms at the interface. The optimal geometry for metal atoms bonded to the interfacial layer of sulfur atoms should satisfy local electron counting rules, i.e. each S atom should have a local environment that supplies two electrons in order to fill the sulfur 3*p* bands. While the Cu atoms are somewhat disordered in the interfaces, I_1 and I_2, it can be seen that they form layers parallel to the interface, making it relatively easy to move Cu atoms from one layer to another. By moving four Cu atoms from the Cu layer at interface I_1 to that of I_2, local electron counting is satisfied. However, this is not true for the other CdS-Cu_2S epitaxial connections that we modeled. Due to the relative orientation of the Cu atomic layers to the interface we were not able to satisfy local electron counting rules for

the CdS-Cu_2S interfaces described below, which contributes to their higher formation energies.

Using the original monoclinic lattice for chalcocite Cu_2S, the sulfur lattices can be matched by connecting the ±(001) facets of Cu_2S to the ±(10$\bar{1}$2) facets of CdS (see Figure 3.7d). This interface appears at an angle of ~35° to the nanorod cross-section when viewed along the [100] direction of the Cu_2S lattice, and the apparent angle of the interface will vary with its orientation on the TEM substrate. As the distortions occur primarily in the Cu_2S lattice, we define the orientation of this interface by the angle the CdS (10$\bar{1}$2) plane makes with the nanorod cross-section (i.e. the (0001) CdS plane). Not only does the hexagonal-monoclinic interface have a larger formation energy than I_1 and I_2, but it also produces a greater total interfacial area. A minority fraction of the interfaces were observed at an angle to the nanorod cross-section (< 30 % for fast addition and < 15 % for slow addition of Cu^+). We also modeled the attachment of orthorhombic Cu_2S to the ±(10$\bar{1}$0) side facets of the CdS nanorod. The supercell shown in Figure 3.7e has been extended along the CdS [1000] direction and shortened along the [10$\bar{1}$0] direction for clarity. This interface has a much greater formation energy than the other three connections, and Cu_2S regions were rarely observed on the sides of the nanorods.

3.4 Selective Facet Reactivity of Cu^+ Cation Exchange

In the CdS-Cu_2S system, where the elastic contributions to the interface formation energies are small, the relative values of the chemical formation energies determine the stability of the different CdS-Cu_2S attachments. The end-on Cu_2S attachments, parallel to the nanorod cross-section, possess the lowest chemical formation energies and are the interfaces observed most often by TEM in the binary nanorods. The angled attachment connecting the basal facets of the monoclinic Cu_2S lattice to CdS has both a higher chemical formation energy per interfacial unit and produces a greater interfacial area. Correspondingly, angled interfaces occur at a significantly lower frequency, particularly in the case where the Cu^+ ions are slowly added to the CdS solution. Finally, growth of Cu_2S on the sides of the CdS nanorods is rarely observed, which correlates with the calculated chemical formation energy that is approximately seven times greater than that of end-on connection to the $(000\bar{1})$ CdS facet. The initial nucleation of CdS-Cu_2S interfaces at the ends of the nanorods is a low-energy configuration that is maintained as the exchange front moves along the length of the nanorod. Thus, the basic morphology of the nanorods possessing Cu_2S segments at one or both ends is the same for different conversion fractions. As discussed below, the asymmetry of Cu_2S segment lengths is attributed to the difference in chemical formation energies for the epitaxial attachment of Cu_2S to opposite ends of the nanorods.

The relative interface formation energies also explain why the branch points of bipods and tripods in the nanorods samples are active sites for Cu^+ exchange. As shown in Figure 3.8a, the exposed {111} surfaces of the zinc-blende branch points differ only in

the stacking sequence of the atomic layers to the ±(0001) faces of the wurtzite nanorods.[3] These surfaces also provide a low barrier for interface nucleation, such that Cu_2S grows into the nanocrystal from the edges of the branch point. Figure 3.9b shows a HRTEM image of a bipod nanocrystal with the core and the tip of one arm converted to Cu_2S, illustrating how the morphology of the heterostructures can be controlled through the shape of the initial nanocrystals.

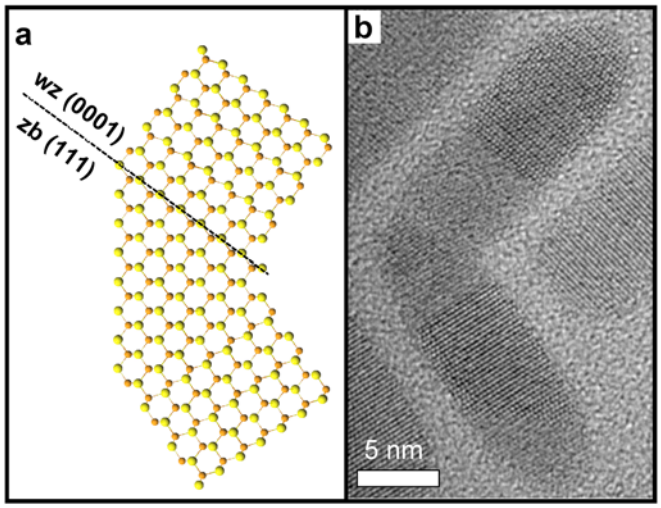

Figure 3.8. CdS-Cu_2S branched heterostructures. (a) Model showing the topotaxial relation between the zinc-blende (zb) core and wurtzite (wz) arms of multipod CdS nanocrystals. (b) HRTEM image of a CdS bipod nanocrystal where the branch point and the end of the lower arm have been converted to Cu_2S.

The relative activation barriers for nucleation at each end of the nanorod control the asymmetry of the Cu_2S segments. In principle, disparate rates of diffusion of cations in opposite directions along the nanorod could also contribute to asymmetric growth. However, previous kinetic studies of cation exchange suggest that interface nucleation

provides the main kinetic barrier for transformation of the nanocrystal.[1] The chemical formation energy for the Cu_2S attachment to the CdS $(000\bar{1})$ facet (I_1) is lower by ~ 0.18 eV per Cd-Cu-S unit compared to attachment to the (0001) facet (I_2). Moreover, the $(000\bar{1})$ end facet of the CdS nanocrystal is believed to be the least stable surface of the nanorod as Cd-termination leads to three dangling bonds per atom, making full passivation difficult without significant surface reconstruction.[9] Therefore, the connection of orthorhombic Cu_2S to the $(000\bar{1})$ end of the nanorods produces the thermodynamically most stable configuration as it both removes a high-energy surface and creates the lowest energy interface. This suggests that the asymmetric CdS-Cu_2S nanorods are produced by selective nucleation of Cu_2S at the $(000\bar{1})$ end of the nanorod.

The increased asymmetry of Cu_2S segments in sample 2 over sample 1 as shown in Figure 3.4 is attributed to the larger diameter and flatter ends of the initial CdS nanorods used to produce sample 2. The shape of the nanorods is kinetically-determined during their growth by the relative rates of monomer addition along different crystallographic directions of the particle.[3,10] Under the non-equilibrium growth conditions used to produce highly anisotropic nanocrystals, the $(000\bar{1})$ and (0001) ends of the nanorods are partially replaced by the more stable $\{10\bar{1}1\}$ type facets leading to pencil or arrow-shaped nanorods.[3] Thus, higher aspect ratio nanorods generally will expose less of the (0001) and $(000\bar{1})$ facets at their ends. The epitaxy of the interface formed during cation exchange will depend on relative areas of the different facets at the ends of the nanorods. The binary nanorods in sample 1 in which the initial nanorods ends have a higher curvature compared to those used to make sample 2 also have a

higher fraction of curved interfaces (see Figure 3.9). Figures 3.9c and 3.9d show HRTEM images of CdS-Cu_2S interfaces for small and large diameter nanorods. While the interface tapers near the edges for the smaller diameter nanorod, it is atomically flat for the larger diameter heterostructure. Nanorods with multi-faceted (curved) end faces expose less of the (0001) and (000$\bar{1}$) surfaces, which may lower the selectivity for interface nucleation at one end. Furthermore, a larger diameter will accentuate the difference in total formation energy between I_1 and I_2. As larger diameter nanorods generally also possess flatter ends, these two parameters act in concert to increase the asymmetry of the Cu_2S segment lengths.

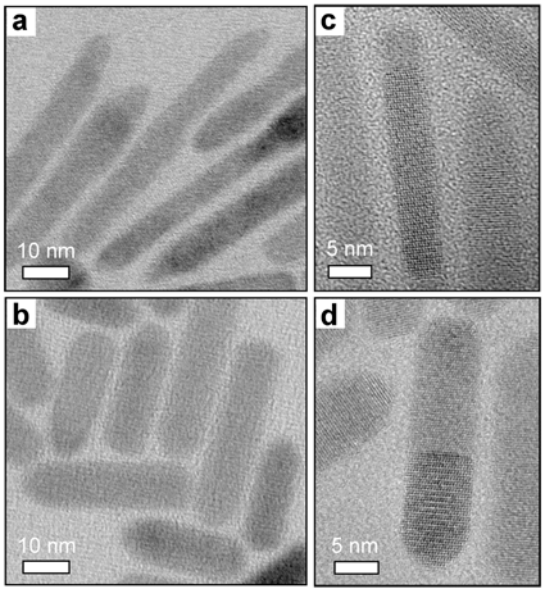

Figure 3.5. TEM images of small and large diameter CdS and CdS-Cu_2S nanorods. (a) The small diameter nanorods used to make CdS-Cu_2S sample 1 have multifaceted (curved) ends. (b) The large diameter nanorods used to make samples 2 and 3 possess primarily flat ends. (c) A CdS-Cu_2S binary nanorod made from the small diameter CdS nanorods, which has an interface that tapers towards the sides. (d) A CdS-Cu_2S binary nanorod made from the large diameter CdS nanorods, which has an atomically flat CdS-Cu_2S interface.

Maintaining a low concentration of Cu^+ ions present in solution during the exchange reaction enhances the formation of a single interface in each binary nanorod. This can be seen as the asymmetry of Cu_2S segments greatly increases for slow (sample 3, Figure 3.4c) versus fast (sample 2, Figure 3.4b) addition of Cu^+ cations to the same initial batch of CdS nanorods. In addition, the percentage of interfaces at an angle to the nanorod cross-section decreases for slow addition. However, the distribution of the fraction converted to Cu_2S among individual nanorods widens, indicating that nucleation and growth of Cu_2S become increasingly overlapped in time. This is expected as the concentration of Cu^+ cations during the early stages of the drop-wise addition is not enough for nucleation to occur on all of the nanorods at once. Previous studies on the reaction kinetics of Ag^+ cation exchange in CdSe nanocrystals support a mechanism where once an interface nucleates in a nanocrystal by cation exchange at the surface, the kinetic barrier for further exchange is relatively low.[1] Thus, upon slow addition of Cu^+ ions, exchange will occur more rapidly at CdS-Cu_2S interfaces that have already formed over the creation of new interfaces, widening the distribution of the Cu_2S fraction among the nanorods. On the other hand, increasing the amount of Cu^+ cations added during rapid mixing of the Cu^+ and CdS solutions decreases the overall asymmetry of Cu_2S segments as shown in Figure 3.6. Thus, a greater initial concentration of Cu^+ ions promotes Cu_2S nucleation on both sides of the nanorod. The high fraction of fully converted nanorods produced with a Cu^+/Cd^{2+} ratio of ~ 0.76 indicates that even with fast mixing, the nucleation and growth of Cu_2S among different nanorods occurs at different times. The temporal separation of nucleation and growth stages is often used to achieve

monodisperse colloidal nanostructures.[11,12] In the present case we have attempted only rapid addition of the CdS and Cu^+ solutions or slow injection of Cu^+ at a constant rate. With further optimization of the rate of Cu^+ addition throughout the course of the reaction it may be possible to maximize the selectivity for nucleation on the $(000\bar{1})$ facet while also separating the nucleation and growth stages to yield a narrow distribution of Cu_2S within the nanorods.

Weak surfactant passivation of the end facets of the CdS nanorods may also contribute to their greater reactivity. Ab initio calculations have shown that the ligands normally used to passivate the surfaces of colloidal nanocrystals, such as amines, phosphonic acids, carboxylic acids, and phosphine oxides bind more strongly to the non-polar $(10\bar{1}0)$-type side facets than to the (0001) or $(000\bar{1})$ end facets.[9,13] As each complete layer of the (0001) and $(000\bar{1})$ facets consists of only Cd or S atoms, the nature of surfactant passivation will strongly depend on the terminating layer. The ab initio calculations also suggest that the (0001) facet is Cd-terminated to minimize the density of dangling bonds, and that the $(000\bar{1})$ facet is not fully passivated. Cd-termination of the $(000\bar{1})$ facet exposes 3 dangling bonds per atom, whereas the Lewis basic ligands listed above should not bind strongly to an S-terminated surface. If the $(000\bar{1})$ facet is the least well-passivated, it will be the most reactive surface. Such, arguments have been used to explain the formation of asymmetric heterostructures consisting of lead selenide (PbSe) or gold (Au) nanocrystals grown selectively at one end of a CdS nanorod.[14,15] However, in these cases, there is not a clear epitaxial relationship between the two materials (CdS with PbSe or Au). Partial cation exchange produces an epitaxial

connection between the secondary and host crystals via the continuity of the underlying anion sublattice. Thus, the formation energies for interface nucleation at different surfaces of the nanocrystal play an important role in determining the relative facet reactivity compared to systems where the growth is not epitaxial.

We found no significant difference in terms of the extent of cation exchange for nanorods synthesized and cleaned using a variety of surfactants, except when excess alkylamine was present in solution, which inhibited the exchange reaction. Alkylamines likely hinder cation exchange by binding to Cu^+ cations in solution, rather than blocking the reaction by adsorbing to the nanocrystal surface. While the reaction occurs instantaneously when only methanol (MeOH) is used to dissolve the Cu^+ salt, the addition of either acetonitrile (MeCN) or octylamine both slow down the reaction and suppressed the fraction of cations exchanged. Cu^+ has a higher solvation energy in MeCN compared to MeOH.[16] As observed in other examples of cation exchange in nanostructures, the primary role of coordinating molecules appears to be adjusting the thermodynamic driving force for exchange by altering the solubility of the host and substitutional cations.[17-19]

Rather than relying labile surfactants to enhance the selectivity for cation exchange at different facets, it may be possible to use a protective inorganic coating. For example, Au can be selectively grown at one end of the nanorod.[15] Following exposure to Cu^+ cations, the opposite end can then be converted to Cu_2S. The Au protective layer may then be selectively etched in order to perform subsequent chemistry at the deprotected facet. Thus, facet-selective solid-state reactions on nanocrystals enable the

ability to perform sequential orthogonal reactions. This is analogous to regioselectivity in organic chemistry, where protective groups are used to selectively block a reaction from occurring at one functional group of the molecule, while another is chemically altered. As both the shape and size of the nanocrystals are defined by the crystallographic facets exposed at the surface, these parameters can be adjusted to control the reactivity of the nanocrystal. For instance, a very different morphology may result during Cu^{+} exchange of CdS nanoplates, which unlike nanorods, primarily expose the (0001) and $(000\bar{1})$ facets at their surface. Selective facet reactivity can in-turn be used to achieve specific physical properties based on the electronic coupling of the two materials and their spatial arrangement within the nanocrystal.

3.5 Chapter 3 Bibliography

(1) Chan, E. M.; Marcus, M. A.; Fakra, S.; ElNaggar, M.; Mathies, R. A.; Alivisatos, A. P. *Journal of Physical Chemisty A* **2007**, *111*, 12210-12215.

(2) Evans, H. T. *Nature Physical Science* **1971**, *232*, 69-70.

(3) Manna, L.; Scher, E. C.; Alivisatos, A. P. *Journal of the American Chemical Society* **2000**, *122*, 12700-12706.

(4) Putnis, A. *American Mineralogist* **1977**, *62*, 107-114.

(5) Cook, W. R., Jr.; Shiozawa, L.; Augustine, F. *Journal of Applied Physics* **1970**, *41*, 3058-3063.

(6) Sands, T. D.; Washburn, J.; Gronsky, R. *Physica Status Solida A* **1982**, *72*, 551-559.

(7) Wang, L.-W.; Li, J. *Physical Review B* **2004**, *69*, 153302-1-4.

(8) Zhang, S. B.; Wei, S.-H. *Physical Review Letters* **2004**, *92*, 086102-1-4.

(9) Manna, L.; Wang, L. W.; Cingolani, R.; Alivisatos, A. P. *Journal of Physical Chemisty B* **2005**, *109*, 6183-6192.

(10) Peng, Z. A.; Peng, X. *Journal of the American Chemical Society* **2001**, *123*, 1389-1395.

(11) Peng, X.; Wickham, J.; Alivisatos, A. P. *Journal of the American Chemical Society* **1998**, *120*, 5343-5344.

(12) Peng, Z. A.; Peng, X. *Journal of the American Chemical Society* **2002**, *124*, 3343-3353.

(13) Puzder, A.; Williamson, A. J.; Zaitseva, N.; Galli, G.; Manna, L.; Alivisatos, A. P. *Nano Letters* **2004**, *4*, 2361-2365.

(14) Kudera, S.; Carbone, L.; Casula, M. F.; Cingolani, R.; Falqui, A.; Snoeck, E.; Parak, W. J.; Manna, L. *Nano Letters* **2005**, *5*, 445-449.

(15) Saunders, A. E.; Popov, I.; Banin, U. *Journal of Physical Chemisty B* **2006**, *110*, 25421-25429.

(16) Chaudhry, M.; Persson, I. *Journal of the Chemical Society, Faraday Transactions* **1994**, *90*, 2243-2248.

(17) Dloczik, L.; Koenenkamp, R. *Journal of Solid State Electrochemistry* **2004**, *8*, 142-146.

(18) Son, D. H.; Hughes, S. M.; Yin, Y.; Alivisatos, A. P. *Science* **2004**, *306*, 1009-1012.

(19) Wark, S. E.; Hsia, C.-H.; Son, D. H. *Journal of the American Chemical Society* **2008**, *130*, 9550-9555.

Chapter 4.

Spontaneous Superlattice Formation in Nanorods Through Partial Cation Exchange

4.1 Strain Engineering in Nanostructures

Lattice mismatch strains are widely known to control nanoscale pattern formation in heteroepitaxy, but such effects have not been exploited in colloidal nanocrystal growth. We demonstrate a colloidal route to synthesizing CdS-Ag_2S nanorod superlattices through partial cation exchange. Strain induces the spontaneous formation of periodic structures. Ab initio calculations of the interfacial energy and modeling of strain energies show that these forces drive the self-organization. The linear arrangement of alternating CdS and Ag_2S segments is shown to be a low energy configuration with high stability against further phase segregation.

The ability to pattern on the nanoscale has led to a wide range of advanced artificial materials with controllable quantum energy levels. Structures, such as quantum dot arrays and nanowire heterostructures can be fabricated by the vapor deposition techniques of molecular beam epitaxy (MBE) and vapor-liquid-solid (VLS) growth,

resulting in quantum confined units that are attached to a substrate or embedded in a solid medium.[1-6] A target of colloidal nanocrystal research is to create these same structures while leveraging the advantages of solution-phase fabrication, such as low-cost synthesis and compatibility in disparate environments (e.g., for use in biological labeling,[7,8] and solution-processed light-emitting diodes[9] and solar cells[10]). One key difference between quantum dots epitaxially grown on a substrate and freestanding colloidal quantum dots is the presence of strain. In epitaxially grown systems, the interface between the substrate crystal and the quantum dot creates a region of strain surrounding each quantum dot, leading to an interaction energy between closely spaced quantum dots. This method of "strain engineering" can be used to spatially pattern quantum dot arrays in two (and even three) dimensions.[3-5] In this paper, we demonstrate the application of strain engineering to colloidal nanostructures, where a single-step chemical transformation produces a regularly spaced array of quantum dots within individual colloidal nanorods.

A linear array of quantum dots within an elongated nanostructure effectively creates a one-dimensional (1D) superlattice, a promising new class of low-dimensional materials.[11-16] 1D superlattices can exhibit radial quantum confinement with strong coupling of electronic states between adjoining segments to produce photon emission from specific regions of the nanowire upon the electrical excitation of charge carriers.[11,13] Their unique geometry allows them to tolerate large amounts of lattice mismatch at the interface between segments without forming dislocations.[17,18] They are also interesting candidates for thermoelectric materials, as they can possess high

electronic mobilities along the nanowire, together with low phonon mobilities due the presence of lattice mismatched interfaces at regular intervals.[12,15,16] Nanowire superlattices composed of GaAs/GaP, Si/SiGe, InAs/InP containing hundreds of repeat units have been fabricated by VLS growth.[11-13] To achieve such structures, gas-phase precursors are alternatively introduced into the reaction chamber containing the substrate for the growth of each layer. Twinning nanowire superlattices, in which there is a regular spacing between rotational twin planes, have also been produced by the periodic addition of a dopant gas during the VLS growth.[14] However, the formation of 1D superlattices by this same time-dependent variation of precursor concentration is out of reach for present colloidal growth techniques. The largest number of alternating layers produced so far is three, and yet the sequence of purifications required in that instance were already taxing to implement.[19,20] An alternative to layer-by-layer growth would be the spontaneous organization of nanoscale materials into a ordered array, in which the pattern naturally emerges from intrinsic interactions of the developing system. Through the chemical transformation of CdS nanorods to CdS-Ag_2S binary nanorods by partial Ag^+ cation exchange, a periodic arrangement results from the interplay of phase segregation and strain-stabilization between the CdS and Ag_2S materials

4.2 Structure and Morphology of CdS-Ag_2S Nanorod Superlattices

As demonstrated in the previous chapter, partial cation exchange in CdS nanocrystals can be used to make epitaxial heterostructures by creating regions of a

secondary material within the host nanocrystal lattice. The resulting organization of materials will strongly depend on the stability of the interfaces that nucleate and grow as the exchange reaction proceeds through the nanocrystal. When there is significant lattice mismatch between the two crystals, the drive to alleviate the increasing elastic strain may produce complex patterns at different stages of the reaction. Such effects are well-known during the strained-growth of lattice mismatched materials on planar surfaces.[1-5] The high mobility of Ag^{+} and Cd^{2+} cations in CdS and the large epitaxial mismatch between the wurtzite CdS and monoclinic Ag_2S lattices suggests that partial cation exchange may lead to interesting patterns of segregated domains of Ag_2S within the host CdS nanorod.

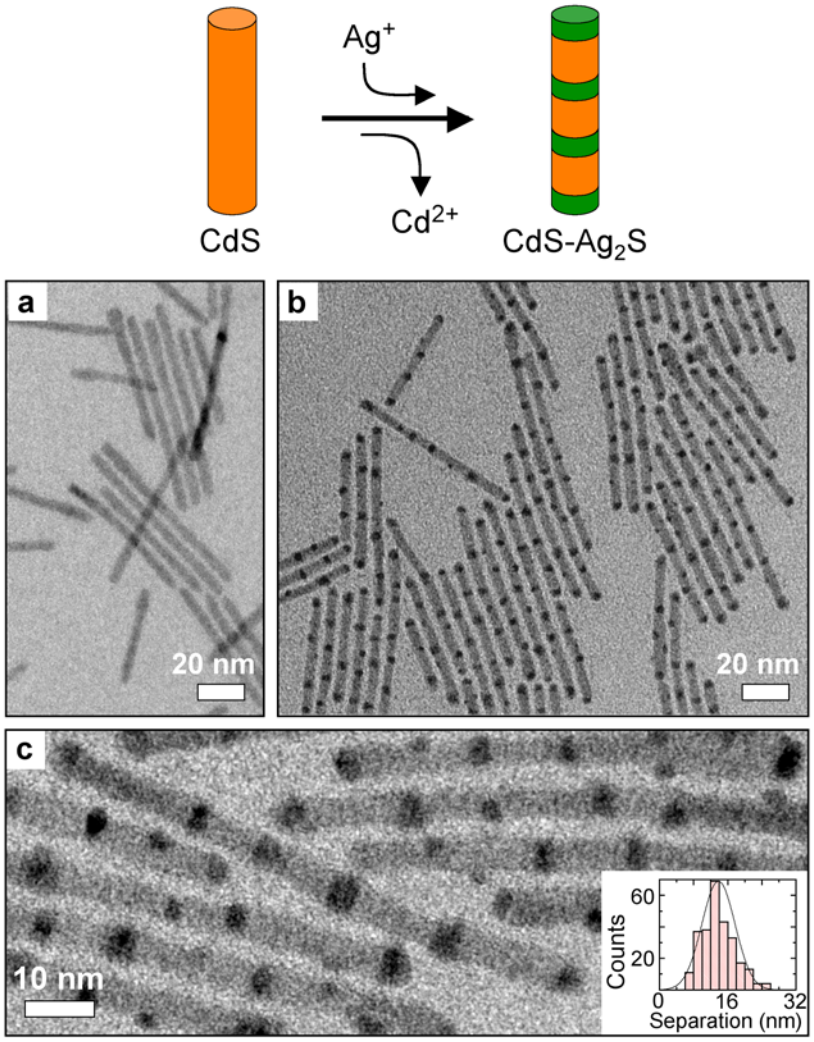

Figure 4.1. TEM images of nanorod superlattices formed through partial cation exchange. (a) The initial 4.8×64 nm CdS nanorods. (b, c) CdS-Ag_2S superlattices produced by partial Ag^+ cation exchange. The inset to (c) is a histogram of the Ag_2S segment spacing (center-to-center). The average spacing of the Ag_2S segments is 13.8 ± 3.8 nm.

TEM images of CdS-Ag_2S heterostructures made by partial Ag^+ cation exchange of CdS nanorods are shown in Figure 4.1. In these experiments the initial CdS nanorods (Figure 4.1a) were exceptionally smooth with a well-controlled diameter (average diameter = 4.8 nm with a standard deviation of 10%), while the length varied between

30 – 100 nm (average length = 64 nm). The colloidal CdS nanorods were added to a solution of toluene, $AgNO_3$, and methanol at -66°C in air. The ratio of Ag^+ cations to Cd^{2+} within the nanorods was varied systematically to observe changes in the binary nanorod morphology. In the presence of excess Ag^+, the nanorods are completely converted to Ag_2S.[21] However, when the Ag^+/Cd^{2+} cations ratio was ~ 0.9, the resulting nanorods display a periodic pattern of light and dark segments (Figures 4.1b and 4.1c). The volume fraction of Ag_2S within the CdS nanorods was measured to be ~ 36%, meaning that the majority of the Ag^+ cations added to the CdS solution exchange into the nanocrystals (as 2 Ag^+ cations are needed to replace each Cd^{2+} cation). The average spacing between the Ag_2S segments is 13.8 nm with a standard deviation of 28% (see the histogram inset in Figure 4.1c).

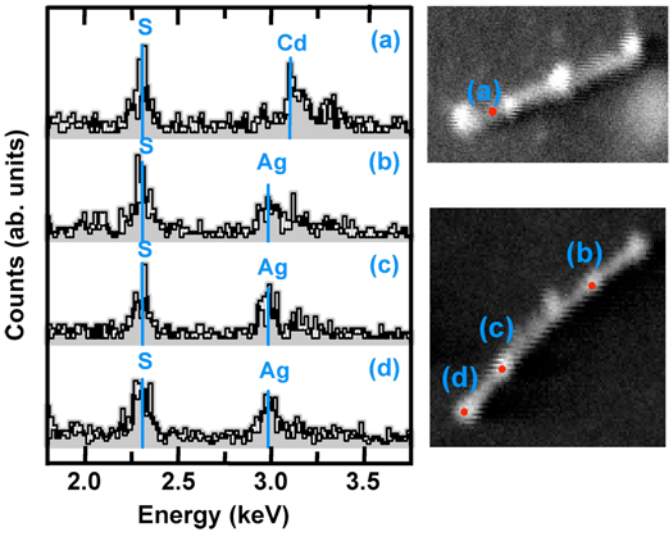

Figure 4.2. EDS spectra of the CdS-Ag_2S nanorod heterostructures, showing the alteration of Cd-S and Ag-S rich regions along the length of the nanorods. The spots where the EDS spectra were taken are shown in the TEM images on the right. The contrast of these images is opposite of the bright-field images shown in Figure 4.1.

Examination of the alternating light and dark regions observed in the partially converted nanorods confirms they are composed of CdS and Ag_2S, respectively. Energy-dispersive x-ray spectroscopy (EDS) indicates that the nanorods alternate between Cd-S and Ag-S rich regions (Figure 4.2). A minority of segments are Ag-rich with little or no sulfur, due to reduction of the Ag_2S crystal by electron beam irradiation as has been previously observed for Ag_2S quantum dots.[22] Electron beam damage also distorts the Ag_2S phase, preventing the acquisition of high-resolution TEM images of the composite nanostructures. However, XRD measurements confirm the presence of hexagonal CdS and monoclinic Ag_2S in the binary nanorods as shown in Figure 4.3. Figure 4.3 shows a comparison of the XRD patterns of the initial CdS nanorods, CdS-Ag_2S heterostructures, and fully converted Ag_2S nanorods. Diffraction peaks appearing in the original nanorods belong to wurtzite CdS (JCPDS #41-1049), while those in the fully exchanged nanorods are indexed to Acanthite, the low-temperature phase of Ag_2S (JCPDS #14-0072). The XRD peaks apparent in the partially exchanged nanorods are purely a combination of these two phases. Furthermore, simulations of the XRD pattern for a mixture of Ag_2S and CdS crystalline domains with dimensions matching that in the sample agree qualitatively with the experimental pattern. The relative intensities of Ag_2S to CdS peaks are similar in the experimental and simulated patterns supporting the extent of the conversion as measured from TEM images. In the experimental XRD pattern, the CdS (0002) peak is broader and weaker for the CdS-Ag_2S nanorods compared to the initial CdS sample. Such a change is expected, as the presence of the Ag_2S segments interrupts the continuity of the CdS (0001) planes perpendicular to the long axis of the nanorod.[23,24] Debye-Scherrer analysis of the XRD peak widths for the

CdS-Ag_2S nanorod sample indicates that the CdS grain size along the axis has decreased from > 30 nm to 12-16 nm. This change qualitatively agrees with TEM measurements, where the initial CdS nanorod dimensions were 5.3×50 nm, while the resulting CdS-Ag_2S heterostructures contained 5.3×11 nm CdS grains.

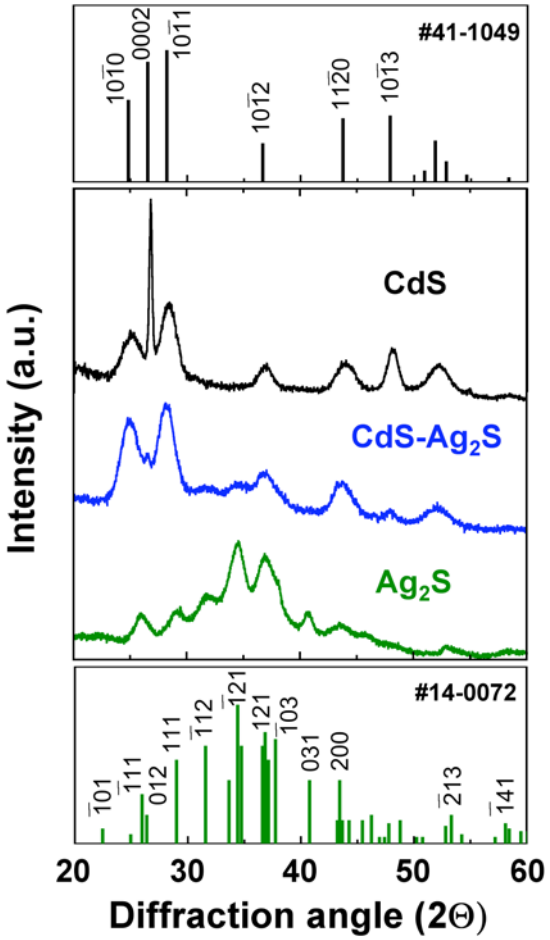

Figure 4.3. XRD spectra of the initial CdS (black), partially exchanged CdS-Ag_2S (blue), and fully converted Ag_2S (green) nanorods. JCPDS patterns for wurtzite CdS (top, JCPDS # 41-1049) and acanthite Ag_2S (bottom, JCPDS # 14-0072) are included for reference.

TEM images show that the Ag_2S regions, which have a broad range of separations at low Ag^+/Cd^{2+} ratios (Ag^+/Cd^{2+} = ~ 0.2, Figure 4.4a), become increasingly ordered at higher Ag^+ concentrations (Ag^+/Cd^{2+} = ~ 0.9, Figure 4.4b). The change in the number and periodicity (spacing) of the Ag_2S regions suggest a systematic organization of the two materials as the volume fraction of Ag_2S increases (Figures 4.4c-f). The number of Ag_2S regions per nanorod decreases as the fraction converted increases, indicating merging of the small Ag_2S regions to form larger segments. Intra-rod Ag_2S separations were correlated through a pair distribution function where the distances between each Ag_2S region and all other Ag_2S regions for a given nanorod were measured. Organization of the CdS and Ag_2S materials to form the nanorod superlattices is seen as the periodicity of the pair distribution histogram (Figure 4.4f) extends over several nearest neighbor distances. In the superlattices the Ag_2S segments are spaced evenly within each nanorod, while no periodicity is apparent for the lower Ag^+ concentration (Figure 4.4e).

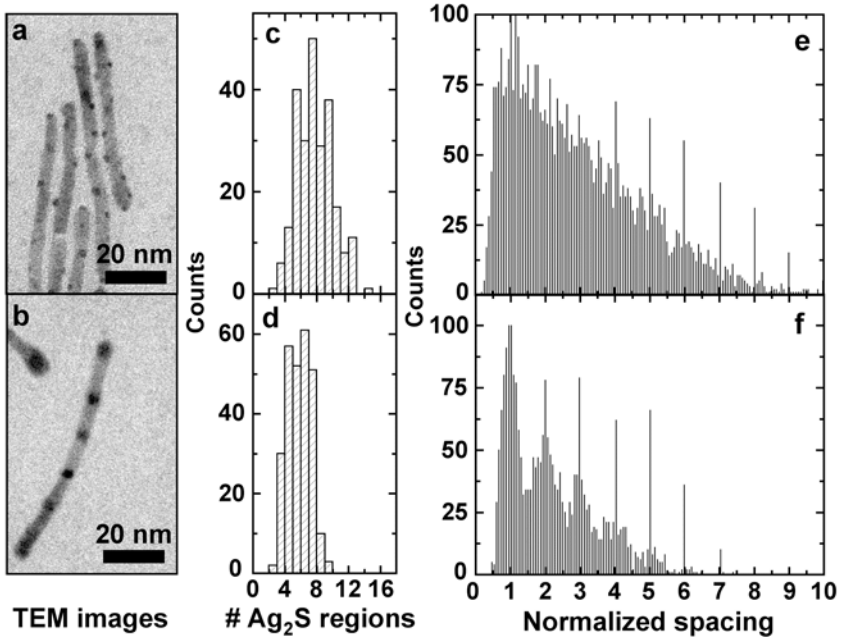

Figure 4.4. Organization of the Ag_2S regions with increasing Ag^+/Cd^{2+} ratio. TEM images: (a) Low concentration (Ag^+/Cd^{2+} ~ 0.2). (b) Intermediate concentration that produces the nanorod superlattices (Ag^+/Cd^{2+} ~ 0.9). Histograms of the number of Ag_2S regions per nanorod: (c) Low concentration and (d) intermediate concentration. Pair distribution histograms for Ag_2S regions in individual CdS-Ag_2S nanorods: (e) Low concentration and (f) intermediate concentration. Intra-rod distances between each Ag_2S region in a given nanorod were measured for 200 nanorods for the two samples shown in (a) and (b). The spacings were normalized by the number of Ag_2S regions and the length of the nanorod. The nanorod heterostructures produced by the low Ag^+/Cd^{2+} ratio (e) shows no correlation beyond the nearest neighbor spacing. The intermediate Ag^+/Cd^{2+} ratio (f) produces CdS-Ag_2S superlattices where the Ag_2S segments display a periodicity extending over several nearest neighbors.

The periodicity of the Ag_2S segments can be controlled with the dimensions of the initial nanorod. As shown in Figure 4.5, for a given number of Ag_2S segments per nanorod, the spacing between Ag_2S segments increases with nanorod length. However, longer nanorods also tend to contain a greater number of Ag_2S segments. For a given nanorod length, the spacing between Ag_2S segments decreases with increasing Ag_2S segments per nanorod. Thus, the Ag_2S regions tend to be spaced out evenly within the

nanorod, rather than each superlattice having the same periodicity. The spacing between Ag_2S segments also increases with the diameter of the initial CdS nanorods. As shown in Figure 4.6, the average nearest neighbor Ag_2S spacing increases from 14 nm for 4.8 nm diameter nanorods to 16 nm for 5.3 nm diameter nanorods. These observations suggest the presence of a repulsive force between Ag_2S segments, which scales with the interfacial area.

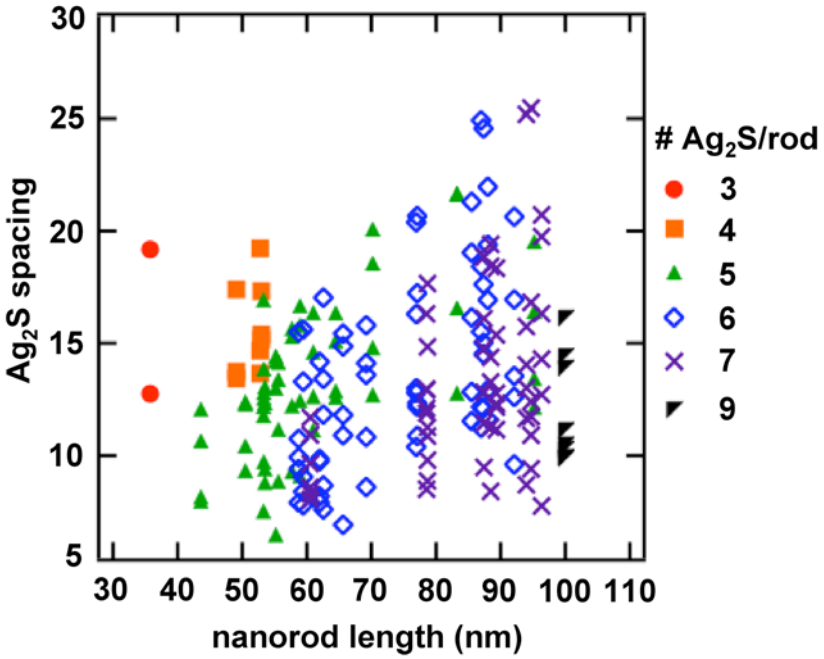

Figure 4.5. Ag_2S segment separation versus nanorod length and the number of Ag_2S regions per nanorod. Individual center-to-center spacings between nearest neighbor Ag_2S segments on a given nanorod are plotted. Spacings at a particular length are measured from the same nanorod to show the distribution of Ag_2S separations for that nanorod. The measurements are labeled according to the number of Ag_2S segments within the nanorod (see legend to the right of the plot).

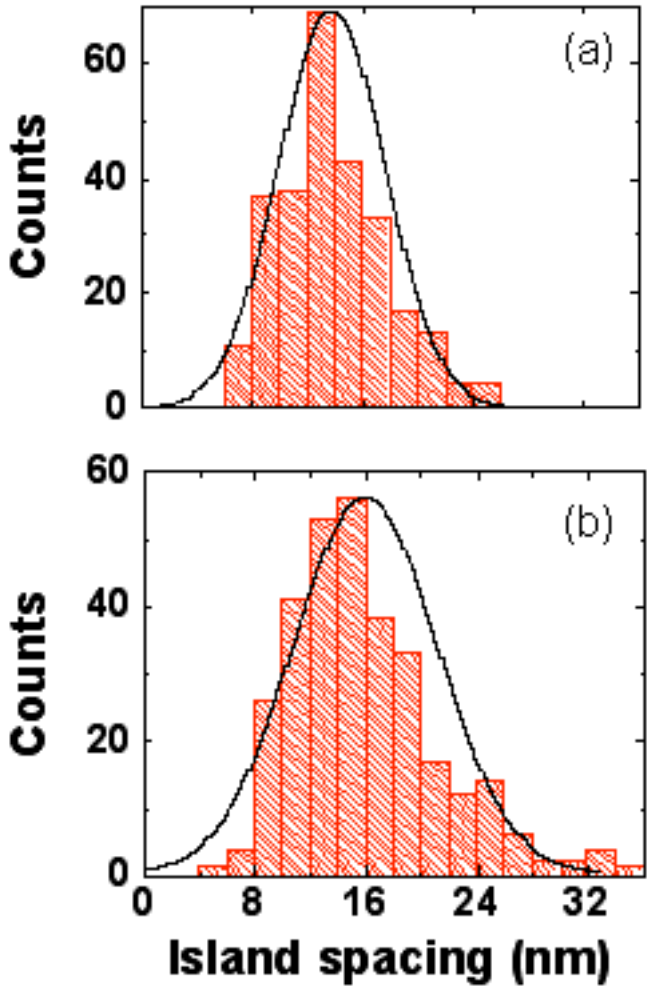

Figure 4.6. Diameter dependence of Ag_2S segment spacing for superlattices made with CdS nanorods of different initial diameters. (a) 4.8 nm diameter CdS rods have an average spacing of 13.8 nm between Ag_2S segments. (b) The spacing increase to 16 nm in 5.3 nm diameter CdS rods. The center-to-center distance between nearest neighbor Ag_2S segments was measured.

Not only is the distance between Ag_2S segments uniform within each nanorod, but also their segment length along the nanorod (i.e. the spacing between CdS segments). Figure 4.7 shows the distribution of Ag_2S segment sizes for the nanorod superlattices

shown in Figure 4.1. Interestingly, for nanorods of different diameters, the Ag_2S segment sizes along the length of the nanorod are very similar to their diameter through the cross-section of the nanorod. For example, starting with CdS nanorods with an average diameter of 4.8 nm, the average Ag_2S segment length in the superlattices is also 4.8 nm. This suggests that once the Ag_2S segments span the diameter of the nanorod, further growth of the segments along the length is hindered.

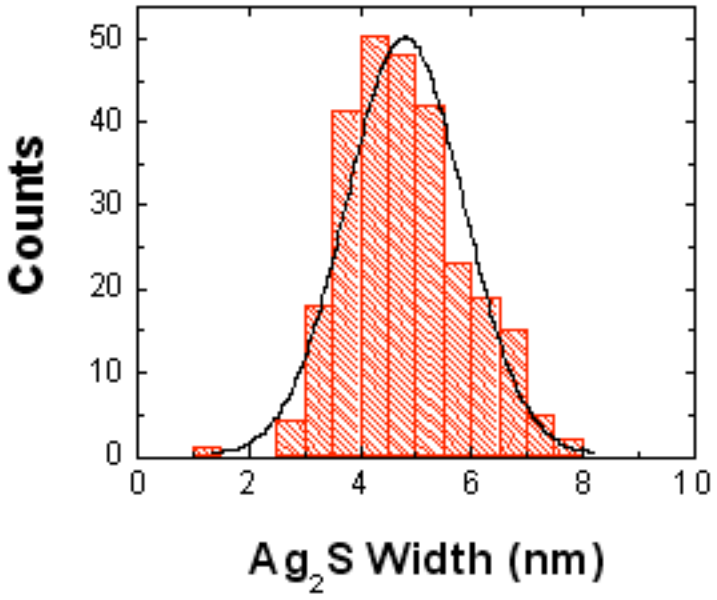

Figure 4.7. Histogram of Ag_2S segment lengths (measured along the length of the nanorod) for the nanorod superlattices shown in Figure 4.1. The average segment length is 4.8 nm with a first standard deviation of 22%.

4.3 Modeling the CdS-Ag_2S Epitaxial Attachments

As the Ag_2S regions grow into the nanorods, the increase in interfacial area causes the initially formed reaction fronts to become unstable. For low amounts of Ag^+ added to CdS nanorods ($Ag^+/Cd^{2+} < 0.4$), the small Ag_2S islands embedded in the surface of the nanorod connect with several different facets of the CdS lattice. At higher conversion fractions ($0.5 < Ag^+/Cd^{2+} < 0.9$), the Ag_2S regions form segments that span the diameter of the nanorod, consisting primarily of flat interfaces parallel to the nanorod cross-section. The relative stabilities of the various CdS-Ag_2S interfaces formed as Ag_2S grows into the host nanorod lattice are determined by their formation energies.

To better understand the changes in the CdS-Ag_2S morphology during cation exchange, we have calculated CdS-Ag_2S interface formation energies for epitaxial attachments between different facets of CdS and Ag_2S. The higher the formation energy for a particular interface, the less stable it will be during ripening of the Ag_2S regions. We modeled the epitaxial attachment of the Ag_2S ±(001) and ±(100) facets to the CdS ±(0001) wurtzite facets as well as the Ag_2S ±(001) facets to the CdS ±(10$\bar{1}$0) facets. Models of the three types of CdS-Ag_2S interfaces are shown in Figure 4.8. The corresponding formation energies for these interfaces are tabulated in Table 4.1, which lists both the chemical contribution, reflecting the strength of interfacial Cd-S-Ag bonds, as well as the elastic contribution due to epitaxial strain. Due to the supercell geometry of the models, each calculation includes two interfaces with opposite lattice indices. For example, both the connections of the Ag_2S (100) facet to the CdS (0001) facet as well as the Ag_2S ($\bar{1}$00) facet to the CdS (000$\bar{1}$) facet comprise the supercell in Figure 4.8a.

However, the formation energies of the two interfaces comprising each supercell were not separated as in the CdS-Cu_2S case, as the Ag_2S segments are found to be quite uniform in size.

The first two interfaces, where Ag_2S connects to the CdS (0001) and (000$\bar{1}$) facets, are parallel to the cross-section of the nanorod (Figure 4.8a and 4.8b). These are the dominant type of interfaces found at intermediate exchange fractions ($0.5 < Ag^+/Cd^{2+} < 0.9$), where the Ag_2S segments have grown to span the nanorod diameter. While, the two interfaces have almost the same lattice mismatch, because of the differences in elastic constants and chemical interface energies they slightly have different total (chemical + elastic) formation energies. The formation energies of both of these interfaces are significantly lower than the connection of Ag_2S to the CdS (10$\bar{1}$0) type facets, which are parallel to the sides of the nanorods. Such interfaces are only observed for the Ag_2S islands created at low Ag^+/Cd^{2+} ratios, when the interfacial area for each Ag_2S region is small. Note, that the chemical and elastic contributions to the formation energy are opposite in sign. The chemical contributions are negative for each of the three interfaces meaning that it is energetically favorable to form Cd-S-Ag interfacial bonds. However, the large elastic contributions cause substantial lattice strain as the interfacial area increases.

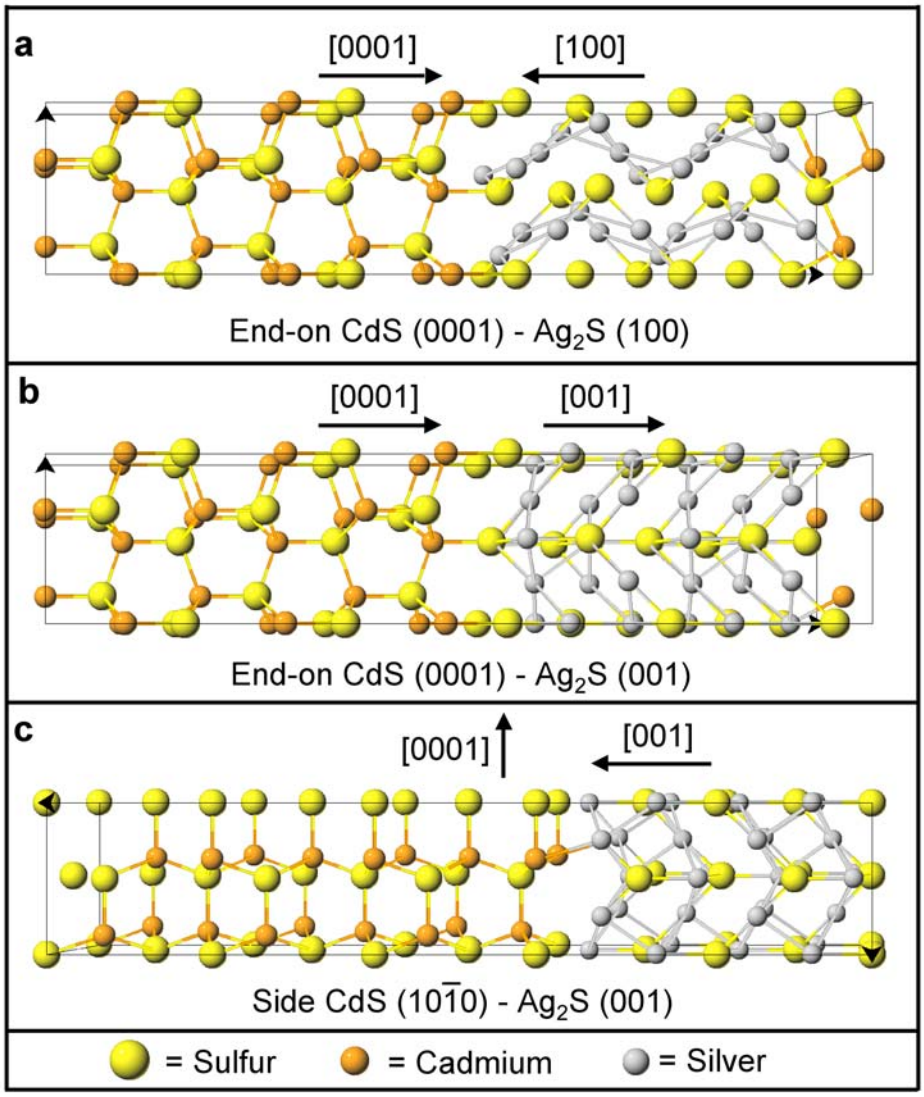

Figure 4.8 Models of the CdS-Ag_2S epitaxial attachments corresponding to the interface formation energies listed in Table 4.1. While only one interface is shown, each supercell is repeated along the long axis of the cell and thus is comprised two interfaces with opposite (*hkl*) or (*hkil*) indices. (a) CdS-Ag_2S attachment of the CdS (0001) and Ag_2S (100) facets, parallel to the cross-section of the nanorod. (d) CdS-Ag_2S attachment of the CdS (0001) and Ag_2S (001) facets, parallel to the cross-section of the nanorod. (e) CdS-Ag_2S attachment of the CdS (10$\bar{1}$0) facet and Ag_2S (001) facet, parallel to the sides of the nanorod.

Table 4.1. Interface formation energies (in eV/per interface unit containing one S atom) for epitaxial attachments of CdS to Ag_2S.[a]

	End-on CdS ±(0001) to orthorhombic Ag_2S ±(100)	End-on CdS ±(0001) to orthorhombic Ag_2S ±(001)	Side CdS ±(10$\bar{1}$0) to orthorhombic Ag_2S ±(001)
Chemical	- 0.87	- 0.3	-1.15
Chemical + elastic	1.57	1.51	2.81

[a] The lattices and facets comprising each interface are listed. The chemical contribution to the formation energy along with the sum of the chemical and elastic contributions are provided for each interface. The elastic contributions were computed assuming the distortions occurred in the Ag_2S lattice only to match the lattice of the CdS. The CdS slab lengths were 19.4Å and the Ag_2S slabs were ~ 15.8 Å in the *z* - direction of the supercell. The slabs are infinite in the *xy* plane. The ± symbol indicates that facets with opposite (hkl) or (hkil) indexes comprise the two interfaces in the supercell. The formation energies were not separated into the two connections that comprise the supercell.

As the total formation energy for each of the CdS-Ag_2S interfaces that we modeled is relatively large, it is energetically favorable to merge the initially small Ag_2S islands into larger Ag_2S segments. Ostwald ripening, which occurs through cation diffusion within the nanocrystal lattice, is particularly facile in these materials due to the high mobilities of Ag^+ and Cd^{2+} within Ag_2S and CdS.[25-28] When the Ag_2S regions grow to span the diameter of the nanorod, the interfaces parallel to the length of the nanorod disappear, which possess the greatest elastic energy (see Table 4.1). At this point, the further ripening of Ag_2S segments is kinetically prohibited, because the atom-by-atom exchange of Ag^+ between two segments will not reduce the total interfacial area until the two segments fully merge. The nanorod heterostructure is in a metastable state, i.e., the complete joining of two Ag_2S regions is always a lower energy configuration, but one that cannot readily be accessed by simple atomic exchange events.

4.4 Mechanism of Spontaneous Pattern Formation

The mechanism by which the initial arrangement of randomly distributed Ag_2S regions evolves into a periodic, 1D pattern is of significant interest for understanding how to control such spontaneous processes. Here, we discuss the role of reaction-diffusion kinetics during the nucleation and growth of Ag_2S within CdS and the strain-induced repulsive interaction between like segments in forming the alternating pattern of CdS and Ag_2S regions. Partial phase segregation both reduces the interfacial area and serves to space the Ag_2S regions out within the nanorod. The elastic distortion at the CdS-Ag_2S interface creates a repulsive interaction between neighboring Ag_2S segments that is minimized when they are evenly spaced within the nanorod

Pattern formation in reaction-diffusion systems far from equilibrium is well-known.[29-32] The relative rates of cations diffusing both in and out of the nanocrystal and through the lattice leads to the distributed formation of Ag_2S regions throughout the nanorod. Cation exchange will much more readily at regions where Ag_2S has already nucleated as there is an energetic barrier towards the formation of new CdS-Ag_2S interfaces.[33,34] Surface exchange is reaction limited, where the nucleation of Ag_2S occurs at a particular site on the nanorod sweeps out a space where all of the available Ag^+ ions will react, leading to a natural spacing of Ag_2S at the surface of the nanorod. As the Ag_2S regions grow into the CdS lattice, they merge to reduce the interfacial area. Because the diffusion of cations within the nanocrystal lattice is much slower than in

solution, it is likely that only Ag_2S segments within a certain separation distance can merge. Thus, the diffusion-limited ripening of Ag_2S segments can further increase the distance between them within the nanorod. However, if the spontaneous ordering were driven by reaction-diffusion kinetics alone, one would expect many nanorod superlattices possessing out-of-place Ag_2S segments, such as two Ag_2S segments very close to each other. For the superlattices shown in Figure 4.1 we observe a minimal spacing of ~ 8 nm for Ag_2S segments that span the entire diameter of the nanorod. This minimum nearest neighbor spacing, along with its dependence on the nanorod dimensions suggests that there is a repulsive interaction between fully formed Ag_2S segments that stabilizes them against merging.

Due to the large lattice mismatch between the CdS and Ag_2S lattices, significant strain fields are present inside the nanorod heterostructure, creating an elastic repulsive interaction between like segments. We describe this repulsive force using the Valence Force Field (VFF) model, which is a classical model for atomic relaxation that treats atoms as points connected by elastic bonds and in our implementation takes into account bond stretching and bending but not bond breaking.[35,36] When the Ag_2S segments span the diameter of the nanorod, the interface is parallel to the nanorod cross-section, such as in the epitaxial models shown in Figures 4.8a and 4.8b. The Ag_2S and CdS lattices must undergo significant distortions in order to epitaxially attach. The Ag_2S lattice constant is 4% smaller in the *x*-direction (i.e. along the [001] or [100] axis of Ag_2S and the [1000] axis of CdS) and 15% larger along the *y*-direction (i.e. along the [010] axis of Ag_2S and the [2100] axis of CdS) compared to that of CdS. Therefore, upon atomic relaxation in

the VFF model, the nanorod will expand and contract along the two perpendicular radial directions (both parallel to the nanorod cross-section).

We performed VFF calculations for CdS-Ag_2S nanorod heterostructures with diameters of 4.8 and 6 nm, which contain two Ag_2S segments at varying separations distances (the Ag_2S segments are both 4 nm along the nanorod length). The resulting elastic energies as a function of the Ag_2S segment separation are shown in Figure 4.9. The elastic energy increases with decreasing separation between the Ag_2S segments as a result of the repulsive interaction between them. The insets of the tail of the curves show the exponential decay of the interaction energy for larger separations. Due to the increased interfacial area for larger diameter nanorods, the strain present in the 6 nm nanorods is greater than that in the 4.8 nm diameter nanorods, resulting in larger elastic energies. For very small separations, the elastic energy is actually lowered, which is due to the anisotropy of the strain fields as explained below.

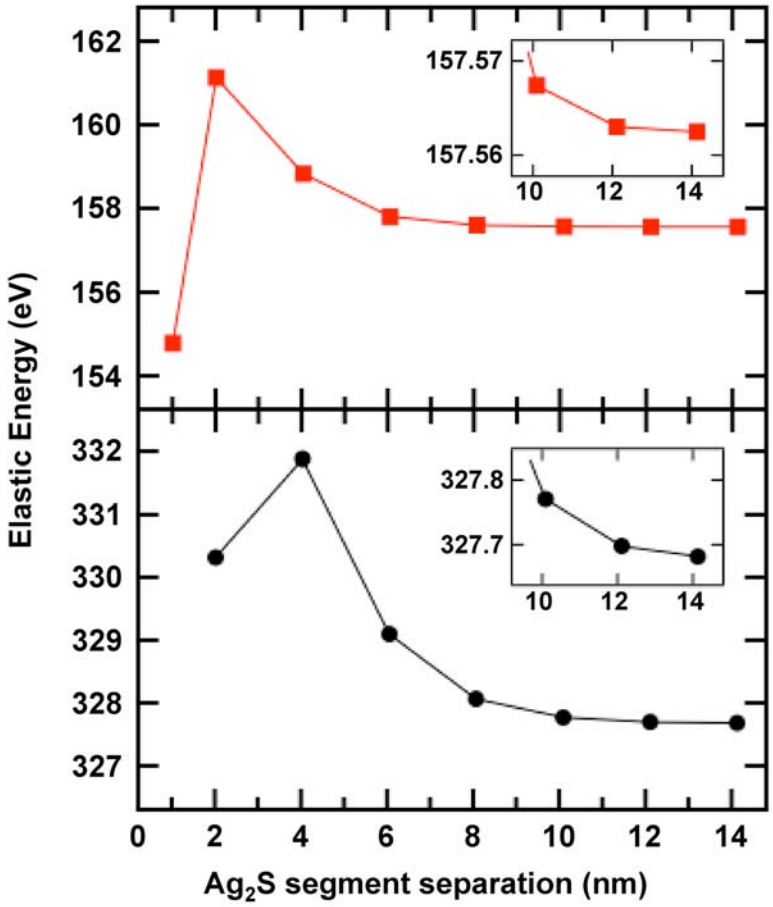

Figure 4.9. Elastic interaction between two Ag_2S segments within a CdS nanorod calculated using the VFF model. (a) 4.8 nm diameter nanorod. (b) 6 nm diameter nanorod. As the segment separation decreases, the interaction between the strain fields of neighboring Ag_2S segments leads to increasing elastic energy. The baseline of the decay curves at infinite separation corresponds to the elastic energy from the epitaxial connection of the CdS and Ag_2S lattices. The insets show the exponential decay of the elastic energy for larger separations.

The strain fields at the interface decay into both the CdS and Ag_2S regions. Therefore, just as the elastic interaction decreases with the length of the CdS regions separating the two CdS-Ag_2S interfaces, it also decreases with increasing Ag_2S segment size (i.e. increased separation between neighboring CdS segments). Introducing asymmetry into the Ag_2S segment lengths results in higher elastic energies. Table 4.2

shows the increase in elastic energy for a nanorod containing 2 Ag_2S segments, as the asymmetry between segment sizes increase along the length of the nanorod. The growth of one fully formed segment at the expense of another is energetically unfavorable, due to the increase in elastic repulsion between the CdS regions on either side of the shrinking Ag_2S. The elastic interaction is minimized when both the Ag_2S and CdS segments are evenly spaced within the nanorods, consistent with the experimental histograms of Ag_2S segment separation and size.

Table 4.2. Elastic energies of CdS-Ag_2S heterostructures as a function of the Ag_2S segment asymmetry calculated in the VFF model. The separation between the centers of the Ag_2S segments is 4 nm

Segment 1 length (nm)	Segment 2 length (nm)	Elastic energy (eV)
4	4	158.83
3	5	159.25
2	6	160.49

To illustrate the elastic interaction between the two Ag_2S segments, color-coded maps of the *z*-component of the bond strain (parallel to the length of the nanorod) for a 4.8 nm diameter nanorod with Ag_2S segment separations of 6, 8, and 10 nm, are plotted in Figure 4.10. Although atomic relaxation in the VFF model produces a 3D tensor strain field, the elastic interaction is evident from the *z*-component along the length of the nanorod, which is greater for smaller Ag_2S segment separation. The red regions between the Ag_2S segments decay away from the interface into the CdS material,

indicating that the atomic bonds are stretched in the *z*-direction, with the degree of distortion increasing radially toward the central axis of the nanorod. This results in the overall deformation of CdS atomic layers in the *xy* plane from flat to convex, as demonstrated by the two layer CdS cutout in Figure 4.10. The deformation pulls the CdS layers on either side of the mid-point between Ag_2S segments in opposite directions, which is the cause of the repulsive interaction. The VFF model also explains why the elastic energy decreases at very small Ag_2S separations (below 2 nm for 4.8 nm diameter nanorods and below 4 nm for 6 nm diameter rods). While the strain fields in *z*-direction between two adjacent Ag_2S segments arise from the bonds being stretched in opposite directions, the atomic distortions in the *xy* plane are in the same direction for small segment separations. This cooperation lowers the strain interaction and leads to an overall decrease in the elastic energy at small segment separations.

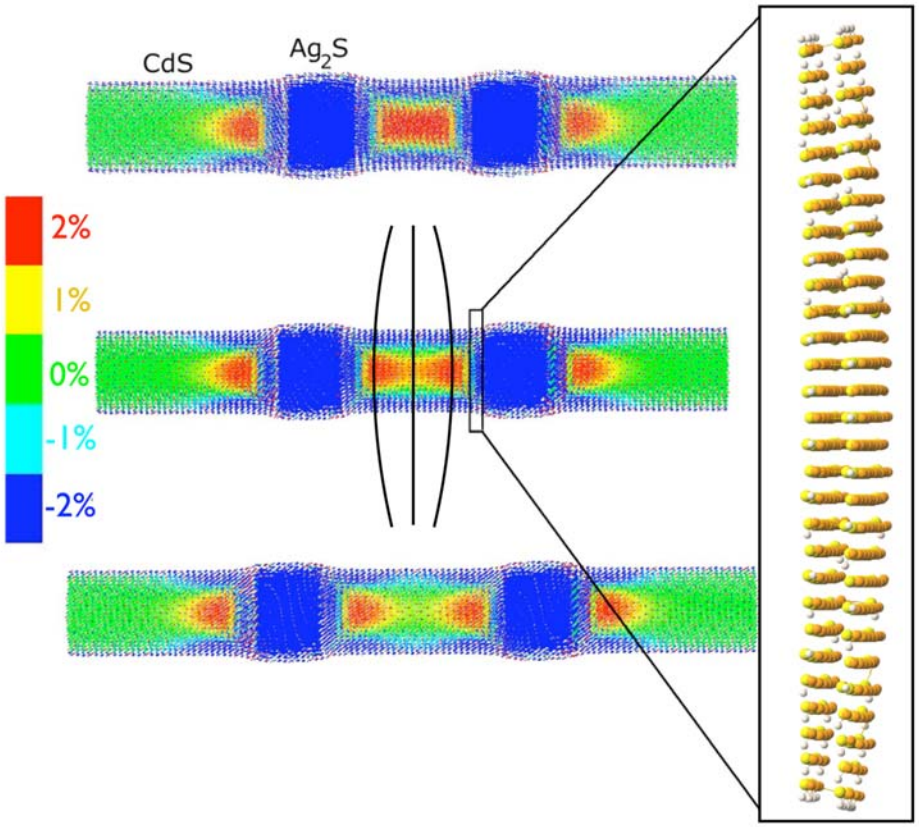

Figure 4.10. Color-coated maps of the *z*-component of strain for 4.8 nm diameter CdS-Ag_2S nanorods, with segment separations are 6, 8, and 10 nm (from top to bottom). The limits of the color map indicate a strain of –2% (compression, blue) to +2% (tension, red). The blow-up on the right shows two layers of CdS adjacent to the Ag_2S segment, illustrating how the layers acquire a convex shape. The atoms are pulled in opposite directions on either side of the mid-point between segments (indicated by the black lines at the center of the second nanorod), which leads to an increasing interaction energy as the segments separation decreases.

As noted above, the CdS-Ag_2S superlattices are a metastable structure. The lowest energy configuration would consist of only two regions, one of Ag_2S and one of CdS, with a single interface between them, as this would minimize both the interfacial and elastic energies. However, such a state cannot be easily reached because once an Ag_2S segment is fully formed within the nanorod, the diffusion of Ag^+ ions to an

adjacent segment will not lower the interfacial energy until the two segments fully merge. Movement of the Ag_2S regions is unfavorable because of the elastic interaction. The elastic repulsion between Ag_2S segments defines the energy barrier between the metastable and the equilibrium configuration. For example, in 6 nm diameter nanorods, this energy can be estimated as 4.2 eV per pair of Ag_2S segments (see Figure 4.9). However, this value represents only the equilibrium difference in energy for nanorods with Ag_2S segments placed at increasingly smaller separations. The kinetic barrier for the diffusion of cations in order to merge the segments may be considerably higher. Although, for a given pair of segments the strain interaction term is about 2 orders of magnitude lower than the interface formation energy, they each play important roles at different stages of formation. The ripening of the initially small and numerous Ag_2S regions occurs in order to lower the interfacial energy. However the final ordering and segment stabilization is determined by the elastic strain interactions, when the interfacial energy at a local minimum and constant for a given number of segments.

The importance of epitaxial strain in attaining the superlattice pattern can be illustrated by examining similar studies of metal ions reacting with semiconductor nanocrystals. Metal-semiconductor nanocrystal heterostructures have been made by reducing Au^+ ions onto InAs quantum dots and CdS and CdSe nanorods.[37-40] As Au^+ has a much greater electron affinity than Ag^+, reduction of the cation takes place rather than exchange with Cd^{2+}. Similar to the CdS-Ag_2S system, small Au regions nucleate over the surface of the semiconductor nanocrystal for low amounts of Au^+ deposited. The positive interfacial energy between Au and the semiconductor promotes phase

segregation of the two materials as the deposition continues. However, there is no clear epitaxial relation between Au and the semiconductor nanocrystal, so the Au regions continues to ripen into a single metal domain, either at the tip of the (CdS/Se) nanorod, or inside the quantum dot (InAs). In contrast, the large epitaxial strain in the Ag_2S-CdS heterostructures causes like segments to repel each other preventing full phase-segregation of the two materials.

The periodic pattern formed during Ag^+ cation exchange in CdS nanorods arises from a combination of the positive interface CdS-Ag_2S formation energies, which drive ripening of the Ag_2S regions and the elastic repulsion, which stabilizes them once they span the nanorod diameter. The large epitaxial mismatch between the CdS and Ag_2S lattices is responsible for both of these phenomena. While such effects may be present during the growth of other nano-scale heterostructures, it is clear that the right balance of forces is needed to produce such well-ordered structures. For instance, Cu^+ cation exchange of the same CdS nanorods leads to quite a different heterostructure morphology. The following chapter compares the morphologies of the CdS-Ag_2S and CdS-Cu_2S binary nanorods in terms of the relative formation energies of the different interfaces observed. Identifying the key parameters responsible for the different morphologies will enable the rational design more complex nano-scale architectures.

4.5 Chapter 4 Bibliography

(1) Guha, S.; Madhukar, A.; Rajikumar, K. C. *Applied Physics Letters* **1990**, *57*, 2110-2112.

(2) Eaglesham, D. J.; Cerullo, M. *Physical Review Letters* **1990**, *64*, 1943-1946.

(3) Notzel, R. *Semiconductor Science and Technology* **1996**, *11*, 1365-1379.

(4) Miller, M. S.; Malm, J. O.; Pistol, M. E.; Jeppesen, S.; Kowalski, B.; Georgsson, K.; Samuelson, L. *Journal of Applied Physics* **1996**, *80*, 3360-3364.

(5) Shchukin, V. A.; Bimberg, D. *Reviews of Modern Physics* **1999**, *71*, 1125-1171.

(6) Law, M.; Goldberger, J.; Yang, P. *Annual Review of Materials Research* **2004**, *34*, 83-122.

(7) Bruchez, M. Jr.; Moronne, M.; Gin, P.; Weiss, S.; Alivisatos, A. P. *Science* **1998**, *281*, 2013-2016.

(8) Chan, W. C. W.; Nie, S. M. *Science* **1998**, *281*, 2016-2018.

(9) Achermann, M.; Petruska, M. A.; Kos, S.; Smith, D. L.; Koleske, D. D.; Klimov, V. I. *Nature* **2004**, *429*, 642-646.

(10) Gur, I.; Fromer, N. A.; Geier, M. L.; Alivisatos, A. P. *Science* **2005**, *310*, 462-465.

(11) Gudiksen, M. S.; Lauhon, L. J.; Wang, J.; Smith, D. C.; Lieber, C. M. *Nature* **2002**, *415*, 617-620.

(12) Wu, Y.; Fan, R.; Yang, P. *Nano Letters* **2002**, *2*, 83-86.

(13) Bjork, M. T.; Ohlsson, B. J.; Sass, T.; Persson, A. I.; Thelander, C.; Magnusson, M. H.; Deppert, K.; Wallenberg, L. R.; Samuelson, L. *Nano Letters* **2002**, *2*, 87-89.

(14) Algra, R. E.; Verheijen, M. A.; Borgstrom, M. T.; Feiner, L.-F.; Immink, G.; van Enckevort, W. J. P.; Vlieg, E.; Bakkers, E. P. A. M. *Nature* **2008**, *456*, 369-372.

(15) Li, D. Y.; Wu, Y.; Fan, R.; Yang, P.; Majumdar, A. *Applied Physics Letters* **2003**, *83*, 3186-3188.

(16) Dresselhaus, M. S.; Dresselhaus, G.; Sun, X.; Zhang, Z.; Cronin, S. B.; Koga, T. *Physics of the Solid State* **1999**, *41*, 679-682.

(17) Ertekin, E.; Greaney, P. A.; Chrzan, D. C.; Sands, T. D. *Journal of Applied Physics* **2005**, *97*, 114325-1-10.

(18) Kastner, G.; Gosele, U. *Philosophical Magazine* **2004**, *84*, 3803-3824.

(19) Milliron, D. J.; Hughes, S. M.; Cui, Y.; Manna, L.; Li, J.; Wang, L.-W.; Alivisatos, A. P. *Nature* **2004**, *430*, 190-195.

(20) Ouyang, L.; Maher, K. N.; Yu, C. L.; McCarty, J.; Park, H. *Journal of the American Chemical Society* **2007**, *129*, 133-138.

(21) Son, D. H.; Hughes, S. M.; Yin, Y.; Alivisatos, A. P. *Science* **2004**, *306*, 1009-1012.

(22) Motte, L.; Urban, J. *Journal of Physical Chemistry B* **2005**, *109*, 21499-21501.

(23) Peng, X.; Manna, L.; Yang, W.; Wickham, J.; Scher, E.; Andreas, K.; Alivisatos, A. P. *Nature* **2000**, *404*, 59-61.

(24) Manna, L.; Scher, E. C.; Alivisatos, A. P. *Journal of the American Chemical Society* **2000**, *122*, 12700-12706.

(25) Schmalzried, H. *Progress in Solid State Chemistry* **1980**, *13*, 119-157.

(26) Woodbury, H. H. *Physical Review* **1964**, *134*, A492-A498.

(27) Desnica-Frankovic, I. D.; Desnica, U. V.; Stotzler, A.; Deicher, M. *Physica B* **1999**, *273-274*, 887-890.

(28) Dutt, M. B.; Sharma, B. L. *Landolt-Boernstein*; Springer-Verlag Series III Vol. 33A, 38-39, **1999**.

(29) Vicsek, T. *Physical Review Letters* **1984**, *53*, 2281-2284.

(30) Cross, M. C.; Hohenberg, P. C. *Review of Modern Physics* **1993**, *65*, 851-1112.

(31) Gaspard, P. *Progess of Theoretical Physics Supplement* **2006**, *No. 165*, 33-56.

(32) Decker, Y. D.; Mikhailov, A. S. *Progess of Theoretical Physics Supplement* **2006**, *No. 165*, 119-143.

(33) Chan, E. M.; Marcus, M. A.; Fakra, S.; ElNaggar, M.; Mathies, R. A.; Alivisatos, A. P. *Journal of Physical Chemisty A* **2007**, *111*, 12210-12215.

(34) Sadtler, B.; Demchenko, D. O.; Zheng, H.; Hughes, S. M.; Merkle, M. G.; Dahmen, U.; Wang, L.-W.; Alivisatos, A. P. *Journal of the American Chemical Society* **2009**, *131*, 5285-5293.

(35) Williamson, A. J.; Wang, L. W.; Zunger, A. *Physical Review B* **2000**, *62*, 12963-12977.

(36) Pryor, C.; Kim, J.; Wang, L. W.; Williamson, A. J.; Zunger, A. *Journal of Applied Physics* **1998**, *83*, 2548-2554.

(37) Mokari, T.; Aharoni, A.; Popov, I.; Banin, U. *Angewandte Chemie International Edition* **2006**, *45*, 8001-8005.

(38) Mokari, T.; Rothenberg, E.; Popov, I.; Costi, R.; Banin, U. *Science* **2004**, *304*, 1787-1790.

(39) Mokari, T.; Sztrum, C. G.; Salant, A.; Rabani, E.; Banin, U. *Nature Materials* **2005**, *4*, 855-863.

(40) Saunders, A. E.; Popov, I.; Banin, U. *Journal of Physical Chemisty B* **2006**, *110*, 25421-25429.

Chapter 5.

Comparison of Cu^+ and Ag^+ Cation Exchange and Extension to Other Systems

5.1 Comparison of Cu^+ and Ag^+ Cation Exchange in CdS Nanorods

The previous two chapters have discussed partial Cu^+ and Ag^+ cation exchange in CdS nanorods in order to create CdS-Cu_2S and CdS-Ag_2S heterostructures. Both exchange reactions occur rapidly and spontaneously at room temperature, such that the fraction converted depends on the M^+/Cd^{2+} ratio (M^+ = Cu^+ or Ag^+). The thermodynamic driving force for cation exchange is attributed to the greater free energy of solvation for divalent Cd^{2+} cations in MeOH compared to the monovalent Ag^+ and Cu^+ cations.[1-5] The solid-state diffusion required for cation exchange is particularly facile in these materials as both Ag^+ and Cu^+ have high diffusion coefficients in their respective sulfides,[6,7] and all three cations have high diffusion coefficients within CdS.[8-10] However, there are considerable differences in the heterostructure morphologies obtained after cation exchange with Cu^+ or Ag^+. The nucleation and growth of Cu_2S or Ag_2S within the CdS nanorods are mediated by the chemical favorability for creating interfacial bonds as well as the structural relationship between the host (CdS) and secondary (Cu_2S or Ag_2S) lattices.

Cation exchange is a single crystal to single crystal transformation. Although, multiple nucleation fronts may develop within the same nanocrystal, the overall shape will be preserved if the anion sublattice maintains its coherency as cations diffuse in and out of the crystal lattice. For example, CdSe nanorods with diameters greater than ~ 4 nm retain their shape following conversion to Ag_2Se.[1] This indicates that the connectivity of the anion sublattice remains in tact during the solid-state transformation, even though the coordinated displacements of the anions are necessary as the selenium sub-lattice has a different symmetry in Ag_2Se compared CdSe. For smaller diameter nanorods, the diameter is comparable to the reaction zone of exchange, and thus the nanorods will reorganize towards their equilibrium (spherical) shape during the transformation process.

The structural difference between the initial and final nanocrystal lattices determine the degree of shape preservation. A smaller change in the lattice volume and symmetry will causes less disruption of the crystal at the reaction front. There is a large expansion of the lattice volume (~14%) during the transformation from CdS to Ag_2S compared to a smaller contraction of the lattice volume (~ 8%) upon conversion to Cu_2S. Furthermore, the sulfur sublattices of CdS and Cu_2S both have hexagonal symmetry while that of Ag_2S has a body-centered cubic symmetry. Thus, for the same initial CdS nanorods, there will be better shape preservation upon complete transformation to Cu_2S as compared to Ag_2S.

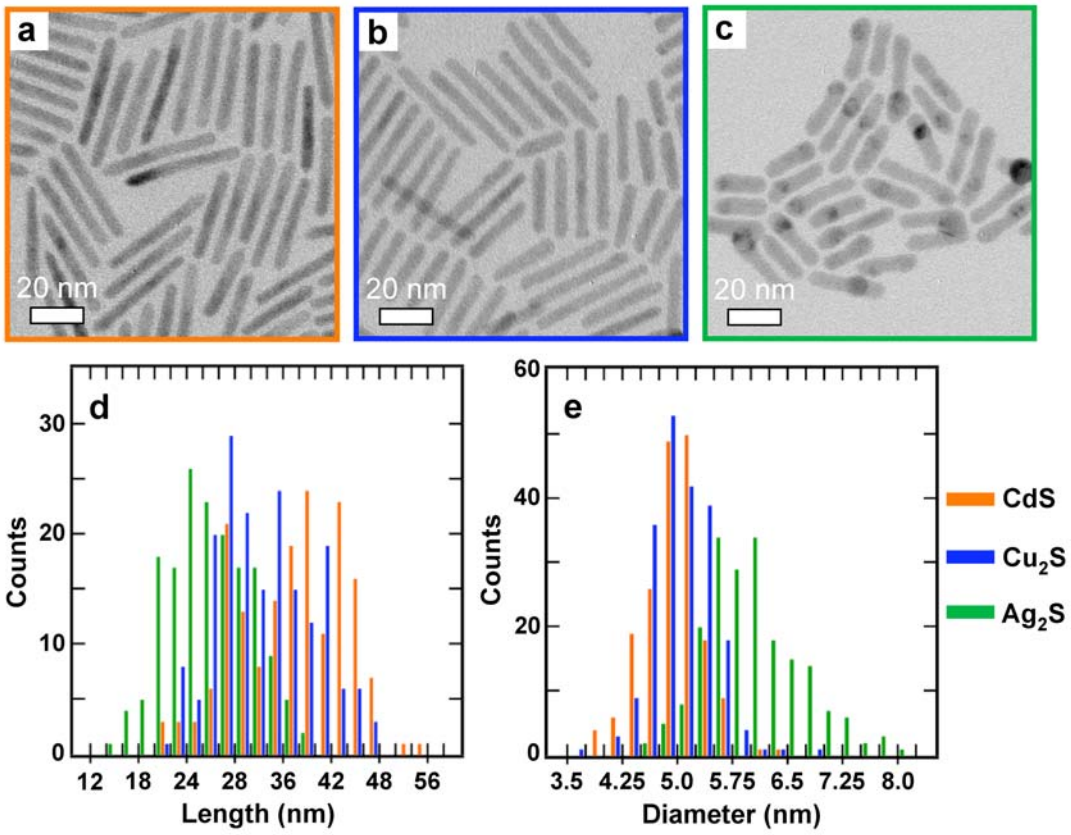

Figure 5.1. TEM images and size distributions of CdS nanorods before and after complete Cu^+ and Ag^+ cation exchange to form Cu_2S and Ag_2S nanorods, respectively. (a) The initial CdS nanorods. (b) Fully-converted Cu_2S nanorods. (c) Fully-converted Ag_2S nanorods. The dark regions in the Ag_2S nanorods are a result of electron beam damage to form Ag^0. (d) Length histograms for the three nanorod samples. (e) Diameter histograms for the three nanorod samples. The orange, blue, and green bars correspond to the CdS, Cu_2S, and Ag_2S nanorods, respectively.

Figure 5.1 shows TEM images and size distributions of the CdS nanorods before and after complete exchange to Cu_2S and Ag_2S. The mean and standard deviation for the length and diameter distributions are: 37±7 × 5±0.4 nm for the initial CdS nanorods, 33±6 × 5±0.4 nm for the Cu_2S nanorods and 27±5 × 6±0.7 nm for the converted Ag_2S nanorods. The changes in the nanocrystal volume are consistent with the bulk changes

in lattice volume listed above. However, there is a significant decrease in the average nanorod length and increase in diameter for conversion to Ag_2S. The decrease in anisotropy is attributed to the larger disruption of the sulfur sublattice during Ag^+ exchange, causing the restructuring of the nanocrystal towards a shape with a lower surface-to-volume ratio.

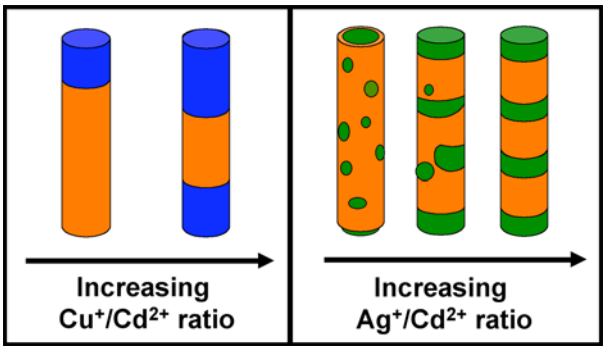

Figure 5.2 Development of the morphology of binary nanorods produced by cation exchange for increasing amounts of Cu^+ or Ag^+ added to CdS nanorods.

The connectivity of the anion sub-lattice is continuous across the interface between CdS and Cu_2S or Ag_2S in partially converted nanocrystals. The nucleation and growth of these interfaces during the exchange reaction will depend on their relative stabilities, where the more stable a particular interface, the more frequently it should be observed. Thus, the heterostructure morphologies for different conversion fractions of the CdS nanorods to Cu_2S or Ag_2S aid in elucidating the movement of the reaction fronts during cation exchange. Figure 5.2 provides a general schematic of the morphological development in the CdS-Cu_2S and CdS-Ag_2S binary nanorods as the Cu^+/Cd^{2+} or

Ag^+/Cd^{2+} ratio increases (for partial exchange the cation ratio is between 0 and 2). A major difference between the two reactions is that the Cu_2S segments are found primarily at the ends of the CdS nanorods at all stages of the conversion, whereas the Ag_2S regions begin randomly distributed and become fewer in number as they grow into the nanorod. Secondly, while the multiple Ag_2S segments within a CdS nanorod are relatively uniform in size once they span the diameter of the nanorod, the two Cu_2S segments can have significantly different lengths. We rationalize the observed differences in the development of heterostructure morphology through the values of the chemical and elastic contributions to the formation energies for the CdS-Cu_2S and CdS-Ag_2S interfaces listed in Table 5.1.

Table 5.1. Comparison of interface formation energies (in eV/per interface unit containing one S atom) for the epitaxial attachment of various facets of CdS to Cu_2S or Ag_2S.[a]

	End-on CdS ±(0001) to orthorhombic Cu_2S ±(001)	Angled CdS ±(10$\bar{1}$2) to monoclinic Cu_2S ±(001)	Side CdS ±(10$\bar{1}$0) to orthorhombic Cu_2S ±(001)	End-on CdS ±(0001) to orthorhombic Ag_2S ±(001)	End-on CdS ±(0001) to orthorhombic Ag_2S ±(100)	Side CdS ±(10$\bar{1}$0) to orthorhombic Ag_2S ±(001)
Chemical	0.204	0.348	0.83	-0.3	-0.87	-1.15
Chemical + Elastic	0.255	0.416	0.85	1.51	1.57	2.81

[a] The lattices and facets comprising each interface are listed. The chemical contribution to the formation energy along with the sum of the chemical and elastic contributions are provided for each interface. The ± symbol indicates that facets with opposite (hkl) or (hkil) indexes comprise the two interfaces in the supercell. These formation energies are not separated into the two connections that alternate along the supercell. The elastic contributions were computed assuming the distortions occurred in the Cu_2S or Ag_2S only to match the lattice of the CdS. The thicknesses of the Cu_2S cells were 13.5 Å for the end-on and angled attachments and 27.3 Å for the side attachment. The Ag_2S thicknesses were ~ 15.8 Å in all cases

There are several notable distinctions between the formation energies of the CdS-Cu_2S and CdS-Ag_2S interfaces that we have modeled. First of all, while the chemical contributions for each of the CdS-Cu_2S formation energies are positive, they are negative for each of the CdS-Ag_2S interfaces. This difference is in part attributed to differences in the bonding character and atomic structure in Cu_2S and Ag_2S. We found that the Cu-S bonds exhibit more ionic character compared to Ag-S bonds, resulting in weaker bonding at the interface, and therefore a greater (more positive) formation energy. Furthermore, while the positions of Ag atoms at the CdS-Ag_2S interface are similar to the optimal positions found in the bulk Ag_2S lattice, relatively large rearrangements of Cu atoms are needed in order for them to connect to the interfacial S layer. These distortions increase the chemical contribution for each of the CdS-Cu_2S interface formation energies. Secondly, the elastic contributions are much smaller for all of the CdS-Cu_2S interfaces compared to the CdS-Ag_2S interfaces due to the smaller mismatch between the CdS and Cu_2S lattices. Furthermore, while the elastic contributions for each of the CdS-Cu_2S formation energies are similar in magnitude, there is a larger energetic difference between the elastic contributions of the side versus end-on CdS-Ag_2S attachments. The importance of these differences in the development of the heterostructure morphology during cation exchange is discussed below.

The relative values of the chemical contributions to the CdS-Cu_2S formation energies govern the favorability for interface nucleation at the various surface facets of the nanorod during Cu^+ cation exchange. As seen in Table 5.1, the elastic contributions to the formation energies are a small fraction of the total formation energy and are of

similar magnitude for each CdS-Cu_2S interface. However, the average chemical formation energy of the two end-on CdS-Cu_2S interfaces is 1.7 times lower than that of the angled interface formed using the monoclinic Cu_2S cell and is 4 times lower than the attachment of Cu_2S to the sides of the CdS nanorods. The chemical formation energies are primarily shaped by the distribution of metal atoms connecting to the interfacial sulfur layer. In the end-on attachments of Cu_2S to the CdS nanorods, the layers of Cu atoms are parallel to the interface making it relatively easy for Cu atoms to bond to the interfacial sulfur layer. However, the attachment of the monoclinic Cu_2S cell to CdS creates an interface at an angle of ~ 35° to both the Cu layers and the nanorod cross-section. In the Cu_2S attachment to the side facets of the nanorods the Cu layers are perpendicular to the interface. These orientations of Cu layers produce a higher chemical formation energy per interface unit. Furthermore, the end-on connections minimize the amount of interfacial area. Correspondingly, the end-on interfaces are observed most often in the nanorod heterostructures compared to the angled and side attachments.

Once the CdS-Cu_2S interfaces have formed at the ends of a nanorod, the interfacial area does not change significantly as the fraction of Cu_2S increases. Thus, they are stable throughout the exchange reaction. However, the end-on connections of Cu_2S to the (0001) and (000$\bar{1}$) CdS facets also have different formation energies (see Table 3.1). As shown in Figure 3.7, in the Cu_2S attachment to the CdS (000$\bar{1}$) facet, the first Cu layer is in between the interfacial S layer and the adjacent one, and each Cd atom bonds to three interfacial S atoms. In the Cu_2S attachment to the CdS (0001) facet,

the first layer of Cu atoms is within the plane of interfacial S atoms, and each Cd atom bonds to only one interfacial S atom. Because of the different formation energies for these two interfaces, nucleation at either end of a nanorod can occur at different stages of the reaction to form asymmetric structures.

The negative chemical formation energies for each of the CdS-Ag_2S attachments favor the creation of Cd-S-Ag interfacial bonds on both the ends and sides of the CdS nanorods, leading to non-selective nucleation. Thus, for low fractions of exchange ($0 < Ag^+/Cd^{2+} < 0.4$), small Ag_2S islands are observed to be randomly distributed over the surface of the CdS nanorods. However, as the Ag_2S regions grow into the CdS lattice, the elastic strain becomes the dominant contribution to the total formation energy. The large elastic contributions make the total CdS-Ag_2S interface formation energies much greater than those for similar CdS-Cu_2S attachments, driving phase segregation of the CdS and Ag_2S materials to reduce the interfacial area. Interfaces with greater elastic contributions will become unstable during the reorganization. Thus, when the Ag_2S regions grow to span the diameter of the nanorod at intermediate conversion fractions ($0.5 < Ag^+/Cd^{2+} < 0.9$), the interfaces parallel to the length of the nanorod disappear, which possess the greatest elastic energy (see Table 5.1). As discussed in the previous chapter, further ripening is kinetically hindered at this point as both the interfacial energy and elastic interaction have reached a local minimum. Thus, non-selective nucleation followed by partial phase segregation produces a metastable configuration consisting of alternating CdS and Ag_2S segments.

It is interesting to note that the Ag_2S segments within a given nanorod are very uniform, even though the epitaxy of Ag_2S with the CdS lattice on either side of the segment are dissimilar. Just as described in Chapter 3 for CdS-Cu_2S interfaces at either end of the nanorod, the non-centrosymmetry of the CdS lattice should lead to different formation energies for Ag_2S attached to the CdS (0001) and (000$\bar{1}$) facets. While Ag_2S does nucleate at the ends of the nanorods, the CdS-Ag_2S interfaces parallel to the nanorod cross-section are primarily formed through ripening of the Ag_2S regions as they grow into the nanorod. Strain repulsion of these segments by the neighboring ones on either side promotes the formation of uniform Ag_2S regions that are evenly spaced within the nanorod. Thus, the elastic repulsive interaction between adjacent interfaces appears to be greater than the energetic difference between the various CdS-Ag_2S interfaces that make up the segmented heterostructure.

We have identified two important parameters that control the heterostructure morphology during cation exchange of ionic nanocrystals. The crystallographic selectivity for nucleation of the reaction front at different facets of the nanocrystal is primarily determined by the chemical formation energy of the resulting interface. The stability of these initial interfaces depends on the change in interfacial area as the secondary material grows within the host nanocrystal lattice. If the elastic strain for a given interface is large, then the interface will become unstable as it grows within the crystal. The preferential nucleation and growth of Cu_2S at the ends of CdS nanorods during Cu^+ exchange is attributed to the high stability of the CdS-Cu_2S interfaces formed at these facets. In comparison, non-selective nucleation in Ag^+ exchange followed by

partial phase-segregation leads to the formation of multiple Ag_2S regions within the nanorod. The relative stabilities of the CdS-Cu_2S and CdS-Ag_2S interfaces that we have modeled correspond well with the frequency with which the corresponding morphologies are observed. In the future, similar modeling of the nano-scale epitaxy may be applied to other material pairs to predict which interfaces are the most stable.

5.2 Extension of Cation Exchange to Other Systems

A number of other cation exchange reactions in ionic nanostructures have been demonstrated. Examples include Hg^{2+} and Pb^{2+} exchange in CdS nanocrystals, Pd^{2+} and Pt^{2+} exchange in CdS, CdSe, and CdTe nanocrystals, and Ag^{+} and Cu^{+} exchange in ZnS nanocolumns.[11-14] Chemical transformations like cation exchange greatly expand the library of nanocrystal shapes, compositions, and morphologies that can be readily synthesized. In principle, any two pair of cations can be interchanged within the ionic lattice of a nanostructure, provided a coordinating molecule is used that strongly solvates the cation within the nanocrystal lattice over that substitutional cation in solution. Simple coordinating solvents (e.g. methanol, acetonitrile, dimethyl sulfoxide) or linear surfactants (e.g. alkylamines, trialkylphosphines, and alkylphosphonic acids) are limited to distinguishing between cations of different oxidation states. However, in the field of host-guest chemistry, a number of macrocyclic molecules with multiple binding sites have been developed, capable of selecting a particular ion based on its size and coordination geometry.[15] Such multi-dentate ligands may be used to increase the

thermodynamic driving force for exchange in cases where the transition metal ions have the same oxidation state and similar solubility. This may be particularly useful in doping semiconductor nanocrystals with magnetic ions such as Ni^{2+} or Co^{2+}.

Through cation exchange, an anisotropic nanocrystal can be converted to a composition that would not naturally grow in the particular shape of the starting material (see Figure 5.3a). For example, synthetic methods exist to grow CdS as nanorods, whereas Cu_2S nanocrystals can be grown as nanodisks.[16,17] Rather than developing new reaction conditions to make CdS nanodisks or Cu_2S nanorods, the conversion from one material to the other via cation exchange can be used achieve nanocrystals of the desired shape and composition. Similarly, sequential partial exchange reactions may be used to obtain a desired combination of heterostructure morphology and composition. For example, nanorods with alternating CdS and PbS segments can be made by partial $Cd^{2+} - Ag^{+}$ exchange followed by $Ag^{+} - Pb^{2+}$ exchange (see Figure 5.3b).

The transformation from one crystal structure to another may be used to trap the final nanocrystal in a phase that is thermodynamically unstable. Ag_2Se nanocrystals made by Ag^{+} exchange of very small CdSe nanocrystals at room temperature possess the high-temperature, superionic conducting Ag_2Se phase, while larger Ag_2Se nanocrystals form in the low-temperature structure.[1] Pd^{2+} and Pt^{2+} exchange in cadmium chalcogenide nanocrystals (CdX, where X = S, Se, or Te) lead to the formation of an amorphous palladium or platinum chalcogenide structure with the same shape and size of the initial nanocrystals.[13] In partial exchange, non-equilibrium phases may be stabilized by the epitaxial connection to the host lattice. For instance, the rock-salt phase of CdSe

nanocrystals is normally stable only at high pressures.[18] However, through Cd^{2+} partial cation exchange of rock-salt PbSe nanocrystals, the CdSe rock-salt phase may form in order to minimize elastic strain at the PbSe-CdSe interface.[19]

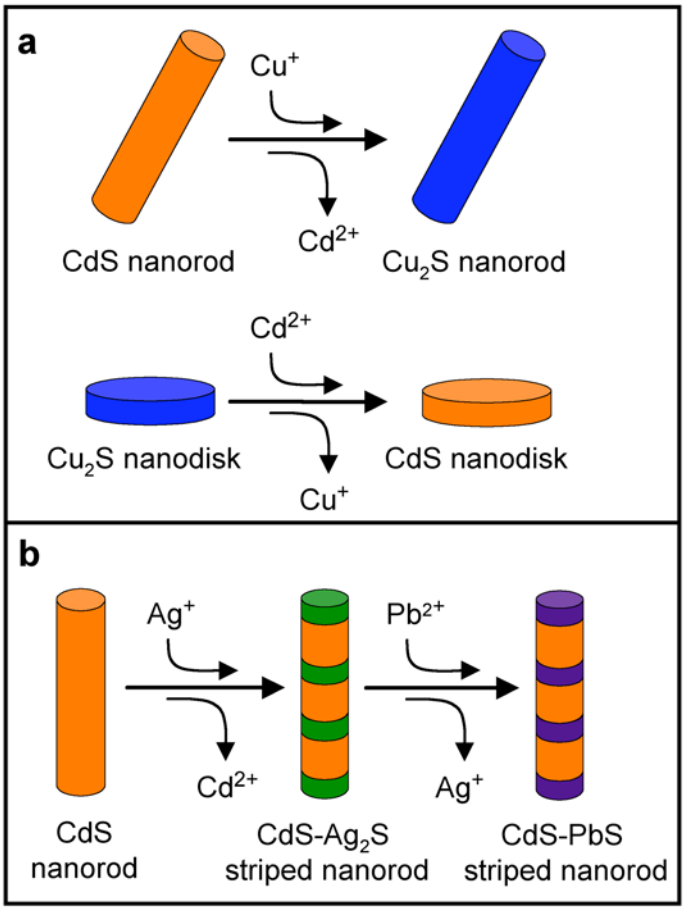

Figure 5.3. Schematic of cation exchange reactions to control the composition and morphology of nanocrystals. (a) Cation exchange of a nanocrystal of a particular shape can be used to achieve a composition that does not naturally grow in the shape of the initial nanocrystal. (b) Sequential partial cation exchange reactions can be used to control the composition and morphology of nanocrystal heterostructures.

The schematic in Figure 5.3 provides examples of how the desired combination of nanocrystal morphology and composition can be achieved through control of the shape and size of the initial nanocrystal and the sequence of exchange reactions. The crystallographic facets exposed at the nanocrystal surface determine its reactivity towards further structural or chemical transformations. Selective facet reactivity can in-turn be used to program specific physical properties in nano-scale heterostructures based on the electronic coupling of the two materials and their spatial arrangement within the nanocrystal. The next chapter details how the optical properties of the CdS-Ag_2S and CdS-Cu_2S nanorod heterostructures can be tailored through control of the electronic band alignment of the two materials and the heterostructure morphology.

5.3 Chapter 5 Bibliography

(1) Son, D. H.; Hughes, S. M.; Yin, Y.; Alivisatos, A. P. *Science* **2004**, *306*, 1009-1012.

(2) Burgess, J. *Metal Ions in Solution*; Ellis Horwood: Sussex, UK, **1978**.

(3) Johnsson, M.; Persson, I. *Inorganica Chimica Acta* **1987**, *127*, 25-34.

(4) Chaudhry, M.; Dash, K. C.; Kamienska-Piotrowicz, E.; Kinjo, Y.; Persson, I. *Journal of the Chemical Society, Faraday Transactions* **1994**, *90*, 2235-2242.

(5) Chaudhry, M.; Persson, I. *Journal of the Chemical Society, Faraday Transactions* **1994**, *90*, 2243-2248.

(6) Schmalzried, H. *Progress in Solid State Chemistry* **1980**, *13*, 119-157.

(7) Berger, R.; Bucur, R. V. *Solid State Ionics* **1996**, *89*, 269-278.

(8) Woodbury, H. H. *Physical Review* **1964**, *134*, A492-A498.

(9) Desnica-Frankovic, I. D.; Desnica, U. V.; Stotzler, A.; Deicher, M. *Physica B* **1999**, *273-274*, 887-890.

(10) Dutt, M. B.; Sharma, B. L. *Landolt-Boernstein*; Springer-Verlag Series III Vol. 33A, 38-39, **1999**.

(11) Mews, A.; Eychmuller, A.; Giersig, M.; Schooss, D.; Weller, H. *Journal of Physical Chemisty* **1994**, *98*, 934-941.

(12) Zhou, H. S.; Sasahara, H.; Honma, I.; Komiyama, H.; Haus, J. W. *Journal of Physical Chemistry* **1994**, *97*, 895-901.

(13) Wark, S. E.; Hsia, C.-H.; Son, D. H. *Journal of the American Chemical Society* **2008**, *130*, 9550-9555.

(14) Dloczik, L.; Koenenkamp, R. *Journal of Solid State Electrochemistry* **2004**, *8*, 142-146.

(15) Lehn, J.-M. *Supramolecular Chemistry*; VCH: Weinheim, Germany, **1995**.

(16) Jun, Y.-W.; Lee, S.-M.; Kang, N.-J.; Cheon, J. *Journal of the American Chemical Society* **2001**, *123*, 5150-5151.

(17) Sigman, M. B. Jr.; Ghezelbash, A.; Hanrath, T.; Saunders, A. E.; Lee, F.; Korgel, B. A. *Journal of the American Chemical Society* **2003**, *125*, 16050-16057.

(18) Tolbert, S. H.; Alivisatos, A. P. *Science* **1994**, *265*, 373-376.

(19) Pietryga, J. M.; Werder, D. J.; Williams, D. J.; Casson, J. L.; Schaller, R. D.; Klimov, V. I.; Hollingsworth, J. A. *Journal of the American Chemical Society* **2008**, *130*, 4879-4885.

Chapter 6.

Optical Properties of Nanocrystal Heterostructures Produced by Cation Exchange

6.1 Optical Absorption and Emission of Binary Nanorods

As detailed in the previous chapters, cation exchange enables the fraction of two semiconductor materials to be systematically varied within individual colloidal nanocrystals. Analogous to band gap engineering in semiconductor thin-films, the electronic coupling of components within nanocrystal heterostructures can be manipulated to obtain the specific optoelectronic properties (see Chapter 1.2 for an introduction to the electronic structure and optical properties of semiconductor nanocrystals). The energy offsets between the conduction and valence bands of each of the two semiconductors can be tuned through quantum-size effects based on dimensions of the initial nanocrystals and the fraction converted by cation exchange. Along with the band offsets, the spatial organization of materials within each nanostructure governs the excitation and relaxation pathways of photo-excited charge carriers. Here, we describe the optical properties of the CdS-Ag_2S and CdS-Cu_2S nanorod heterostructures produced by cation exchange in terms of the electronic band alignment between the two materials, the fraction of the nanorod converted, and the heterostructure morphology.

CdS and Ag_2S have a sandwiched, Type I alignment of their valence and conduction bands, where the valence band edge of Ag_2S is higher in energy than that of CdS, and conduction band edge of Ag_2S is lower in energy than the CdS conduction band edge.[1-3] CdS and Cu_2S have a staggered, Type II alignment where both the valence and conduction band edges of Cu_2S are higher in energy than those of CdS.[4,5] The binary nanorod morphology in combination with the band offsets for these materials gives rise to unique optical properties. Linear arrays of Ag_2S quantum dots embedded within a larger band gap CdS regions function as tunable near-infrared (NIR) emitters. The asymmetric morphology of the CdS-Cu_2S nanorods may enable the transport of oppositely charges carriers along the CdS and Cu_2S segments to extract charges following photo-induced charge separation. Analogously, an electrically bias applied to the nanorods can produce photon emission through radiative recombination of electrons and holes at the interface.

The optical absorbance spectra of the heterostructures are primarily a function of the relative amount of the two materials within the nanorods. CdS is a direct band gap (E_g) semiconductor that absorbs in the blue region of the visible spectrum (E_g = 2.54 eV), while Ag_2S and Cu_2S both have indirect gaps that absorb in the near-infrared (E_g = 0.9 eV and 1.2 eV, respectively).[2-5] Absorbance spectra for CdS-Ag_2S and CdS-Cu_2S nanorods made with different M^+/Cd^{2+} ratios ($M^+ = Ag^+$ or Cu^+) are shown in Figure 6.1. Both sets of absorbance spectra show that the first exciton peak of the CdS nanorods remains at the same spectral position for up to ~ 40% of the nanorod converted to Ag_2S or Cu_2S (i.e. M^+/Cd^{2+} ratios up to ~ 0.8). This implies that the CdS regions of the

nanorod do not change significantly in diameter during exchange, as etching of the nanorod would lead to a blue-shift in the exciton peak.[6] The absorption cross-section in the blue region increases with for larger fractions of Ag_2S (Cu_2S) along the appearance of a tail to the red of the CdS absorption edge, due to smaller E_g of these materials. Thus, the optical absorption of the binary nanorods can be easily tuned through the visible region based on the amount of Ag^+ or Cu^+ added.

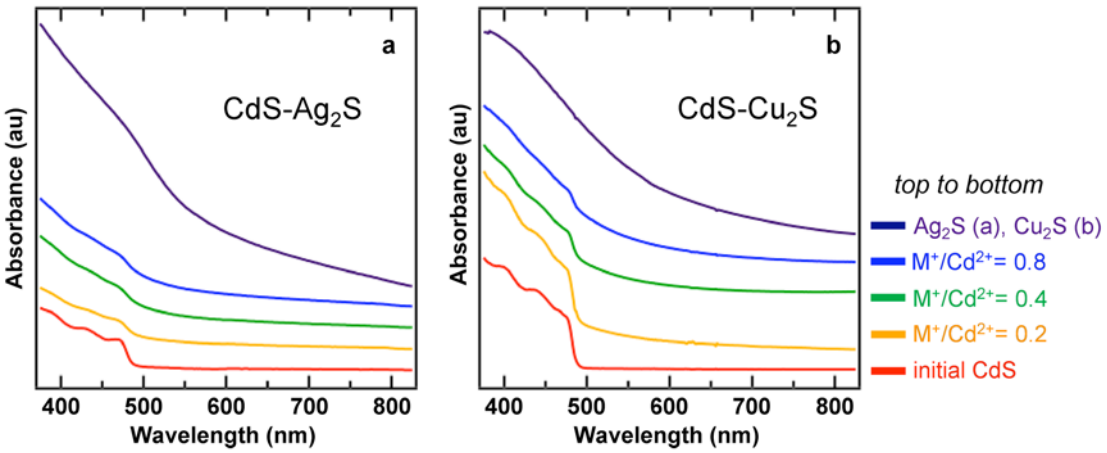

Figure 6.1. Optical absorbance spectra of nanorod heterostructures made by cation exchange. (a) Absorbance of CdS-Ag_2S nanorods made with increasing Ag^+/Cd^{2+} ratios. (b) Absorbance of CdS-Cu_2S nanorods made with increasing Cu^+/Cd^{2+} ratios. The M^+/Cd^{2+} ratios are given in the legend at the right.

The fluorescence emission of the CdS-Ag_2S nanorod heterostructures is that of a Type I array of Ag_2S quantum dots separated by confining regions of CdS (see Figure 6.2). Exciton emission from the initial CdS nanorods is quenched after cation exchange accompanied by near-infrared (NIR) emission from Ag_2S. The emission wavelength of the Ag_2S regions depends upon their size, ranging from ~ 1000 – 1300 nm. Fully

converted Ag_2S nanorods display weak emission matching the bulk band gap for Ag_2S (1300 nm, ~ 0.95 eV), while the spectral position shifts to higher energy in partially exchange structures due to quantum confinement of the smaller Ag_2S regions. Bimodal spectra are observed for low to intermediate exchange fractions are a result of the Ostwald ripening process, where emission from the smaller Ag_2S regions disappears as they merge into larger ones. At ~ 10% conversion (Ag^+/Cd^{2+} = 0.2), the emission spectrum displays a shoulder to the red, corresponding to the small fraction of Ag_2S segments of larger size (usually found at the ends of the nanorods). While at ~ 20% conversion ($Ag^+/Cd2^+$ = 0.4), the relative intensities of the two peaks have switched, and the spectrum contains a shoulder to the blue from the remaining small Ag_2S regions which have not been absorbed by the larger segments.

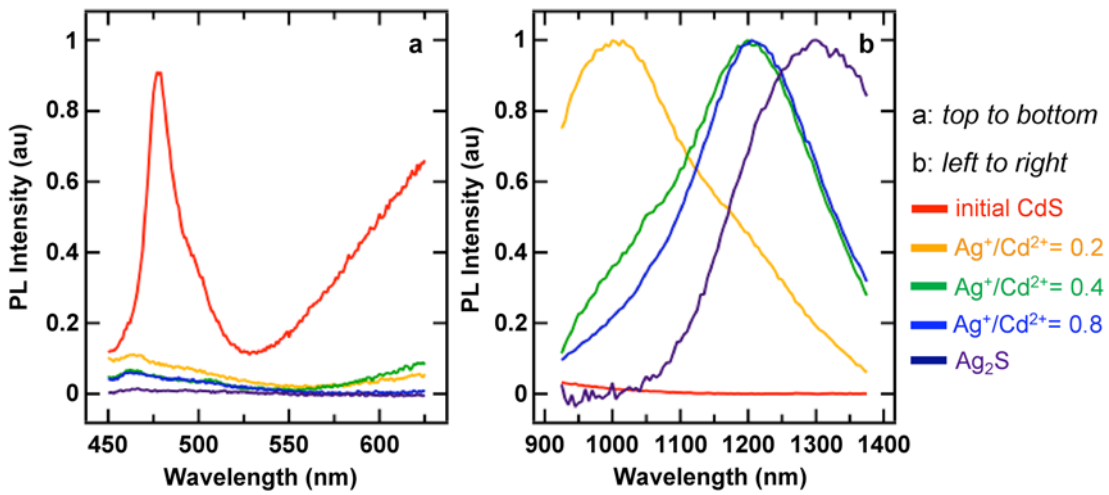

Figure 6.2. Emission spectra of CdS-Ag_2S nanorod heterostructures. (a) Visible emission spectra at 400 nm excitation for the initial CdS nanorods and CdS-Ag_2S nanorods made with increasing Ag^+/Cd^{2+} ratios. The CdS exciton peak is quenched after cation exchange. (b) Near-infrared emission spectra at 500 nm excitation show emission from the CdS-Ag_2S heterostructures, which red shifts with increasing size of the Ag_2S regions. The Ag^+/Cd^{2+} ratios are given in the legend at the right.

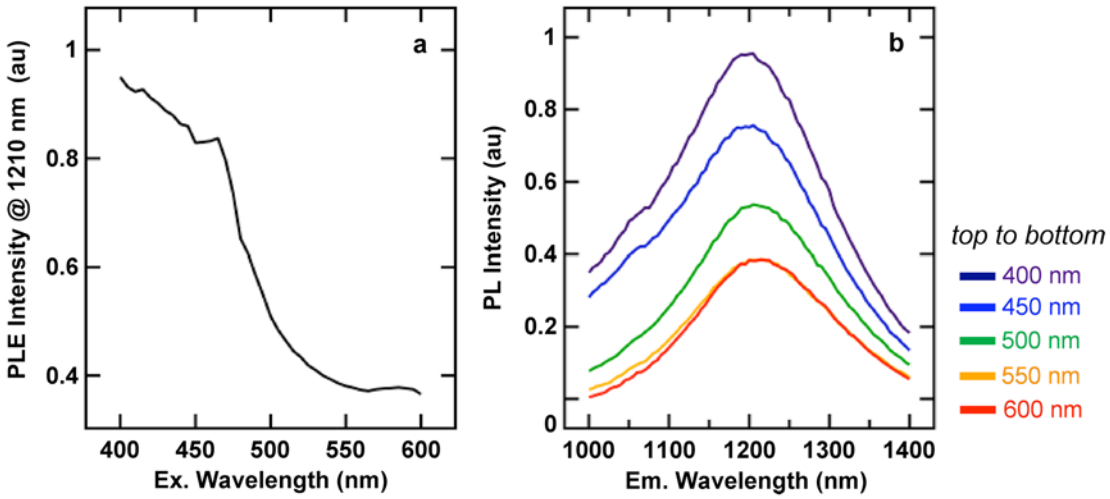

Figure 6.3. Emission intensity of CdS-Ag_2S nanorod heterostructures as a function of excitation wavelength. (a) Photoluminescence excitation spectrum for CdS-Ag_2S heterostructures (Ag^+/Cd^{2+} = 0.8) where the emission intensity at 1210 nm is plotted while the excitation wavelength is varied from 400 to 600 nm. NIR emission from the heterostructures increases significantly in intensity when the excitation wavelength is above the CdS band gap. (b) Emission spectra for the CdS-Ag_2S heterostructures at different excitation wavelengths. The excitation wavelengths are provided in the legend to the right. The emission spectra are color-coated according to the legend on the right.

Figure 6.3a shows a photoluminescence excitation spectrum for CdS-Ag_2S nanorods, where the relative intensity of the NIR emission peak is plotted as a function of the excitation wavelength. Emission from Ag_2S increases significantly in intensity when the excitation energy is above the band gap of CdS. While the slope of the absorbance in fully converted Ag_2S nanorods also increases around 525 nm (see Figure 6.1a), the large increase in emission suggests electronic coupling of the two materials at the interface, where excited carriers in the CdS regions relax into the Ag_2S band levels. Emission spectra for CdS-Ag_2S heterostructures, which have a maximum at 1210 nm (Ag^+/Cd^{2+} = 0.8), are plotted in Figure 6.3b for excitation wavelengths ranging from

400-600 nm. Thus, Stokes shifts of several hundred nanometers are possible, where the CdS regions can act as an absorbing material for visible light producing NIR emission from the Ag_2S regions.

Similar to Ag^+ exchange, the CdS exciton peak disappears after Cu^+ exchange, accompanied by a new emission peak in the NIR. However, the spectral position of the emission from CdS-Cu_2S heterostructures does not change with the volume fraction of Cu_2S within the nanorods. Figure 6.4 shows absorption and emission spectra of CdS-Cu_2S nanorods, where acetonitrile (MeCN) added to the Cu^+ solution before mixing with the CdS nanorods was used to adjust the fraction converted to Cu_2S. MeCN binds to free Cu^+ cations in solution inhibiting the exchange reaction.[7] Thus, as the MeCN/Cu^+ ratio decreases, the fraction of the nanorod converted to Cu_2S increases as seen in the absorbance spectra in Figure 6.4a. While the emission intensity of the CdS-Cu_2S heterostructures varies for different conversion fractions, the spectral profile, which consists of two overlapping peaks, stays approximately the same (see Figure 6.4b). Transferring the nanocrystals from toluene to tetrachloroethylene, generally led to a decrease in the intensity of the peak centered at ~ 875 nm and an increase in intensity of the peak at ~ 725 nm (Figure 6.4c). The higher energy peak (~ 725 nm) may be attributed to surface trap emission, as chlorinated solvents often weaken surfactant passivation of the nanocrystal surface leading to increased trap emission. This peak also has a similar spectral position to the trap emission observed in the initial CdS nanorods at ~ 700 nm. The lower energy peak (~ 875 nm, 1.4 eV) roughly matches the band gap energy of Cu_2S (1.2 eV). These spectra were not wavelength corrected for the spectral

response of the detector. Because the sensitivity of the CCD detector falls off around 900 nm, the true position of this peak is slightly higher in energy.

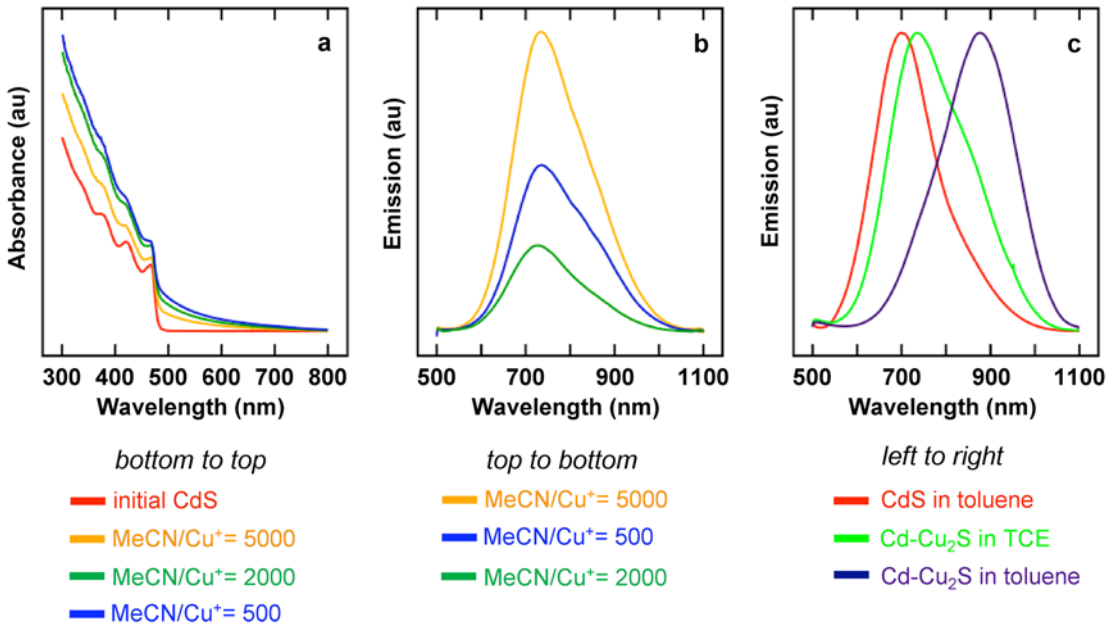

Figure 6.4. Absorbance and emission spectra of CdS-Cu_2S nanorod heterostructures. (a) Absorption spectra of the initial CdS nanorods and CdS-Cu_2S nanorods made with decreasing MeCN/Cu^+ ratios. The fraction of Cu_2S within the nanorods increases with decreasing amounts of MeCN (b) Near-infrared emission spectra of the same CdS-Cu_2S nanorods at 400 nm excitation. The emission spectra profiles are similar for different Cu_2S conversion fractions. (c) Trap emission from the CdS nanorods compared CdS-Cu_2S heterostructures in toluene and tetrachloroethylene (TCE). The spectra are color-coated according to the legend below each plot.

The conduction band edges of bulk CdS and Cu_2S are nearly the same energy, while the valence band edge is much higher in energy for Cu_2S compared to CdS.[4] The emission peak at ~ 875 nm likely arises from radiative the recombination of an electron that is delocalized over the entire nanorod with a hole that is localized to the Cu_2S

region. The Cu_2S valence band edge should not change significantly in energy with the size of the Cu_2S region due to the heavier effective mass of the hole. Furthermore, once the Cu_2S segments form at the ends of the nanorods, their diameter (the confining dimension) remains approximately the same as the fraction of the nanorod converted to Cu_2S increases. For these reasons, the CdS-Cu_2S emission will be relatively insensitive to quantum-confinement effects compared to that of the CdS-Ag_2S nanorod heterostructures.

Optical absorption and emission spectra are useful for characterizing the recovery of the electronic structure during sequential exchange reactions of CdS nanocrystals to Ag_2S and back to CdS. To promote the reverse exchange of Ag_2S nanocrystals to CdS, a large excess of Cd^{2+} ions, an elevated temperature, and coordinating molecules with higher binding strengths to Ag^+ (MeCN and TBP) are used.[8,9] TEM images of the initial CdS nanorods, converted Ag_2S nanorods, and back-converted CdS nanorods are shown in Figures 6.5a-c. The nanorod shape is preserved after the forward Ag^+ exchange reaction, although a small percentage of the nanorods have coalesced. The back exchange reaction generally preserves the anisotropic shape, but the nanorods have increased surface roughness, likely due to etching during the transformation. The absorption and emission spectra for the three nanorod samples are shown in Figures 6.5d and 6.5e. The conversion of the Ag_2S nanorods back to CdS is accompanied by the recovery of the original exciton absorption features. However, there is a slight blue shift in the first exciton peak position (~3 nm), and the tailing of the absorption to the red of the CdS exciton peak indicates the nanorods still contain a small amount of Ag_2S. The

fluorescence spectrum of the back-converted CdS nanorods shows weak exciton emission and greatly increased trap emission. The increase in trap emission is a result of increased disorder of the nanocrystal surface after sequential cation exchange reactions.

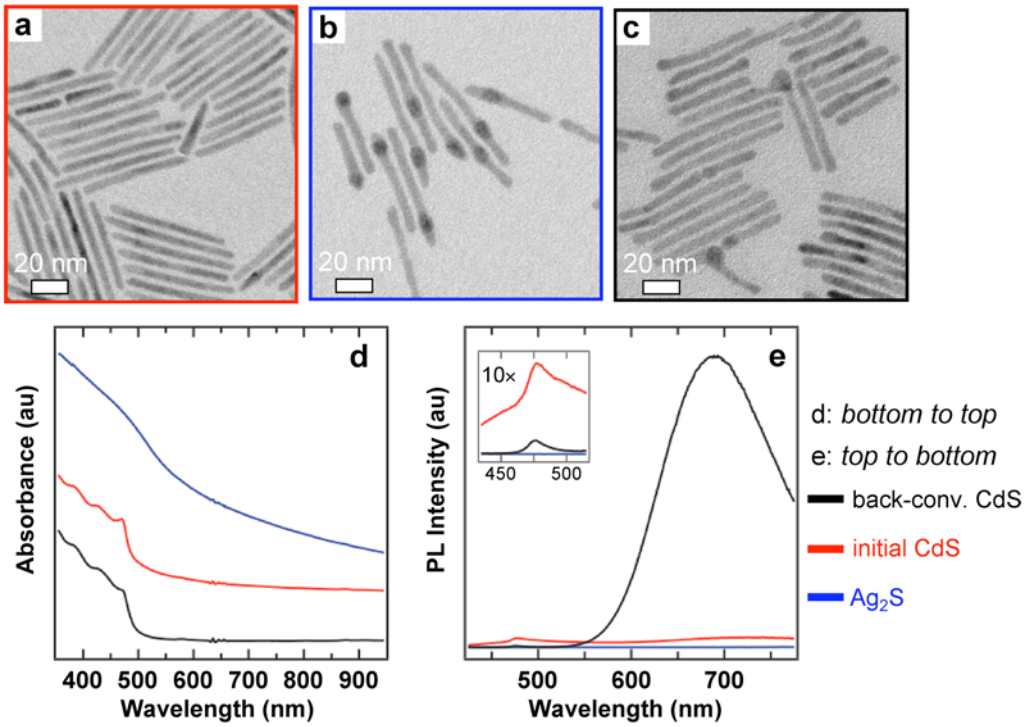

Figure 6.5. Forward and back conversion of nanorods between CdS and Ag_2S. (a) TEM image of the initial CdS nanorods. (b) Ag_2S nanorods made by full exchange. (c) Recovered CdS nanorods after back conversion from Ag_2S to CdS. (d) Absorbance spectra of the three nanorod samples. The absorbance spectra have been vertically offset for clarity. (e) Emission spectra of the three nanorod samples showing the large increase in trap emission after back conversion. The inset shows the band-edge emission from the CdS samples on a 10× scale. The three nanorod samples are color-coated according to the legend on the right.

6.2 Carrier Relaxation in CdS-Ag_2S Nanorod Heterostructures.

The Ag_2S regions introduce both new radiative and non-radiative pathways for photo-excited charge carriers within the CdS nanorods. Interfacial and surface defects arising from the cation exchange process may compete with the transfer of excited electrons from the CdS conduction band to Ag_2S, limiting the quantum yield of the NIR emission. Ultrafast pump-probe spectroscopy was used to study the relaxation of carriers as a function of the relative fraction of the two materials within the nanorods. A 400-nm pump pulse from a femtosecond Ti:sapphire laser excites electrons into the conduction band of CdS, leading to a transient bleach in the absorption signal. A probe pulse with a variable delay of 1-1000 picoseconds (ps) from the pump pulse is tuned to the first exciton peak of CdS at 470 nm to monitor the recovery dynamics of the absorption bleach. After thermal relaxation of the excited electron to the lowest lying level of the conduction band, it may radiatively recombine with a hole from the valence band edge, or non-radiatively relax to a mid-gap trap state. The overall time it takes for this process to occur is referred to as the recovery time, τ, of the transient bleach signal. Non-radiative relaxation through Auger interactions typically takes place on the order tens of picoseconds in cadmium chalcogenide nanocrystals, whereas radiative band-edge recombination occurs on a time-scale of tens to hundreds of nanoseconds.[10-12] Therefore, the recovery dynamics is an important measurement of the degree of defect states in the nanocrystals.

Bleaching dynamics of the initial CdS nanorods are shown in Figure 6.6a. The recovery of the absorption is best fit to a biexponential decay with time constants, τ_1 = 202 ± 52 picoseconds (ps) and τ_2 = 3300 ± 770 ps. The time constant, τ_1, corresponds to relaxation to surface defect states, while τ_2 is attributed to subsequent relaxation to deep trap levels over a time-scale of 100-1000 ps as well radiative recombination events on the order of nanoseconds. Figure 6.6b shows normalized bleaching dynamics of Ag_2S-CdS nanorods with Ag^+/Cd^{2+} ratios ranging from 0.25 to 0.75 and Table 6.1 summarizes the biexponential fits to the decay of the transient bleaching signal. The bleach recovery occurs significantly faster in the CdS-Ag_2S nanorods, and the relative weight of the fast time constant, τ_1, increases, as the fraction of Ag_2S within the nanorods increases. The longer time constant, τ_2 ~ 2000 ps, is still present in the kinetic traces, but the contribution of τ_1 dominates the dynamics for higher conversion fractions to Ag_2S. At ~ 25% conversion (Ag^+/Cd^{2+} = 0.50), the weight of τ_2 in the biexponential fit is ~ 17%, and τ_2 is negligible by ~ 37% conversion (Ag^+/Cd^{2+} = 0.75). Thus, carriers excited into the CdS conduction band quickly relax into mid-gap states provided by introduction of the Ag_2S regions. Defect levels include surface states resulting from disorder introduced by cation exchange as well as interfacial states due to the large lattice mismatch between CdS and Ag_2S. These processes compete with radiative band edge recombination following the transfer of excited electrons from the conduction band of CdS to that of Ag_2S (see Figure 6.3). The growth of an inorganic shell may passivate surface states in order to increase the quantum yield of the Ag_2S NIR emission. For instance, partial

exchange with Zn^{2+} over the entire heterostructure surface could be used to coat the segmented nanorods with a few monolayers of the larger band gap ZnS.

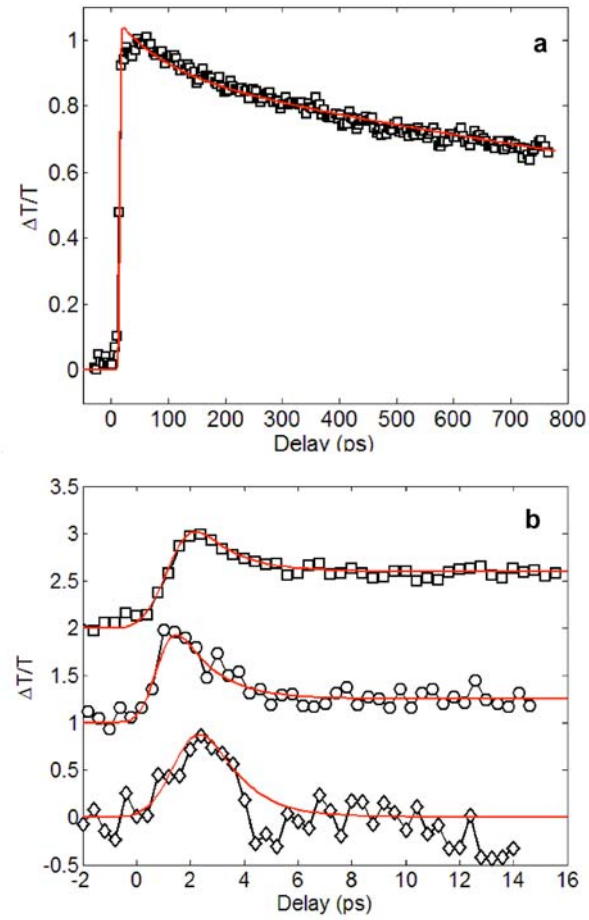

Figure 6.6. Transient bleaching of CdS and CdS-Ag_2S nanorods. The pump excitation is tuned to 400 nm and the probe pulse to 470 nm. (a) The initial CdS nanorods (□). (b) CdS-Ag_2S nanorods made with Ag^+/Cd^{2+} = 0.25 (□), Ag^+/Cd^{2+} = 0.5 (○), and Ag^+/Cd^{2+} = 0.75 (◇). The Ag_2S material drastically shortens the excited state lifetime of electrons in the conduction band of CdS.

Table 6.1. Time constants of the bleaching recovery in CdS and CdS-Ag_2S nanorods.[a]

Ag^+/Cd^{2+}	decay time, τ_1 (ps)	weight τ_1 (%)	decay time, τ_2 (ps)	weight τ_2 (%)
0	202 ± 52	31	3300 ± 770	69
0.25	1.2	63	1900	27
0.50	1.4	83	2000	17
0.75	1.1	100	--	--
0 (back converted)	100 ± 32	18	3470 ± 277	82

[a] The fraction of the nanorod converted are provided in the left-hand column. The transient absorption spectra were fit to biexponential decays. The weight contribution of each of the time constants to the fit to the right of the time constant.

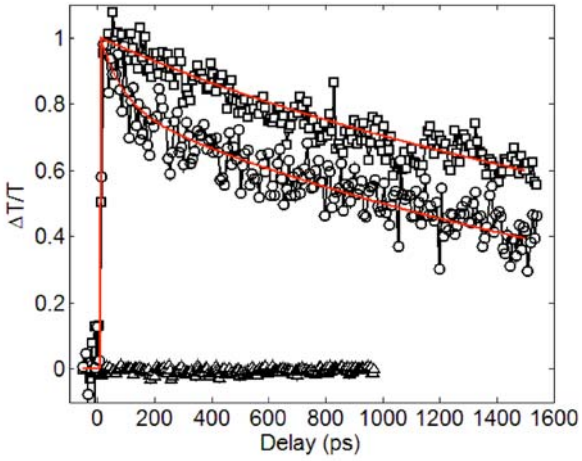

Figure 6.7. Recovery of the bleach dynamics after reverse exchange. (□) The initial CdS nanorods. (△) The fully-converted Ag_2S nanorods show no transient bleaching signal. (○) Upon back-exchange to CdS the bleaching signal is recovered with an increase in the contribution from the short time constant.

Transient absorption spectroscopy can also quantify the extent to which the carrier dynamics are recovered when Ag_2S nanorods are converted back to CdS, as shown in Figure 6.7. In this sample, the bleach decay of the initial CdS nanorods has

time constants of τ_1 = 803 ± 100 ps and τ_2 = 3680 ± 117 ps, while the transient absorption signal is completely quenched after full Ag^+ exchange. Reverse exchange from Ag_2S back to CdS shows the near-complete recovery of the bleach signal with decay time constants, τ_1 = 100 ± 32-ps and τ_2 = 3470 ± 277-ps. The fast decay time constant, τ_1, is shorter in the recovered CdS nanorods leading to a faster recovery of the bleaching signal. These changes qualitatively agree with static absorbance and fluorescence spectra shown in Figures 6.5b and 6.5c. The trap emission is much greater in the recovered CdS nanorods compared to the original CdS nanorods. Also, the absorbance spectra indicate that a small amount of Ag_2S is still present within the recovered CdS nanorods. The shortening of the fast relaxation time constant is caused by the increased disorder at the nanocrystal surface during the exchange reactions as well as the remaining Ag_2S within the nanorods. However, it is quite remarkable that to a large extent, the optical properties of the nanorods can be reversibly switched through sequential chemical transformations.

6.3 Applications of CdS-Cu_2S and CdS-Ag_2S Binary Nanorods

The absorption of the CdS-Ag_2S and CdS-Cu_2S heterostructures can be tuned to match the solar spectrum through the relative fraction of the high (CdS) and low (Ag_2S or Cu_2S) band gap materials within the nanorods, making them attractive materials for solar photon collection. Previous nanocrystal-based solar cells have used two different single component nanocrystals which are either blended together or cast sequentially to make a bilayer film.[13,14] After photo-excitation of charge carriers, one type of

nanocrystal (e.g. CdS or CdSe) functions as the electron carrier, while the other type (e.g. Cu_2S or CdTe) is used to transport holes. However, in these cases the nanocrystals are randomly oriented within the film, and the surfactant layers coating the nanocrystals can inhibit charge transport between them. Forming well-defined and strong contact between the electron and hole carrying regions of the device may lead to more efficient charge separation and improved charge mobility. This may be accomplished through partial cation exchange, which naturally creates an epitaxial connection between specific facets of two crystals within a single nanostructure.

CdS and Cu_2S have a Type II band alignment and exhibit a well-matched absorbance with the solar spectrum. This material system was actively explored in solar cell devices from the 1960s until the 1980s, but ultimately abandoned for a variety reasons:[4] 1) The CdS-Cu_2S interface was complex and not well-understood.[15] 2) Slow diffusion of Cu into the CdS layer over time significantly changes the photoeffect produced by the heterojunction cells.[4] 3) Copper and sulfur have a rich phase diagram with several $Cu_{2-x}S$ phases existing for $0 < x < 0.3$. Each of these phases has different photovoltaic properties, with Cu_2S chalcocite ($x = 0$), being the most favorable.[4] However, it is difficult to prepare macroscopic crystals of phase-pure Cu_2S.[16-18] Nanoscale CdS-Cu_2S heterojunctions have the potential alleviate some of these problems. Since each CdS nanorod is a single crystal, the resulting CdS-Cu_2S interfaces are much simpler than those produced via surface cation exchange of multicrystalline CdS films. The Cu_2S phase of the exchanged nanorods is pure chalcocite and is stable over a period of months. We are currently using HRTEM, electron energy loss

spectroscopy (EELs), and electron diffraction at low gun bias and low temperature to examine the atomic structure of these CdS-Cu_2S nano-scale interfaces in detail, in order to better understand the structural changes that occur under an electrical bias.

As preliminary work, we have also fabricated nanocrystal-based solar cells consisting of films containing layers of separate CdS nanorods and Cu_2S nanodots, with a power conversion efficiency of up to 1.6%.[14] Improved charge separation at the epitaxial CdS-Cu_2S interface of the binary nanorod heterostructures is expected compared to the bilayers of CdS and Cu_2S nanocrystals, which have an organic layer of surfactants separating them. By vertically aligning the binary nanorods, electrons and holes can be transported along the CdS and Cu_2S segments, respectively, for charge collection at electrical contacts sandwiching the aligned nanorod film (see Figure 6.8). Alternatively, charge carriers could be extracted radially, though the use of a conformal polymer coating (or liquid in the case of a photoelectrochemical cell), which would minimize charge recombination by significantly shortening the necessary diffusion length for charge collection.[19,20] The efficiency of photon absorption can be tuned with the length of the nanorods and the relative fraction of CdS and Cu_2S, where the lower band gap Cu_2S has a higher absorption coefficient at both blue and red wavelengths. To this end, we are working to vertically align large areas of the asymmetric CdS-Cu_2S nanorods. CdS nanorods have a permanent dipole moment, which facilitate their alignment in electric fields.[21] The asymmetry introduced by converting one end of the nanorods to Cu_2S may be used to enhance the degree of field alignment. Alternatively, a

film of aligned CdS nanorods could be placed in a dilute solution of Cu+ to transform the top layer of the film to Cu_2S

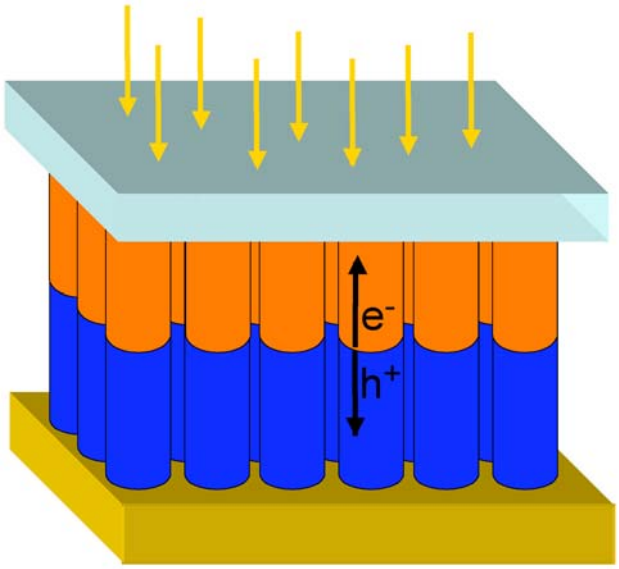

Figure 6.8. Schematic of a vertically aligned CdS-Cu_2S binary nanorods to improve the efficiency of photon absorption and charge collection in nanocrystal-based solar cells.

The CdS-Ag_2S nanorod heterostructures exhibit NIR emission, which can be tuned with the size of the Ag_2S regions. Such segmented nanorods containing many electronically independent nanodots may be of interest as luminescent probes for use in biological labeling.[22,23] The emitted NIR photons would not be significantly absorbed by water and thus could be transmitted through living tissue. Coating the Ag_2S regions with an inorganic shell may passivate surface defects to increase the quantum yield of fluorescence emission. In particular, a ZnS overlayer could serve both to passivate the

Ag_2S regions and prevent leakage of Cd^{2+} from the CdS regions. While Ag_2S may not be stable at the temperatures required for conventional epitaxial shell growth, an alternative method would be partial cation exchange with Zn^{2+} cations to form a thin layer of ZnS.

While there is strong electronic coupling between the adjoining CdS and Ag_2S regions, in the present configuration the Ag_2S quantum dots are only very weakly coupled to each other because the CdS segments between them are large. Structures where the Ag_2S regions both regularly spaced and close enough for their electron wave functions to have significant overlap may lead to the formation of delocalized excited state mini-bands.[24,25] Such materials are of great interest for use in nanocrystal solar cells, where the sparse density of electronic states within the nanostructure may lead to multiple exciton generation (MEG), in which a single photon creates multiple electron-hole pairs.[12,26] Highly-efficient MEG has been reported in PbS and PbSe nanocrystals, which is attributed to the small band gap and large degree of quantum-confinement in these materials.[27,28] Thus, rather than changing the periodicity of the Ag_2S regions, an alternative route would be to convert the CdS-Ag_2S superlattices to CdS-PbS superlattices via Pb^{2+}-Ag^{+} cation exchange, where electronic coupling of the embedded PbS quantum dots would still be possible for much larger separations.

6.4 Chapter 6 Bibliography

(1) Robinson, R. D.; Sadtler, B.; Demchenko, D. O.; Erdonmez, C. K.; Wang, L.-W.; Alivisatos, A. P. *Science* **2007**, *317*, 355-358.

(2) Ninomiya, S.; Adachi, S. *Journal of Applied Physics* **1995**, *78*, 1183-1190.

(3) Junod, P.; Hediger, H.; Kilchor, B.; Wullschleger, J. *Philosophical Magazine* **1977**, *36*, 941-958.

(4) Fahrenbruch, A. L.; Bube, R. H. *Fundamentals of Solar Cells*; Academic Press: New York, **1983**.

(5) Marshall, R.; Mitra, S. S. *Journal of Applied Physics* **1965**, *36*, 3882-3883.

(6) Li, L.-S.; Hu, J.; Yang, W.; Alivisatos, A. P. *Nano Letters* **2001**, *1*, 349-351.

(7) Chaudhry, M.; Persson, I. *Journal of the Chemical Society, Faraday Transactions* **1994**, *90*, 2243-2248.

(8) Son, D. H.; Hughes, S. M.; Yin, Y.; Alivisatos, A. P. *Science* **2004**, *306*, 1009-1012.

(9) Camargo, P. H. C.; Lee, Y. H.; Jeong, U.; Zou, Z.; Xia, Y. *Langmuir* **2007**, *23*, 2985-2992.

(10) Klimov, V. I.; Mikhailovsky, A. A.; McBranch, D. W.; Leatherdale, C. A.; Bawendi, M. G. *Science* **2000**, *287*, 1011-1013.

(11) Crooker, S. A.; Barrick, T.; Hollingsworth, J. A.; Klimov, V. I. *Applied Physics Letters* **2003**, *82*, 2793-2795.

(12) Klimov, V. I. *Journal of Physical Chemisty B* **2006**, *110*, 16827-16845.

(13) Gur, I.; Fromer, N. A.; Geier, M. L.; Alivisatos, A. P. *Science* **2005**, *310*, 462-465.

(14) Wu, Y.; Wadia, C.; Ma, W.; Sadtler, B.; Alivisatos, A. P. *Nano Letters* **2008**, *8*, 2551-2555.

(15) Sands, T. D.; Washburn, J.; Gronsky, R. *Solar Energy Materials* **1984**, *10*, 349-370.

(16) Cook, W. R. Jr.; Shiozawa, L.; Augustine, F. *Journal of Applied Physics* **1970**, *41*, 3058-3063.

(17) Evans, H. T. *Nature Physical Science* **1971**, *232*, 69-70.

(18) Sands, T. D.; Washburn, J.; Gronsky, R. *Physica Status Solida A* **1982**, *72*, 551-559.

(19) Maiolo, J. R.; Kayes, B. M.; Filler, M. A.; Putnam, M. C.; Kelzenberg, M. D.; Atwater, H. A.; Lewis, N. S. *Journal of the American Chemical Society* **2007**, *129*, 12346-12347.

(20) Spurgeon, J. M.; Atwater, H. A.; Lewis, N. S. *Journal of Physical Chemistry C* **2008**, *112*, 6186-6193.

(21) Ryan, K. M.; Mastroianni, A.; Stancil, K. A.; Liu, H.; Alivisatos, A. P. *Nano Letters* **2006**, *6*, 1479-1482.

(22) Bruchez, M. Jr.; Moronne, M.; Gin, P.; Weiss, S.; Alivisatos, A. P. *Science* **1998**, *281*, 2013-2016.

(23) Fu, A.; Gu, W.; Boussert, B.; Koski, K.; Gerion, D.; Manna, L.; Gros, M. L.; Larabell, C. A.; Alivisatos, A. P. *Nano Letters* **2007**, *7*, 179-182.

(24) Lazarenkova, O. L.; Balandin, A. A. *Journal of Applied Physics* **2001**, *89*, 5509-5515.

(25) Smith, B. B.; Nozik, A. J. *Nano Letters* **2001**, *1*, 36-41.

(26) Nozik, A. J. *Physica E* **2002**, *14*, 115-120.

(27) Schaller, R. D.; Klimov, V. I. *Physical Review Letters* **2004**, *92*, 186601-1-4.

(28) Ellingson, R. J.; Beard, M. C.; Johnson, J. C.; Yu, P.; Micic, O. I.; Nozik, A. J.; Shabaev, A.; Efros, A. L. *Nano Letters* **2005**, *5*, 865-871.